2013

Electrostatic actuation based modulation of polar molecules and associated force interaction studies

Xiao Ma
Iowa State University

Recommended Citation

Ma, Xiao, "Electrostatic actuation based modulation of polar molecules and associated force interaction studies" (2013). *Graduate Theses and Dissertations*. 13488.
http://lib.dr.iastate.edu/etd/13488

Electrostatic actuation based modulation of polar molecules and associated force interaction studies

by

Xiao Ma

A dissertation submitted to the graduate faculty
in partial fulfillment of the requirements for the degree of
DOCTOR OF PHILOSOPHY

Major: Mechanical Engineering

Program of Study Committee:
Pranav Shrotriya, Major Professor
Marit Nilsen-Hamilton
Sriram Sundararajan
Shankar Subramaniam
Monica Lamm

Iowa State University
Ames, Iowa
2013

TABLE OF CONTENTS

LIST OF FIGURES

LIST OF TABLES

ACKNOWLEDGEMENTS

First, I would like to express a sincere appreciation to my advisor Prof. Pranav Shrotriya for his guidance, help and patience during the past 6 years of research. Without his support, the work could not been accomplished.

I would also like to express gratitude and appreciation to all of my committee members: Prof. Nilsen-Hamilton, Prof. Sundararajan, Prof. Subrmaniam, and Prof. Lamm. They served on my POS committee and provided me with quite a lot valuable suggestions and instructions to my research.

My thanks extend to all professors and colleagues in the project, particularly to Prof. Curtis Mosher for many useful discussions, technical support and assistance.

I would also like to thank all the lab colleagues, former and present: Janice Marquardt, Kyungho Kang, Yue Zhao, Therin Young, Miguel Rodriguez, and Yang Hong, with whom I shared and discussed a lot during this professional research route.

I would like to thank my family for their support and love. They carried me through these years and provided me with strong support and encouragement. Without them, I could not imagine how I can overcome all of the obstacles during this long journal and finally reached the shore.

I would also like to express my gratitude on the financial support for this study, which was provided by National Institute of Justice and National Science Foundation Career grant CMMI-0547280 and US-DOE Ames Laboratory.

ABSTRACT

Seamless integration of artificial components with biological systems to form an elegant biotic-abiotic interface or smart surface has promising application potential in biomedical engineering. The specific aim of this study is to implement the actuation and modulation of binding behavior between biomolecules under electrostatic stimuli, and investigate the corresponding force interaction between the complementary pairs. The nanofabrication technology was utilized to establish the patterned binding pair of thrombin and DNA aptamer on gold substrate, and different electrical fields were applied on the system to evaluate electrostatic influence. The atomic force microscopy (AFM) surface imaging was then used to explicate the surface height change after the removal of the electrical fields. The height change of the surface showed that positive electrical fields can successfully break the bonds between thrombin and aptamer, while moderate negative electrical fields kept the integral structure. The experimental studies implement the idea of electrostatic actuation and modulation of the complementary pair. The force interaction between the pair was then investigated through AFM based dynamic force spectroscopy (DFS). The open circuit DFS experiment was conducted first to clarify the magnitude of single molecule level force interaction between thrombin and aptamer, and the linear dependence of rupture force on logarithmic loading rate was observed. A single energy barrier model was used to understand the binding physics and kinetics. By fitting the model with experiment data, we could acquire important kinetic parameters t_{off} and x_{β}. Then in-situ electrochemical atomic force microscopy (ECAFM) based DFS experiment was conducted to investigate the electrostatic influence upon molecular force interaction between thrombin and aptamer. The force interaction difference showed that positive electrical fields lowered the dissociation force between thrombin and aptamer, while negative electrical fields held similar force level with zero potential. The ECAFM experimental studies further support the conclusion of electrostatic actuation and modulation of the complementary pair. Besides, the root cause for the change of binding behavior and force interaction between the biomolecules under electrostatic fields is the conformational transition of the molecules, which might be illustrated by the molecular dynamics (MD) simulation. Therefore, a MD based computational study was performed on self-assembled monolayer (SAM) with polar end group under the application of electrical fields to clarify the conformational transition and associated friction change of the monomolecular thin films. The simulation results showed that positive electrical fields can generate larger conformational transition of the SAMs, which led to a greater frictional coefficient drop of the surface, while negative electrical fields kept similar conformational state and frictional response as the zero potential. The simulation result provides another explanation of the electrostatic actuation based modulation of polar molecule functionalized surface.

CHAPTER 1. INTRODUCTION

Seamless and exquisite integration of artificial components with biological systems to form a biotic-abiotic interface or a smart surface has recently attracted increasing interests. The structural and functional biotic-abiotic interface can lead to nanoscale, highly sensitive, and flexible bio-sensors and actuators, which may have broad and in-depth applications in biomedical and biomechanical field, such as modulating the activity of biological systems and biomolecules, locating disease, and repairing or reprogramming genetic information, and establishing brain-machine interface (BMI) to control external prostheses (Wong, Almquist et al. 2010), etc. Currently the tools for implementing the above objectives are far from complete, and one of the major challenges on the biotic-abiotic interface integration is to dynamically translate external stimuli into biochemical signals and efficiently transmit such signal into the biological processes.

The objective of the proposed research is to investigate the binding behavior and force interaction between a ligand / receptor system - thrombin and aptamer - under electrical field actuation, and endeavor to obtain a mechanistic understanding of the binding mechanism.

The central hypothesis for this study is that if application of electrical field induces controllable conformational transition in surface immobilized aptamer, then specific binding / dissociation of the counterpart thrombin can be achieved. In order to test this hypothesis, characterization of electrical field influence on biomolecular binding via nanofabrication and atomic force microscopy (AFM) surface imaging and characterization of electrical field influence on intermolecular forces between thrombin / aptamer pair via AFM based dynamic force spectroscopy (DFS) were carried out.

In addition, in order to further understand the mechanism of conformational transition and its influence on the smart surface performance, a computational study of self-assembled monolayer conformational transition and friction performance change under the application of electrical fields were also carried out based on molecular dynamics (MD) simulation, which can provide information of conformational transition on upon monolayer thin film influenced by the external electrical fields. The associated frictional performance change due to the conformational transition implies the potential application of such electrostatic actuation based smart surface design.

1.1 Electrical field influence on conformational transition of charged molecules

Among various kinds of external stimuli, such as such as pH (Hianik, Ostatna et al. 2007), temperature (Nguyen, Pei et al. 2011) and electro-chemical modifications (Gray and Winkler 1996; Willner 2005), electrostatic mechanisms have many advantages on communicating information in biotic-abiotic interface, allowing massively parallel actuation and measurement capabilities that will ultimately be essential for biomedical applications (Wong, Footer et al. 2008; Wong and Melosh 2009; Wong and Melosh 2010). In addition, application of electrostatic fields is an efficient and feasible mechanism to induce conformational transition upon charged bio-molecules without harmful influence on the chemical stability. Electrostatic actuation provides a means for influencing only near surface molecules, the double layer formed near the electrode leads to development of strong electrical fields that only affect the bio-molecules that are close or immobilized on the electrode surface, thus the conformational transition of the charged bio-molecules can be generated by relatively low external voltages. Rant et al. have demonstrated that the conformation of short DNA oligomers immobilized at low grafting densities can be reversibly switched by application of electrical fields (Rant, Arinaga et al. 2004; Rant, Arinaga et al. 2007). Since DNA is negatively charged, positive voltages caused the DNA to flatten on the surface, while negative voltages caused the DNA to orient vertically, as shown in Fig. 1-1(a). Electrostatic fields can also influence self-assembly and hybridization of DNA, as shown in Fig. 1.1(b). Positive voltages (+300 mV) applied to gold electrodes functionalized with single-strand DNA showed a three-fold enhancement in complementary DNA hybridization, while for negative voltage it was an order of magnitude lower.

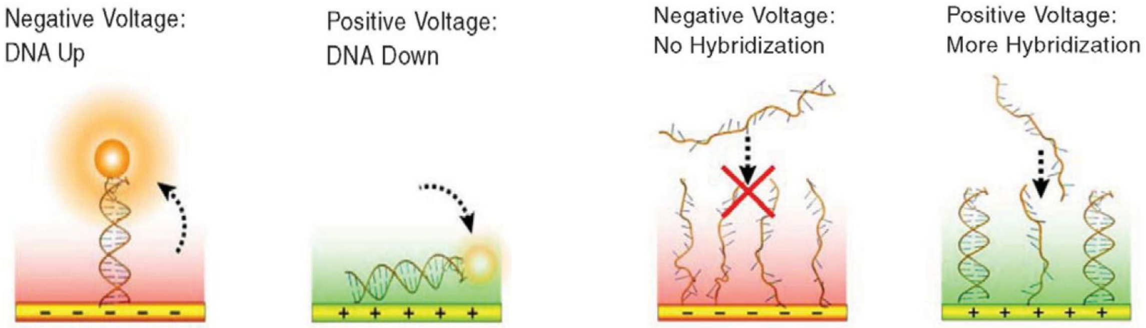

(a) conformational transition (b) hybridization change

Fig. 1-1 Electrical field influence on charged DNA molecule

Electrostatic field based conformational transition is not limited to bio-molecules, Lahann et al. used an analogous approach to cause alkanethiol molecules to bend from a vertical to a horizontal orientation by applying positive electrical field (Lahann, Mitragotri et al. 2003), so that charged functional groups were attracted to the electrode surface, exposing the hydrophobic alkane chain on the surface, which realized the macroscopic surface chemistry change from hydrophilic to hydrophobic nature. Kanaga Karuppiah et al. utilized atomic force microscope (AFM) to evaluate the adhesion and frictional response of a low-density mercaptocarboxylic acid SAM under the application of electrical fields with different polarities (Karuppiah, Zhou et al. 2009), and discovered higher value of adhesion but lower friction level when negative bias electrical fields were applied to the SAM. They attributed the contrary observation between adhesion and friction to the crystalline order of sparse monolayer films, i.e., the higher friction under positive bias is attributed to the relatively disordered structure of the film, whereas the relatively ordered structure under negative bias may cause the friction to decrease.

1.2 Thrombin-aptamer pair as a sample model and micro-contact printing technique

Besides selecting the type of external stimuli (electrical fields) to induce conformational transition on biomolecules, it is also essential to choose an appropriate model biomolecular system to investigate the specific response.

The coagulation catalytic enzyme thrombin and its DNA aptamer provide such a relevant and suitable sample model. Nucleic acid aptamers are a relatively new recognized type of molecules, with similar properties of ligand specificity and affinity to antibodies but with several specific advantages as components of sensors and biomedical devices (Cullen and Greene 1989; Ellington and Szostak 1990; Hermann and Patel 2000). Aptamers are small (15 to 40 nt) with affinities for proteins and other large biomolecules in the picomolar to nanomolar range, and demonstrate exquisite specificity and stability for their receptors due to large structural changes in the binding process, which can be utilized for detection of the target (Jenison, Gill et al. 1994; Yang, Kochoyan et al. 1996), and thus can be a selection for various bio-molecules (Bode, Mayr et al. 1989; Tsiang, Gibbs et al. 1995; Tasset, Kubik et al. 1997; Lavrik, Sepaniak et al. 2004; Gronewold, Glass et al. 2005; Hianik, Ostatna et al. 2005) and biomedical materials and drugs (Lato, Boles et al. 1995; Wallis, Vonahsen et al. 1995; Wang and Rando 1995; Burke, Hoffman et al. 1997; Mannironi, DiNardo et al. 1997; Wallace and Schroeder 1998; Berens, Thain et al. 2001; Stojanovic, de Prada et al. 2001; Win, Klein et al. 2006). The large structural or conformational transition of aptamer associated with binding may be hindered or enhanced through application of electrical fields as demonstrated in previous paragraph.

Thrombin, a catalytic enzyme, is involved in the synthesis of fibrin from fibrinogen during the blood clotting process, has a wide range of health effects in the human system. When thrombin is beyond the normal level, thrombosis may happen due to too much fibrin generated in the bloodstream; when thrombin is lower than the normal level, hemorrhage may happen due to too little fibrin generated. Thrombin has two binding sites to control its catalytic function (Bode, Mayr et al. 1989). The 1st one is the fibrinogen binding site, where the conversion of fibrinogen to fibrin occurs so as to enhance the coagulation process, and the 2nd one is heparin binding site, where heparin binds to thrombin to inhibit the coagulation process, as shown in Fig. 1-2(a). Thrombin has a well established aptamer, which shows a hairpin structure formed by eight guanine bases sequenced in $GGNTGGN_{2-5}GGNTGG$, known as G-quadruplex, as shown in Fig. 1-2(b). The aptamer can fit into thrombin heparin binding site and affects the thrombin in the similar way as heparin (Bode, Mayr et al. 1989; Bock, Griffin et al. 1992). This aptamer has been shown in chemical assays to have high binding specificity (Bode, Mayr et al. 1989; Tsiang, Gibbs et al. 1995; Tasset, Kubik et al. 1997). The strong binding between thrombin-aptamer pair makes it both relevant and suitable for the study of binding behavior and force interaction of the binding pairs.

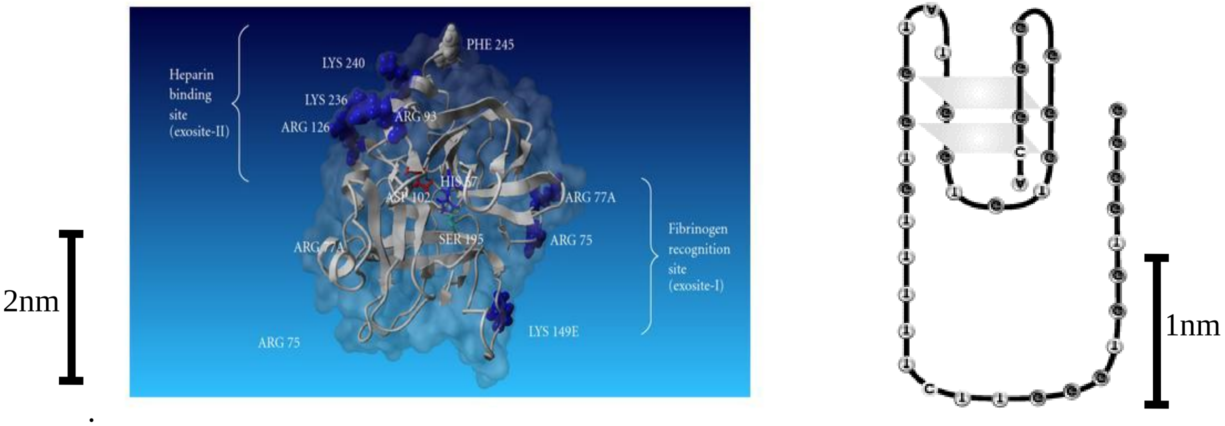

(a) Thrombin (b) Aptamer

Fig. 1-2 Thrombin and apatamer structure

In order to test the binding specificity and conformational transition between thrombin-aptamer pair, micro-contact printing (μCP) is applied to study the height changes upon binding of thrombin / aptamer pair, which is a vell widespread methods for creating micro and nanoscale structures outlined by Kumar and Whitesides (Kumar and Whitesides 1993). To perform micro-contact printing, a flexible polymer poly(dimethyl siloxane) (PDMS) stamp is made from a mold. The alkanethiol solution is exposed to the stamp as an “ink”, and then the liquid is allowed to dry with a gas such as nitrogen. The dried chemical species is then printed on a substrate with a known pattern. The PDMS stamp is then removed, leaving the pattern of the chemical species printed on the substrate, as shown in Fig. 1-3. After that solutions containing the objective complementary species are exposed to the substrate, and deposit on the adjacent area of the printed alkanethiol patterns to form the desired nanostructure subsequently.

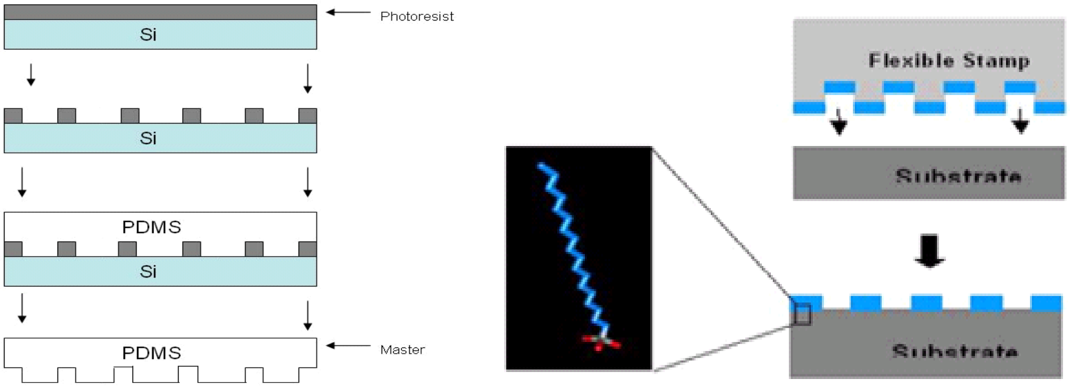

(a) Stamp fabrication (b) Printing process

Fig. 1-3 Micro-contact printing technique

1.3 Force spectroscopy on determination of binding forces between bio-molecules

In the development of micro/nano bio-sensors and architectures, forces between biomolecules are a key factor to determine molecular binding specificity and stability. Low binding forces between a complementary pair of biomolecules may result in an unstable nanostructure, or a lack of sensor sensitivity. In addition, it becomes apparent that there was a need to measure the force of the interaction between biomolecules for a thoroughly understanding of the binding mechanism between the pairs. There is a variety of methods to detect the presence of a certain biomolcules, including charge transfer sensors (Hianik, Ostatna et al. 2005), Love-wave sensors (Gronewold, Glass et al. 2005), microcantilever sensors (Lavrik, Sepaniak et al. 2004). While chemical assays and charge transfer sensors are not as dependent on binding forces for detection, wave sensors and microcantilever sensors require high specificity and stable binding forces.

Dynamic force spectroscopy (DFS) is a method to directly measure binding forces between a single pair of complementary chemical species (Florin, Moy et al. 1994). In this method a single or multiple ligand/receptor pairs are pulled apart at a controlled rate, and the force required for breaking the intermolecular binding is measured as a function of the applied loading rate. For the implementation on an AFM based DFS, the ligand molecules are immobilized on the AFM probe, while the receptor species are fixed on the substrate. The functionalized AFM probe with ligand is then brought into contact with receptor to establish a ligand-receptor bond, and subsequently pulled away at a controlled rate to break the bond. The measurements of this bond break force are performed a large number of times in order to obtain a statistically significant measure of the force interaction between the pair. This method has been used to determine the binding specificity and strength for biotin-avidin (Florin, Moy et al. 1994), single-stranded DNA pairs (Strunz, Oroszlan et al. 1999), alkanethiols (Oncins, Vericat et al. 2008), and many other complementary chemical species. Binding forces for these interactions were determined to be in the range of 30 to 150 pN (Basnar, Elnathan et al. 2006).

1.4 Molecular dynamics simulation on monolayer thin film under electrostatic stimuli

Self-Assembled Monolayers (SAM) have attracted increasing interest as an active smart surface for applications in micro/nano electronics (Schon, Meng et al. 2001; Schon, Meng et al. 2001; Fan, Yang et al. 2002; Stapleton, Harder et al. 2003; Fan, Yao et al. 2004), microfabrication (Ulman 1990; Jackman, Wilbur et al. 1995; Wilbur, Kumar et al. 1996; Azzaroni, Schilardi et al. 2003; Liu and Cui 2005), nanotribology (Srinivasan, Houston et al. 1998; Maboudian, Ashurst et al. 2000; Sundararajan and Bhushan 2001), and several biomedical fields (Kane, Takayama et al. 1999; Zhao, Wang et al. 2011). These monomolecular assemblies can undergo conformational transition through application of external stimuli, such as temperature, pH of solvent, application of electrical fields, and electrochemical modifications (Vemparala, Kalia et al. 2004). Among different external stimuli, application of external electrical fields is a practically feasible and effectively controllable method without any detrimental influence on the chemical stability of SAM.

All atom molecular dynamics (MD) simulation can serve as a computational tool to identify the influence of electrical field on conformational transitions and film structure of SAMs. Vemparala et. al. (Vemparala, Kalia et al. 2004) conducted MD simulation to investigate the electrical field induced conformational transition of fully packed polyethylene glycol (PEG) SAMs. Due to the polar nature of glycol end groups, the electrical field triggered the conformational transition from “all-trans” state to “gauche” state in the end groups. However due to the limited spatial availability in the fully packed structures, the overall order and backbone chain orientation remained undisturbed during electrical field application.

Several research groups have applied MD simulation to study the structural transition and its influence on frictional behavior of SAM. Harrison et. al. (Brenner, Harrison et al. 1991; Harrison, White et al. 1992; Harrison, White et al. 1995; Harrison, Mikulski et al. 2001; Mikulski and Harrison 2001; Harrison, Schall et al. 2008) introduced AIREBO potential to simulate structural and tribological properties of alkane SAMs using various materials such as carbon nanotubes, diamond surfaces, amorphous carbon surfaces and fullerenes as the indentation and sliding counterfaces. They compared odd number carbon (C_{13}) with even number carbon (C_{14}) system which differs in the orientation of the last carbon–carbon bond. The analysis of the probability distribution of methyl angle showed that the odd system has a comparatively larger extent of deformation, and a greater likelihood of gauche defects than the even system. Detailed sliding-direction force distribution suggested that the odd system contains a greater fraction of atoms that are capable of generating small pushing and resisting forces, while the even system prevails in enduring large pushing and resisting forces. They also reported that the flexible hydrocarbon SAMs can significantly reduce the mechanical excitation in the form of vibrational and rotational energy upon the interface lattice layers during sliding, thus effectively lowering the frictional resistance. They also discovered the friction coefficient increases with increasing applied normal load and decreasing temperature for certain crystallographic sliding directions, whereas it is approximately independent of sliding velocity. Chandross et. al. (Chandross, Webb et al. 2004;

Chandross, Lorenz et al. 2005) used MD simulation to study the adhesion and friction between ordered and disordered SAMs on silicon dioxide substrate. They introduced the disorder into SAMs by removing randomly selected chains from the originally well ordered crystalline substrate to generate defects and attaching chains onto an amorphous substrate. By applying relatively slow shear velocities and constant pressures onto SAMs, typical stick-slip motion was observed in full coverage ordered SAMs and disappeared in disordered one. Compared with the full coverage ordered SAMs, the friction coefficient of the disordered SAMs was found to be not sensitive to the coverage density, chain length and substrate.

In summary, polar end groups such as carboxyl and glycol can generate conformational transition via application of electrical fields due to the non-concentric charge distribution of the polar groups. Simulation results show that the orientation of bonds in functional groups and crystallographic directions influence friction responses to a large extent for dense and ordered SAMs, and characteristic phenomena such as stick-slip motion and periodicities of friction were observed. For sparse and disordered SAMs, the coverage density and chain length were found not to influence frictional performance. However, the study on frictional performance change of sparse and dense monolayer films due to large conformational transition induced by external stimuli is far from sufficient, which should be further clarified in our research.

CHAPTER 2. ELECTROSTATIC ACTUATION BASED MODULATION OF INTERACTION BETWEEN PROTEIN AND DNA APTAMER

(A paper prepared for submission to Nano Letters)

Xiao Ma, and Pranav Shrotriya

Department of Mechanical Engineering, Iowa State University, Ames, IA 50011

2.1 Abstract

The need to design nanoscale, sensitive and flexible biotic-abiotic interface keeps increasing. The essential issue is how to facilitate biological signal transmission and modulation through controllable external stimuli. This requires a thorough understanding of the binding and dissociation process between bio-molecules under the stimuli. The purpose of this study is to demonstrate the binding and dissociation behavior between the coagulation enzyme thrombin and single-stranded DNA aptamer with application of electrical fields. Micro-contact printing was utilized to prepare compositionally patterned gold specimen with adjacent regions covered with alkanethiol and DNA aptamer molecules, then thrombin molecules were injected into the system to form the binding pair with aptamer. Different electrical field potentials were applied to the nanoscale structure by a three-electrode electrochemical cell. Due to the negatively charged nature of aptamer DNA strands, positive electrical field can trigger a large bending-down conformational transition of the aptamer, thus can break the bonds between binding pair.

Through Atomic Force Microscopy, height of the pattern was measured and the difference of height under different potentials can show the binding state of the pair. We can thus propose a method to actuate and modulate the dissociation behavior between thrombin and aptamer through the external electrostatic stimuli.

Keywords micro-contact printing; atomic force microscopy; thrombin; DNA aptamer; electrostatic actuation and modulation

2.2 Introduction

Exquisite integration of artificial components with biological systems for building seamless biotic-abiotic interface has recently attracted increasing interest and attention. The nanoscale, structural and functional biotic-abiotic interface can lead to highly sensitive, biocompatible and flexible bio-sensors and actuators, which have enormous and broad applications in biomedical, and biomechanical fields, such as modulating biological systems and bio-molecule activity, locating disease, and repairing or reprogramming genetic information (Wong, Almquist et al. 2010), etc. Currently one of the major challenges on the biotic-abiotic interface design is to dynamically translate external stimuli into biochemical signals and efficiently transmit such signal into the biological processes.

There are various kinds of external stimuli that can be applied to communicate information in biotic-abiotic interface and influence biomelecular interactions, and thus different mechanisms could be adopted for actuation and modulation of the interactions in biomolecular systems. Hianik et al. (Hianik, Ostatna et al. 2007) investigated the influence of electrolyte ionic strength and pH on binding affinities between thrombin and 32 mer DNA aptamer. They changed the concentration of NaCl in the buffer solution from 0 to 500mM, and found the binding affinity between the pair decreased three folds, which might be caused by the shielding effect of the negative charges on DNA aptamer as well as on protein surface. They also tested the binding affinities of the pair under three electrolyte pH levels: 4.5, 7.5 and 8.8, and found the neutal pH conditions resulted in four folds binding affinity as the acidic and basic pH conditions. Nguyen et al. (Nguyen, Pei et al. 2011) characterized the temperature-dependent biomolecular interactions for the binding between L-arginine vasopressin and its RNA aptamer spiegelmer. They observed that the binding affinity of the pair reached the higher level under 36 to 45 ℃, while maintained the lower level under two temperature zones (25 - 33 ℃ and 50 - 65 ℃). Willner et al. (Willner 2005) utilized the electron transfer mechanisms of redox-active protein to implement electrochemical activation of surface-attached proteins, and successfully enhanced glucose oxidase and lactate dehydrogenase catalysis. However, it should be noticed that this method just applied to small sets of proteins and delicate synthetic modification was generally required (Gray and Winkler 1996).

Compared to above modulation mechanisms, electrostatic actuation has its own advantages on allowing massively parallel actuation, measurement capabilities and link to extensive semiconductor processing and circuit design, that could ultimately be essential for biomedical applications (Wong, Footer et al. 2008; Wong and Melosh 2009;

Wong and Melosh 2010). In addition, application of electrostatic fields is an efficient and feasible mechanism to induce conformational transition of charged or polar bio-molecules. When applying electrical fields onto a biological system, the double layer formed near the electrode leads to generation of strong electrical fields within several nanometers, thus only affects the bio-molecules that are immobilized on or close to the electrode surface, which implies relatively low external voltages can induce substantial conformational transition of the bio-molecules without generating harmful byproducts. Rant et al. (Lahann, Mitragotri et al. 2003; Rant, Arinaga et al. 2004; Arinaga, Rant et al. 2007) demonstrated that the conformation of short DNA oligomers immobilized at low grafting densities can be reversibly switched by application of electrical fields. Since DNA is negatively charged, positive voltages caused the DNA to flatten on the surface, while negative voltages caused the DNA to orient vertically. Wong et al. (Wong and Melosh 2009) found electrostatic fields can influence self-assembly and hybridization of DNA. Positive voltages (+300 mV) applied to single-strand DNA functionalized gold electrodes showed a three-fold enhancement in complementary DNA hybridization, while for negative voltage it was an order of magnitude smaller.

Besides applicable external stimuli, it is also essential to select an appropriate model bio-molecular system to investigate the specific response. The coagulation protein thrombin and its aptamer provide such a relevant and suitable sample model. Nucleic acid aptamers are a relatively new recognized type of molecules, with similar properties of ligand specificity and affinity to antibodies but having several specific advantages as components of sensors and biomedical devices (Ellington and Szostak 1990; Tuerk and

Gold 1990; Hermann and Patel 2000). They are small (15 to 40 nt) with high affinities to proteins and other large bio-molecules (k_d values are in the picomolar to nanomolar range), and demonstrate exquisite specificities for their receptors due to large structural changes in the binding process, which can be utilized for detection of the target (Jenison, Gill et al. 1994; Yang, Kochoyan et al. 1996), selection of various bio-molecules(Lavrik, Sepaniak et al. 2004; Gronewold, Glass et al. 2005; Hianik, Ostatna et al. 2005) and biomedical materials and drugs (Wang and Rando 1995; Stojanovic, de Prada et al. 2001; Win, Klein et al. 2006). Thrombin is a catalytic enzyme taking effect in the synthesis of fibrin from fibrinogen during the blood clotting process, has a wide range of health effects in the human system (Bode, Mayr et al. 1989). Thrombin has a well established aptamer, which shows a hairpin structure formed by eight guanine bases sequenced in GGNTGGN2-5GGNTGG, known as G-quadruplex. The aptamer can fit into thrombin heparin binding site and affects the thrombin in the similar way as heparin (Bock, Griffin et al. 1992). This aptamer has been shown in chemical assays to have high binding affinity (Bode, Mayr et al. 1989; Tsiang, Gibbs et al. 1995; Tasset, Kubik et al. 1997). The strong and specific binding between thrombin and aptamer makes it suitable for current study.

In order to verify the actuation and modulation on the model biomolecular system via electrostatic stimuli, the binding specificity and affinity between thrombin-aptamer pair must be first proved. Micro-contact printing (μCP), a widespread method for creating micro and nanoscale structures outlined by Kumar and Whitesides (Kumar and Whitesides 1993), is utilized for this purpose by generating the height changes upon binding of thrombin/aptamer pair, and the height change was characterized by Atomic Force Microscopy surface imaging. After the specific binding between thrombin and aptamer was verified, different electrical fields were exerted on the pair and AFM surface imaging was utilized again to characterize the height changes, and compare to the results of nonelectrical field situation so as to acquire the information of binding or dissociation state of the pair.

2.3 Methods

2.3.1 Test of binding specificity

All chemicals required for the experiments were purchased from Sigma Aldrich (www.sigma.com), and all oligonucelotides were purchased from Integrated DNA Technologies (www.idtdna.com). All solutions were prepared with double distilled water (ddH2O).

The scheme of building nanostructure of hexadecanethiol, aptamer and thrombin in a series of steps is shown in Fig. 2-1. To perform micro-contact printing, a flexible polymer poly(dimethyl siloxane) (PDMS) stamp was made from a mold using a AZ3514 photoresist master, with 5 μm diameter pattern and 10 μm spacing among patterns. The PDMS was cured at 60 ℃ for a minimum of 12 hours. Then hexadecanethiol was exposed to the stamp as a ink in liquid, and the liquid was dried with a gas such as nitrogen. The dried hexadecanethiol was then printed and adhered on a substrate with a known distributed pattern. The PDMS stamp was removed, leaving the pattern of the hexadecanethoil printed on the substrate.

After that a solution containing 3.4 μM 5' thiolated thrombin aptamer (HS-GCCTTAACTGTAGTACTGGTGAAATTGCTGCCATTGGTTGGTGTGGTTGG) in ddH_2O was exposed to the substrate. Due to the strong covalent bonds between gold substrate and thiol group, hydrophicility of the aptamer molecules, and well packed hexadecanethiol chains, aptamer molecules can only be immobilized on the bare gold surfaces, i.e. the spacing area among the hexadecanethiol patterns, leading to a compositionally patterned sample.

To bind the aptamer with thrombin, 10 μM concentration of thrombin in binding buffer with Tween20 included to decrease non-specific binding (20 mM Tris-HCl, 140 mM NaCl, 5 mM KCl, 1 mM $CaCl_2$, 5 mM $MgCl_2$, 5% glycerol v/v and 0.05% Tween20 v/v in ddH_2O at pH 7.4) was deposited on the printed surface. The mixture was allowed to stand for 1 minute before being rinsed several times in binding buffer with NP40 included (20 mM Tris-HCl, 140 mM NaCl, 5 mM KCl, 1 mM $CaCl_2$, 5 mM $MgCl_2$, 5% glycerol v/v and 0.05% NP40 v/v in ddH_2O at pH 7.4) followed by rinsing several times with ddH_2O.

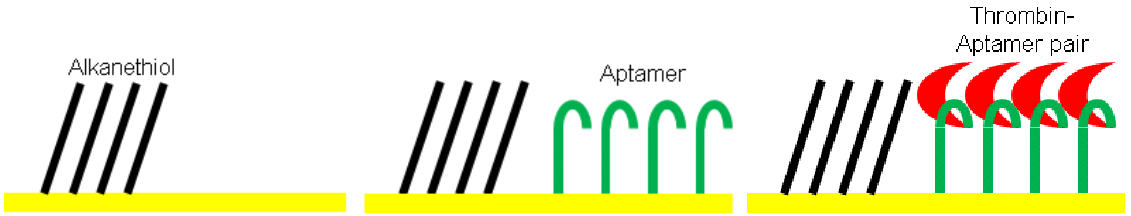

(a) Hexadecanethiol printed (b) Aptamer deposited (c) Thrombin bound with aptamer

Fig. 2-1 Schematic procedure for establishing the binding pair nanostructure in a compositionally patterned sample

Atomic Force Microscopy surface imaging was then utilized to measure the height change of the surface with 12 runs for each situation independently to acquire sufficient statistical significance, and different operators involved in the data analysis of the AFM surface topographic image so as to eliminate or reduce the bias of the measurement.

In order to test the binding specificity, two control groups of binding pair supposed to have non-specific binding or non-binding features were considered in the experiment. One is aptamer and γ-thrombin, the other is 5’ thiolated poly A (pHS-A30) and thrombin. The nanostructure preparation process and AFM characterization of those pairs are similar to the above procedures for objective pair (aptamer-thrombin).

2.3.2 Test of electrical field influence

Based on the nanostructure built as Fig. 2-1 (c), i.e. the bound state of aptamer and thrombin, different electrical field strength of -300mV, -100mV, 0mV, 100mV and 300mV were applied onto the structure respectively for 1min each via regular three electrode system, as shown in Fig. 2-2. The sample serves as the working electrode, while a silver wire is used as a reference electrode and platinum wire as a counter electrode to maintain the constant potential value. After electrical fields were removed, we utilize AFM surface imaging again to validate the height change of the surface with 12 runs for each potential condition.

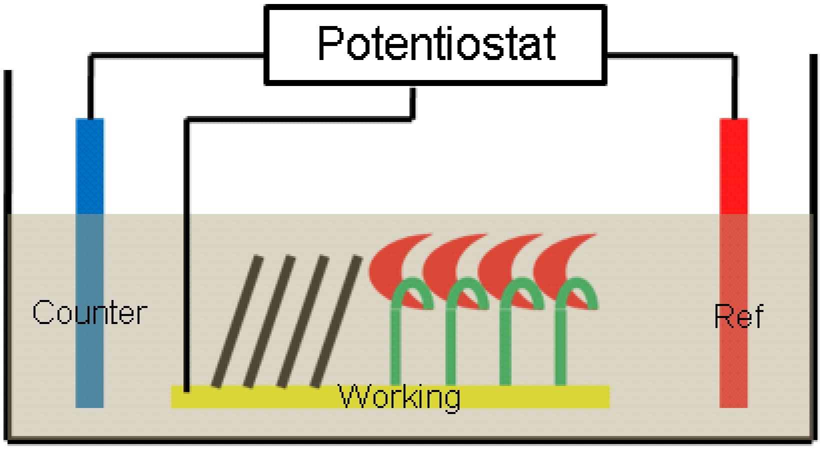

Fig. 2-2 Setup of three electrode system for testing electrostatic interaction

By applying the electrical field onto the binding pair nanostructure, there might be two possible states for the sample, as shown in Fig. 2-3. The binding pair may resist the external electrical field influence and maintain the structure, as shown in Fig. 2-3(a), then the height stateof the sample measured by AFM surface imaging will keep the same level as the case shown in Fig. 2-1(c); or the electrical field can break the pair, as shown in Fig. 3(b), then the height state of the sample measured by AFM surface imaging will be changed and showed as the case shown in Fig. 2-1(a) or (b).

(a) Bound state of the pair

(b) Dissociated state of the pair

Fig. 2-3 Schematic of bound and dissociated state of the thrombin-aptamer pair

The data analysis scheme of the AFM topographic images is shown in Fig. 2-4. On each AFM image, a 3 um × 3 um section area was selected from the pattern center (denoted as the diagonal-line square) to calculate the height for the pattern, and four 3 um × 3 um section areas surround the pattern was selected (denoted as the vertical-line square) to calculate the average value of background height. Then the subtraction of the pattern height from the background height rovided the height difference information for each image.

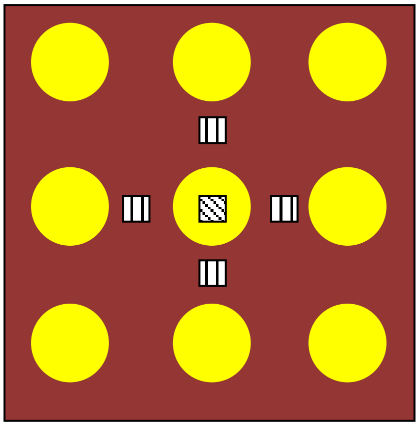

Fig. 2-4 Image processing scheme for height analysis

2.4 Results and Discussion

2.4.1 Test of binding specificity

The AFM surface topographic images under non-electrical field conditions are shown in Fig. 2-5, Alkanethiol was first printed onto gold substrate with the assigned pattern, the average height difference between alkanethiol and gold surface is -1.7 nm (gold height – alkanethiol height) through data analysis. Then aptamer molecules were printed on gold surface, since the alkanethiol occupies the position of round pattern, aptamer can only reside on the bare gold substrate area among the alkanethoil patterns, and the average height difference between the alkanethoil and aptamer became -0.5 nm (aptamer height – alkanethiol height), which implies the height of aptamer is 1.2 nm. Finally thrombin molecules were deposited onto the alkanethiol / aptamer surface and could specifically bind to aptamer. The binding between thrombin and aptamer increases the height to a large extent, so that now the pair shows greater height than alkanethiol, and that's why an inverse image was observed compared to the previous two cases. The relative height difference between the thrombin-aptamer pair and alkanethiol became -1.4 nm (aptamer + thrombin height – alkanethiol height), which implies the height of thrombin is 1.9 nm. This height change is summarized in Table 2-1 to show the size scale of alkanethiol, aptamer and thrombin in the binding process.

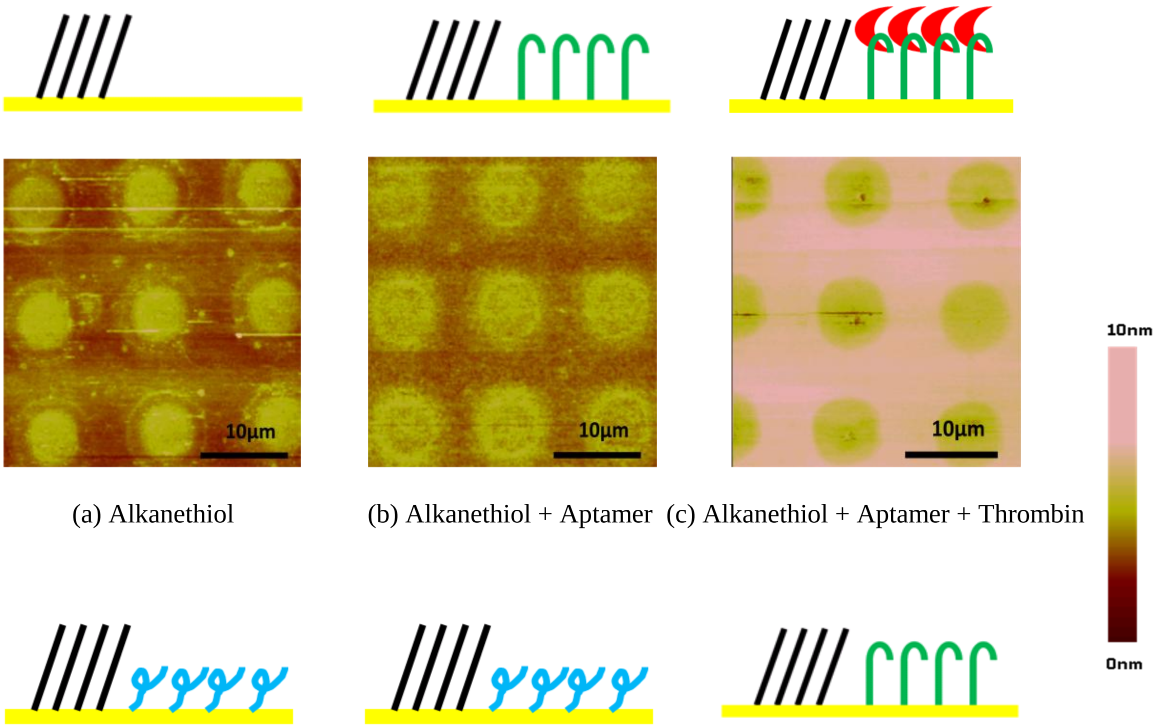

(a) Alkanethiol (b) Alkanethiol + Aptamer (c) Alkanethiol + Aptamer + Thrombin

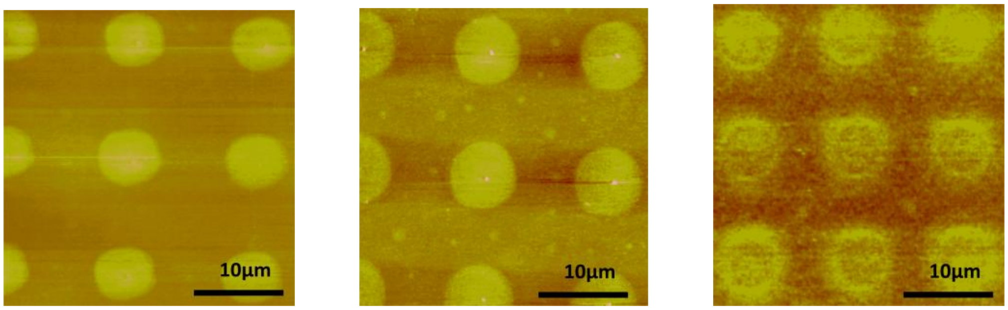

(d) Alkanethiol + polyA (e) Alkanethiol + polyA + Thrombin (f) Alkanethiol + Aptamer + γ-Thrombin

Fig. 2-5 AFM images of non-electrical field conditions

(The blue coil in (d), (e) is polyA)

Table 2-1 Height change summary of μCP experiment

	Alkanethiol vs Gold	Alkanethiol vs Aptamer	Alkanethiol vs Thrombin-Aptamer pair
Height difference (nm)	-1.7 ±0.2	-0.5 ±0.2	1.4 ±0.2
	Alkanethiol	Aptamer	Thrombin
Height of molecules (nm)	1.7 - 0 = 1.7	1.7 – 0.5 = 1.2	1.7 + 1.4 – 1.2 =1.9

For the control groups, no matter for the case of depositing thrombin onto polyA, or the case of depositing γ-thromibin onto aptamer, we didn't observe a reverse image to appear, which implies that there is no specific binding between those pairs, and thus confirm the specific binding between aptamer and thrombin.

Detailed statistical results support our conclusion. Through the Shapiro-Wilk W Goodness-of-Fit Test (Shapiro and Wilk 1965), all p-values are larger than $\alpha = 0.05$, which implies all samples can be acknowledged as normal distributions. The confidence intervals (95%) of those samples based on normal distribution assumption can be found in Appendix Table 2-1. In order to further ensure the inference from the statistical test, we adopted another method bootstrap to resample the data (Efron 1979; Efron 1993), which does not rely on any distribution assumtions and allows replacement during the resampling process to generate the distribution. The resampling number was set to be N = 1000, then corresponding confidence intervals (95%) of those resampling distributions can also be found in Appendix Table 2-1 (More detailed description of bootstrap resampling process is also described in Appendix). It can be seen that the statistical results have very good agreement on normal distribution assumption and bootstrap resampling, which further confirm the inference from the test.

The summarized statistical results from the bootstrap reampling are shown in Fig. 2-6. We observed that there is no overlap of the confidence intervals for the three cases in objective group, which implies there are statistically significant differences among them. Thus we can take the height difference as the indicator of the binding states, and make it as a model for determination of the binding states in the next step of the experiments. For poly A control group, we observed that no matter adding the thrombin or not onto polyA, the confidence intervals have almost overlap with each other, which implies they isn’t statistically significant difference between them, so there is no specific binding between polyA and thrombin. For γ-thrombin control group, we observed that compare to thrombin added to aptamer, after adding γ-thrombin onto aptamer, there is no overlap of the confidence intervals for the two cases, which means there is statistically significant difference between them, and thus there is no specific binding between aptamer and γ-thrombin.

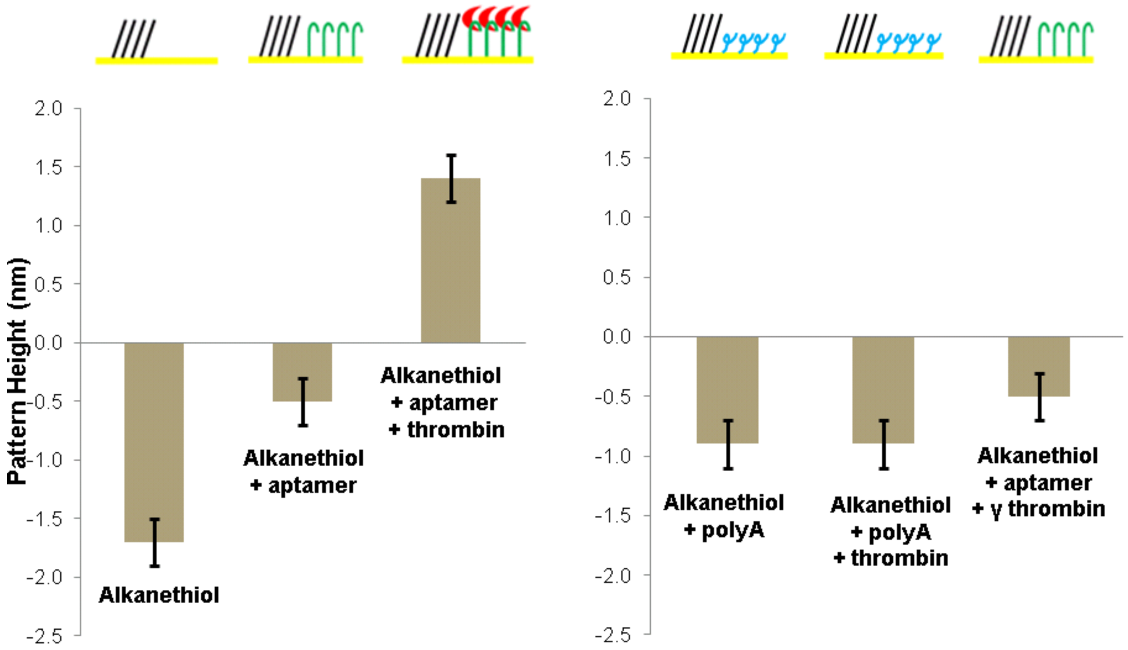

(a) Height difference of objective group (b) Height difference of control group

Fig. 2-6 Statistical results of AFM surface height measurement results for nonelectrical field application

2.4.2 Test of electrical field influence

After electrical fields were applied onto the aptamer and thrombin pair (as shown in Fig. 2-5 (c)), based on the data model showed in Fig. 2-6(a), we can determine the influence of electrical fields on the binding states of the pair. AFM surface topographic images under electrical field conditions are shown in Fig. 2-7. When 0mV was applied to the system, as shown in Fig. 2-7(c), the image has the same feature as Fig. 2-5(c), which means the pair structure was well maintained under zero volt condition. When positive electrical fields were exerted onto the binding pair (both 100mV and 300mV), due to the negatively charged nature of the DNA aptamer, the electrostatic force pulled the aptamer down onto the gold substrate, which can break the bonds between thrombin and aptamer, thus led to the case shown in Fig. 2-7(d) and Fig. 2-7(e). The image is inversed and height difference value changes from 1.4 nm to -0.5 nm. While negative electrical fields exerted onto the system, for a smaller field strength value -100 mV, as shown in Fig. 2-7(b), we found the height difference value to be 1.4 nm, i.e. keep the bound state level of the pair, which means the pair can resist the electrostatic pushing force and maintain the structure. However, for a larger field strength value -300 mV, as shown in Fig. 2-7(a), we found the height difference value change enormously from 1.4 nm to -1.7 nm, which implies not only the thrombin was removed from the surface, but also the aptamer was eliminated from the surface due to the much greater electrostatic pushing force. In this way, we propose a method to actuate and modulate the binding behavior between thrombin and aptamer by applying moderate electrical field strength ranging from -100 mV to 300 mV.

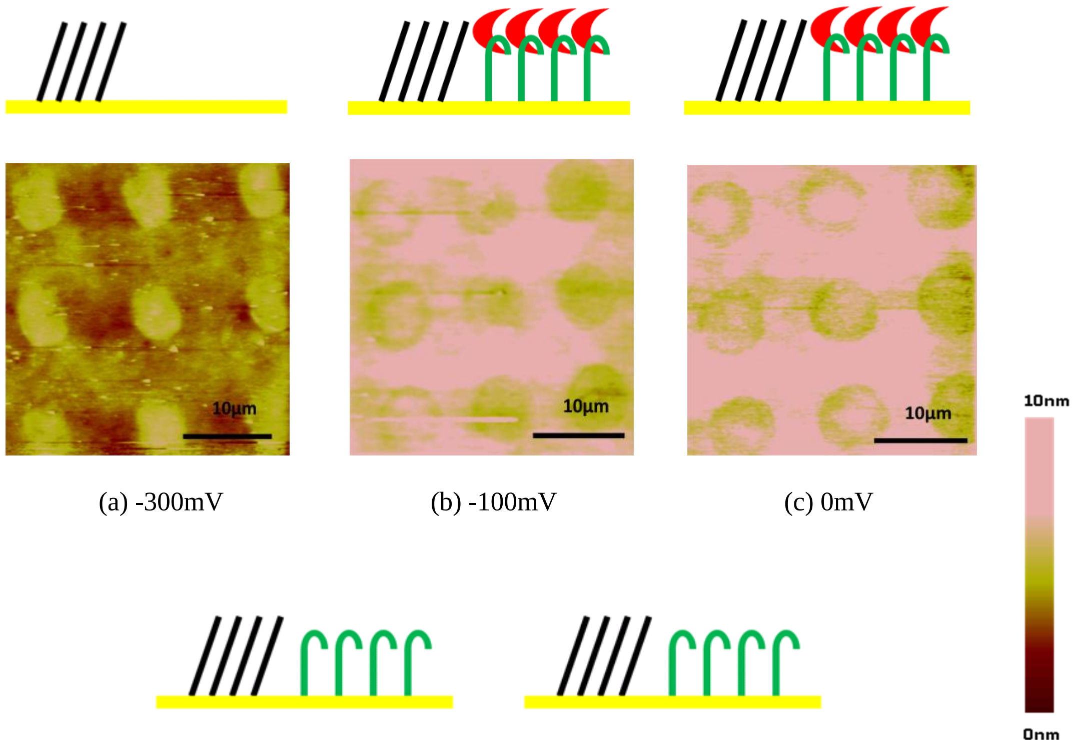

(a) -300mV (b) -100mV (c) 0mV

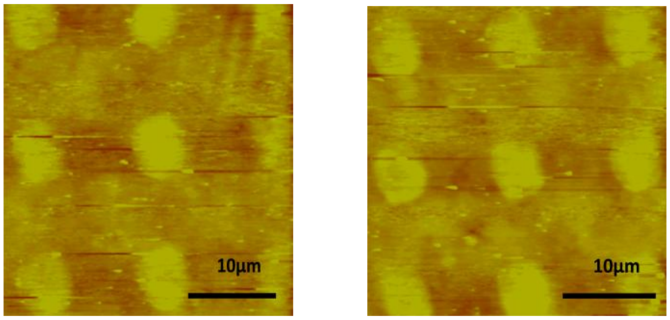

(d) 100mV (e) 300mV

Fig. 2-7 AFM images of electrical field applications

Detailed statistical results of confidence intervals on both normal distribution and bootstrap resampling (N = 1000) could be found in Appendix Table 2-2. The summary of those experimental results can be further highlighted in Fig. 2-8. For 0mV and -100mV, as shown in Fig. 2-8(b), the confidence intervals almost overlap with the case of alkanethiol + aptamer + thrombin shown in Fig. 2-8(a), which implies there is no statistically significant difference among them. Thus we can conclude that the binding states of the pair can be maintained under 0mV and -100mV. For 100mV and 300mV, as shown in Fig. 2-8(b), the confidence intervals almost overlap with the case of alkanethiol + aptamer shown in Fig. 2-8(a), which implies there is no statistically significant difference among them. So we can conclude that the thrombin has been removed from the aptamer under 100mV and 300mV. For -300mV, as shown in Fig. 2-8(b), the confidence interval almost overlaps with the case of alkanethiol shown in Fig. 2-8(a), which implies there is no statistically significant difference between them. Hence we can conclude that both thrombin and aptamer have been removed from the gold substrate under -300mV.

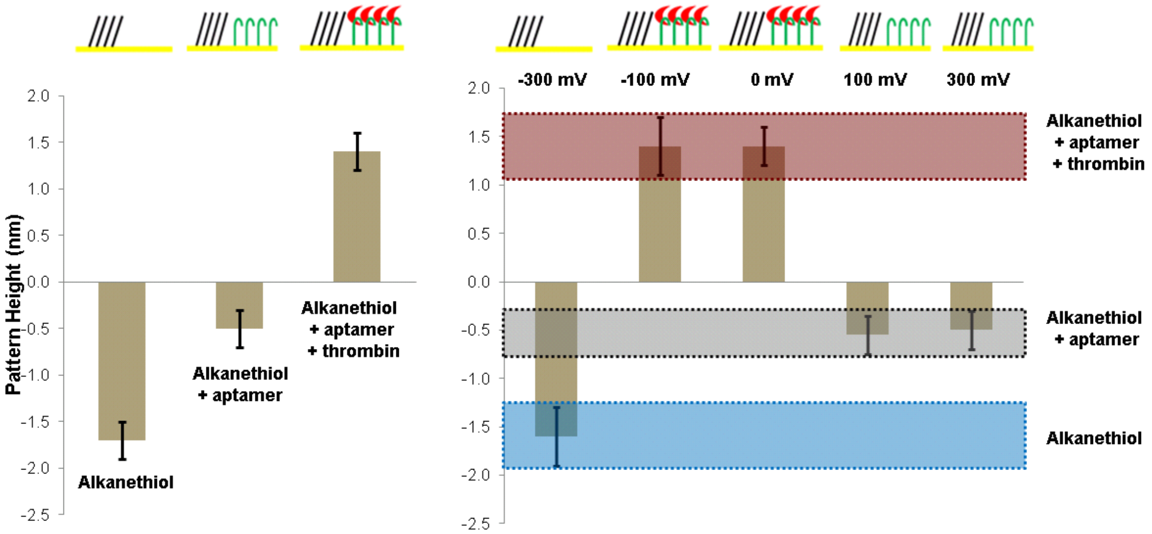

(a) Height difference of nonelectrical field (b) Height difference of electrical field

Fig. 2-8 Statistical results of AFM surface height measurement results for nonelectrical / electrical field application

2.5 Conclusion

We could draw the following conclusions based on this studies on electrostatic actuation based modulation of the binding behavior of thrombin and DNA aptamers.

1) Through uCP technique, thrombin-aptamer binding pair can be successfully established.

2) By performing height identification experiment through AFM surface imaging, the binding specificity between thrombin and aptamer can be verified.

3) Moderate electrical fields can be utilized to induce binding change between thrombin and aptamer pair, and thus can realize the actuation and modulation of the binding behavior between the pair:

3a) Positive electrical fields of 100 mV can successfully break the bonds between the aptamer-thrombin pair;

3b) Neutral condition does not influence the binding between the pair;

3c) Negative electrical fields of -100mV can withhold the pair structure; while At -300mV, the whole binding pair is stretched away from the gold substrate and the nanostructure was destroyed due to the too large electrostatic pushing force.

2.6 Appendix

Bootstrap resampling:

For each sample of 12 data, we treated it as the whole population, and resampled the data following the replacement rule, i.e. we picked up a data from those 12 data randomly, then put back the data in the pool to allow another data pick-up. Such resampling was repeated for many times, in our case, the resampling times N = 1000. Then the 1000 resampling data generated a new distribution, and we could perform the statistical analysis on this new distribution. The benefit of application of bootstrap resampling method is that there is no specific distribution assumption on the data set, and the new resampled distribution could have much more data than the original data set, thus make the statistical analysis more stable and robust.

Appendix Table 2-1 Statistical results of confidence intervals for height difference under non-electrical field conditions based on normal distribution assumption and bootstrap resampling

			Average	Lower bound	Higher bound
Objective group	Alkanethiol	Normal distribution	-1.66	-1.74	-1.58
		Bootstrap	-1.66	-1.73	-1.58
	Alkanethiol + Aptamer	Normal distribution	-0.53	-0.61	-0.45
		Bootstrap	-0.53	-0.60	-0.46

	Alkanethiol + Aptamer + Thrombin	Normal distribution	1.40	1.30	1.50
		Bootstrap	1.40	1.32	1.48
Control group	Alkanethiol + polyA	Normal distribution	-0.92	-1.04	-0.80
		Bootstrap	-0.92	-1.02	-0.82
	Alkanethiol + polyA + Thrombin	Normal distribution	-0.89	-1.06	-0.73
		Bootstrap	-0.89	-1.03	-0.76
	Alkanethiol + Aptamer + γ-Thrombin	Normal distribution	-0.55	-0.64	-0.46
		Bootstrap	-0.55	-0.62	-0.48

Appendix Table 2-2 Statistical results of confidence intervals for height difference under electrical field application based on normal distribution assumption and bootstrap resampling

		Average	Lower bound	Higher bound
0mV	Normal distribution	1.43	1.33	1.54
	Bootstrap	1.43	1.34	1.52
100mV	Normal distribution	-0.55	-0.67	-0.43
	Bootstrap	-0.55	-0.66	-0.45
300mV	Normal distribution	-0.53	-0.63	-0.42
	Bootstrap	-0.53	-0.61	-0.44
-100mV	Normal distribution	1.41	1.33	1.50
	Bootstrap	1.41	1.32	1.51
-300mV	Normal distribution	-1.63	-1.77	-1.50
	Bootstrap	-1.63	-1.74	-1.51

CHAPTER 3. ATOMIC FORCE MICROSCOPE BASED FORCE SPECTROSCOPY MEASUREMENTS OF THE THROMBIN-APTAMER INTERACTION

(A paper submitted to Langmuir)

Xiao Ma[1], Janice Marquardt[1], Marit Nilsen-Hamilton[2] and Pranav Shrotriya[1]

[1] Department of Mechanical Engineering, Iowa State University, Ames, IA50011

[2] Department of Biochemistry, Biophysics, and Molecular Biology, Iowa State University, Ames, IA 50011

3.1 Abstract

Force spectroscopy is used to characterize the bond strength and binding energy between thrombin and its single-stranded DNA aptamer. Atomic force microscope (AFM) based experiments are conducted on the thrombin/aptamer and other non-specific binding systems to ensure that the measured binding forces are specific to the dissociation of the thrombin/aptamer complex. A thrombin-coated AFM tip is first brought into contact with the receptor-functionalized surface and subsequently retracted from the surface at a controlled displacement rate to dissociate the thrombin/receptor bound complexes formed during contact. The force response associated with probe retraction is analyzed to determine the force and loading rate associated with dissociation of the protein/receptor complex. Experimental results show that force curves have the characteristic sequential unbinding response and larger dissociation forces only for the combination of thrombin and the specific binding receptor (thrombin aptamer). The force curves on the non-specific binding DNAs have lower magnitudes of dissociation forces. The distribution of forces measured for different loading rates on the thrombin aptamer coated surface were analyzed to provide estimates of the dissociation force as function of loading rate associated with thrombin/aptamer complex. Experimental results show that the dissociation force increased from 20 pN to 40 pN as the loading rate was increased from 100 pN/s to 40000 pN/s. The measured dissociation force magnitudes for the thrombin/aptamer unbinding are lower than for forces associated with G-quadruplex unbinding and comparable to forces associated with DNA unfolding. A single energy barrier model for the protein/aptamer bond was utilized to compute the spontaneous dissociation time and energy barrier width from the measured dissociation forces. Computed bond parameters are compared to previously reported values obtained from chemical assays and demonstrate the efficacy of force spectroscopy-based analysis of molecular binding.

Keywords Atomic Force Microscopy Force Spectroscopy Thrombin Aptamer Single energy barrier model

3.2 Introduction

Dynamic Force Spectroscopy (DFS) has been utilized to measure dissociation forces between specific complementary chemical and biological molecules (Florin, Moy et al. 1994; Strunz, Oroszlan et al. 1999; Oncins, Vericat et al. 2008). Analysis of the unbinding forces reveals remarkable insight into energy consumption, binding kinetics and thermodynamic parameters for the molecular bonds (Flyvbjerg 2002). These advantages make it a useful tool for probing the nature and mechanism of biomolecular interactions and cellular adhesion. We report DFS-based analysis of the specific binding between thrombin and its DNA aptamer.

Aptamers are engineered nucleic acids that are selected from a random pool using the "systematic evolution of ligands by exponential enrichment" (SELEX) procedure (Ellington and Szostak 1990; Tuerk and Gold 1990; Hermann and Patel 2000), to have a high specific binding affinity towards a target biomolecule (Wallace and Schroeder 1998; Berens, Thain et al. 2001; Stojanovic, de Prada et al. 2001; Lavrik, Sepaniak et al. 2004; Gronewold, Glass et al. 2005; Hianik, Ostatna et al. 2005). Aptamers display similar specific affinity for their target analyte as antibodies and have the following additional advantages over antibodies for application to analytical platforms: stable over a larger range of temperatures and conditions; easily regenerated and reused; and easily modified or functionalized for different applications. The aptamer used in this study was selected by Tasset, et al. (Tasset, Kubik et al. 1997) to bind human thrombin. Thrombin catalyzes the synthesis of fibrin from fibrinogen so as to facilitate coagulation during blood clotting. The thrombin aptamer forms a G-quadruplex (Bode, Mayr et al. 1989; Tsiang, Gibbs et al. 1995; Tasset, Kubik et al. 1997) that fits into thrombin's heparin binding site (Kelly, Feigon et al. 1996). This aptamer has been shown in chemical assays to have high binding specificity to thrombin with a dissociation constant (K_d) of 1 to 6 nM (Wu, Tsiang et al. 1992; Tsiang, Gibbs et al. 1995). The strength of the interaction between thrombin and its aptamer makes it relevant for the study of binding forces and suitable for a force spectroscopy study.

Basnar et al. (Basnar, Elnathan et al. 2006) utilized atomic force microscope to study the disruption of the thrombin-aptamer complex at a loading rate of 3000pN/s. The force quantum associated with dissociation of the complex was calculated to be 4.45 pN by taking the peaks from the force distribution histogram and performing linear regression. The magnitude of the reported force quantum is close to the thermal force level and is significantly lower than the force magnitude of stable bond strengths reported for a G-quadruplex interacting with specific binding partners. Miyachi et al. (Miyachi, Shimizu et al. 2010) developed an AFM-SELEX cycle to select stronger affinitive DNA aptamer to thrombin under a very high loading rate level (~ 10^5 pN/s), and acquired much higher affinity force between the selected aptamer and thrombin to around hundreds of pN. Ge, et al. (Ge, Jin et al. 2012) invented an idea for testing the binding interaction via dynamic force spectroscopy between thrombin and a bivalent DNA aptamer which contains thrombin's two aptamers (15apt and 27apt) linked by eight spacer phosphoramidites, and showed that the dissociation force ranged from 60 to 150 pN under loading rates from 2000 pN/s to 5×10^5 pN/s. Lynch et al. (Lynch, Baker et al. 2009) used AFM to investigate the dissociation behavior of G-quadruplex DNA composed of 3 and 4 G tetrads, and found the most likely unbinding forces for disruption of both the 3G and 4G quadruplex structure to be from 40 to 70 pN, corresponding to loading rates from 1000 pN/s to 50000 pN/s. Pope et al. (Pope, Davies et al. 2001) used AFM to study the melting of double strand DNA and obtained the most likely unbinding forces for unzipping a 12-mer double helical DNA to be from 23 to 40 pN, which correspond to loading rates from 100 pN/s to 6000 pN/s. Using a biomembrane force probe, Erdmann et al. (Erdmann, Pierrat et al. 2008) measured the force magnitude associated with dissociation of biotin-streptavidin bonds to be from 50 to 80 pN, corresponding to loading rates from 100 pN/s to 10000 pN/s. The large difference between force magnitudes reported for thrombin/aptamer binding (4.45 pN) (Basnar, Elnathan et al. 2006) and other binding complexes (23 - 80 pN) indicates a need for closer evaluation of the thrombin/aptamer binding interactions.

Here we report the dissociation force for the thrombin/aptamer complex over a range of loading rates. The measured unbinding forces are compared to other specific binding complexes to suggest a mechanism underlying the dissociation process. The dissociation forces are also analyzed using a single energy barrier model to estimate the magnitude of spontaneous dissociation time and energy barrier width for the thrombin/aptamer interaction.

3.3 Methods

Binding forces were measured between a thrombin-coated AFM tip and three different surfaces that were functionalized with either thiolated poly(ethylene)glycol (PEG, 2 kDa) or 5’ thiolated single stranded poly(dA) (pHS-A_{30}) or 5’ thiolated 50nt-thrombin aptamers (HS-GCCTTAACTGTAGTACTGGTGAAATTGCTGCCATTGG TTGGTGTGGTTGG) (Tasset, Kubik et al. 1997). The schematic representation in Fig. 3-1 shows the probe surface interaction during the AFM based experiments. The force interaction with PEG surface was used to verify that tip the surface is functionalized with proteins. Binding forces between thrombin aptamer and single stranded DNA (poly(dA)) was used to determine the magnitude of non-specific interactions. The interactions between thrombin and thrombin aptamer were investigated to determine the binding forces associated with specific binding.

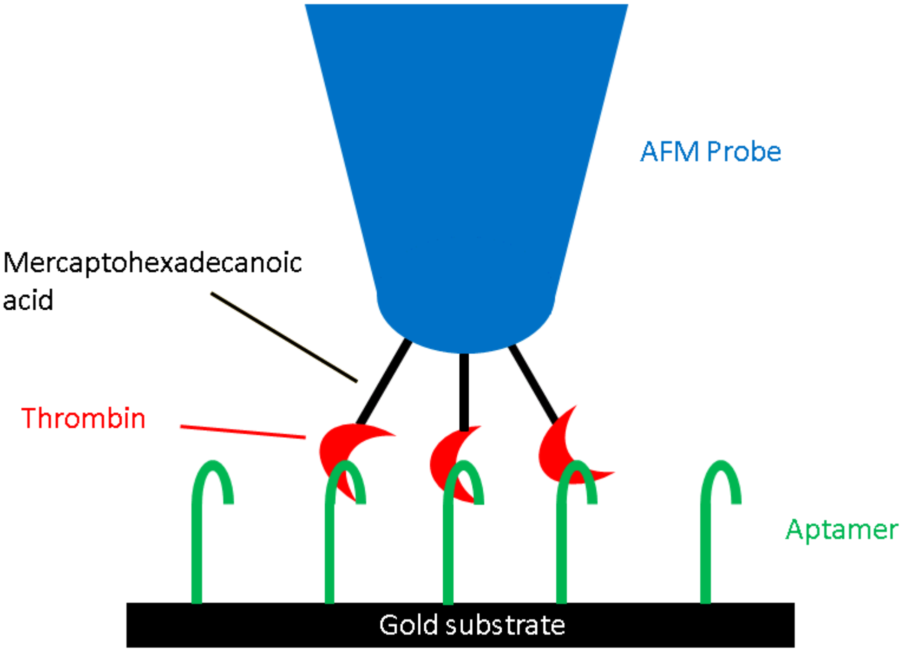

Fig. 3-1 AFM experiment configuration for force interaction measurement

All chemicals required for the experiments except PEG were purchased from Sigma Aldrich (www.sigma.com), and all oligonucelotides were purchased from Integrated DNA Technologies (www.idtdna.com). Poly(ethylene)glycol was purchased from Creative PEGworks (www.creativepegworks.com). All solutions were prepared with double distilled water (ddH_2O).

Atomic force microscope tips were coated with thrombin to measure the protein surface interactions. To functionalize the AFM tip, gold-coated silicon nitride tips were purchased from Novascan Technologies Inc. (www.novascan.com). The spring constant of each AFM tip was determined using Sader's method prior to functionalization (Sader, Chon et al. 1999). Thrombin was immobilized on the gold coated AFM tip as follows: The probe was incubated first in 2 mM mercaptohexadecanoic acid for 1 h to form a carboxyl-terminated self-assembled monolayer on the gold surface then in freshly prepared 10 mg/ml carbodiimide (EDAC) in ddH_2O for 30 min to activate the carboxylic acid groups for protein attachment. The probe was then immersed in 1 mg/ml human thrombin in buffered saline solution (137 mM NaCl, 2.7 mM KCl, 10 mM Na_2HPO_4, 5 mM KH_2PO_4 in ddH_2O at pH 7.4 as adjusted with HCl) for 90 min to immobilize the protein on the activated carboxylic acid-terminated SAM surface. Last, the probe was washed 3 times for 5 min each in buffered saline solution and 3 times for 5 min each in ddH_2O. The probe was either used immediately or stored for less than 24 h in ddH_2O before use. A single AFM tip was used to collect at the most 200 force curves and a total of 25 different AFM tips were used for the experiments reported here.

The three functionalized surfaces - PEG, poly(dA) and thrombin aptamer- were prepared by attaching the molecules to a gold-coated silicon wafer using a gold/thiol bond. A template transfer technique was used to form a smooth gold film on the polished silicon wafers. To form the PEG functionalized surface, the gold-coated silicon wafers were incubated in thiolated PEG (1 mg/mL in ethanol) for 1 min. The poly(dA)-functionalized surfaces were prepared by immersion of the gold-coated wafer in 1 mg/ml thiolated poly(dA) in binding buffer (20 mM Tris-HCl, 140 mM NaCl, 5 mM KCl, 1 mM $CaCl_2$, 5 mM $MgCl_2$, and 5% glycerol (v/v) in ddH_2O at pH 7.4) for 1 min (Basnar, Elnathan et al. 2006). Finally, the aptamer-functionalized surfaces were prepared by immersion of the gold coated silicon wafers in 1 mg/ml thiolated aptamer in binding buffer. All functionalized surfaces were rinsed several times with ddH_2O and grounded with copper tape before being used for the unbinding experiments.

Force curve experiments for all the coated substrates were performed in binding buffer using a Dimension 3100 atomic force microscope. During the experiments, the AFM tip was moved towards the sample to establish contact with surface and then retracted back to its starting location at a fixed displacement rate. The force applied to the AFM tip during surface contact and retraction was measured to obtain the force curves. The experimental study was conducted in two steps: 1) force curves were acquired on all functionalized surfaces to compare unbinding force responses for specific and non-specific interactions, and 2) force curves were acquired to investigate the load rate dependence of the force interaction associated with a specific binding event. In the initial step, force curves were obtained on the all three substrates at a nominal displacement rate of 200 nm/s. For each functionalized substrate, force curves were measured ten times per location, at 5 locations on 5 different samples, resulting in a total of 250 force curves for each functionalized surface. In the second stage, the force curves were collected only on thrombin aptamer functionalized surfaces at two different nominal displacement rates: 200 nm/s and 2000 nm/s. A total of two thousand force curves (10 samples X 20 locations/samples X 10 force curve/locations) were acquired for each displacement rate.

3.4 Results and Discussion

Representative force curves corresponding to interactions between the thrombin coated AFM tip and PEG or poly(dA) functionalized surfaces are shown in Fig. 3-2(a) and (b), respectively. Force curves corresponding to interactions between thrombin and an aptamer functionalized surface representing sequential unbinding and single unbinding are shown in Fig. 3-2(c) and (d), respectively.

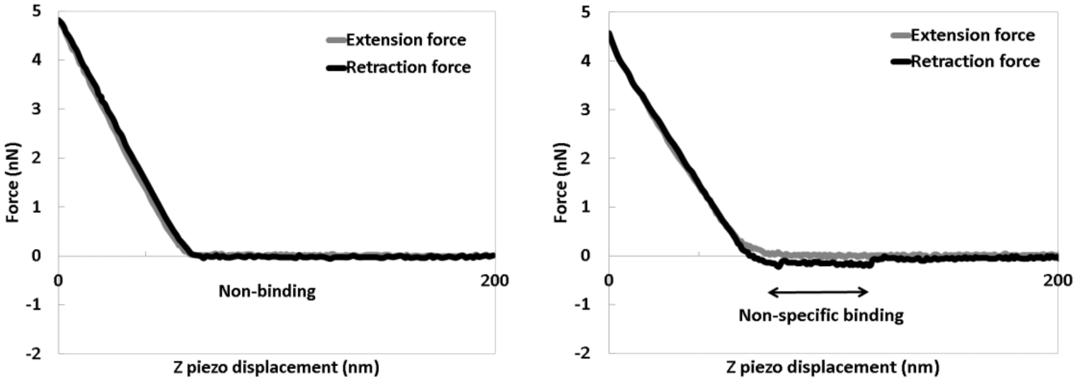

(a) PEG (b) poly(dA)

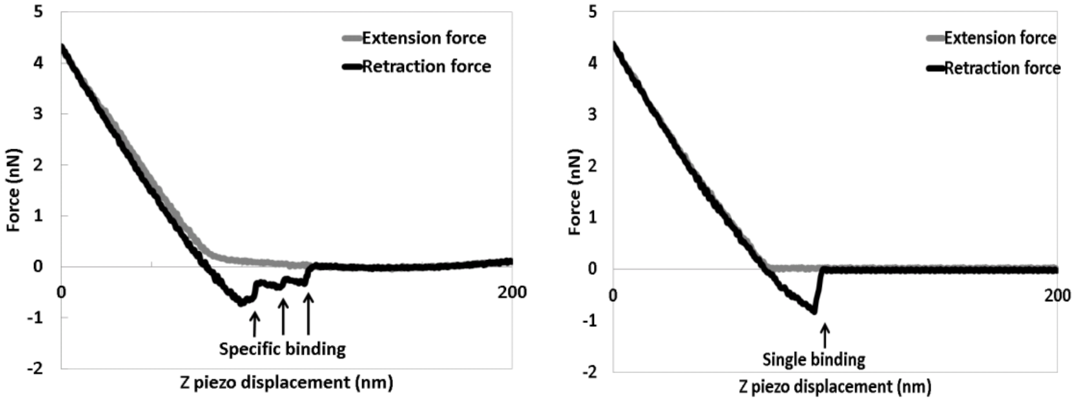

(c) aptamer (sequential unbinding) (d) aptamer (single unbinding)

Fig. 3-2 Representative force curves for thrombin coated tip interaction with the functionalized surfaces

For each functionalized surface, the force curves were collected on five different samples, five locations per samples and using 25 different AFM tips. We did not observe a systematic influence of these parameters on the measured force curves. The force curves of the thrombin coated AFM tip against the PEG functionalized surface (shown in Fig.3- 2(a)) did not show any difference between the extension and retraction of the tip. This indicates that the AFM tip did not form any bonds with PEG functionalized surface, which is consistent with the generally observed lack of interaction between PEG and proteins (Prime and Whitesides 1991; Vemparala, Kalia et al. 2004). Force curves on both thrombin aptamer and poly(dA) functionalized substrates showed binding interactions with the thrombin-coated AFM tip during retraction. However, the nature of the binding interactions observed on the poly(dA) and aptamer functionalized surfaces were very different. For poly(dA) functionalized surfaces, the retraction curves did not show obvious discrete drops in forces but rather an elongated displacement that ended with a small magnitude of force drop (labeled as non-specific binding events shown in Fig. 3-2(b)). The force curves on the thrombin aptamer functionalized surfaces included either multiple discrete stepwise drops (labeled as specific binding events shown in Fig. 3-2(c)) or a single large drop (shown in Fig. 3-2(d)) of force in the retraction curve. Discrete drops in forces have been suggested to be associated with sequential unbinding interactions between multiple bonds loaded in parallel (Pope, Davies et al. 2001; Erdmann, Pierrat et al. 2008). A comparison of these experimental observations indicates the following: 1) The difference in interactions of the aptamer-coated AFM tip with the PEG and thrombin functionalized surfaces shows that the tip was functionalized with protein molecules; (2) Binding between the protein and poly(dA) requires low magnitude forces for dissociation; (3) Binding between the protein and aptamer requires a larger magnitude of forces and the retraction curve shows characteristics that are associated with dissociation of specific binding (Pope, Davies et al. 2001).

In order to determine the dependence of the unbinding forces on the loading rate, the force curves on the aptamer-functionalized surfaces were collected at two different displacement rates of the AFM cantilever (200 nm/s and 2000 nm/s). A total of 4000 force curves (2000 corresponding to each displacement rate) were collected and could be divided into three groups – no binding event, single binding event (as shown in Fig. 3-2(d)) and multiple binding events (as shown in Fig. 3-2(c)) – and number of force curves for each group are presented in Table 3-1. Multiple discrete load drops were observed for approximately 11% of the force curves corresponding to about 452 force curves from 4000 total measurements (Erdmann, Pierrat et al. 2008).

Table 3-1 Distribution of force curves corresponding to interaction between thrombin and aptamer coated surface

	No binding	Single binding	Multiple binding
Numbers	601	2978	452
Percentage	14.9%	73.9%	11.2%

The dissociation forces and corresponding loading rates were determined from the retraction portion of force curves as shown schematically in Fig. 3-3 in order to determine the load rate dependence of the dissociation force associated with specific binding. During the dissociation experiment, thrombin and the aptamer were pulled apart at a constant displacement rate using the flexible atomic force cantilever. It is difficult to *a-priori* impose a desired loading rate during tip retraction. Instead, deformation of the AFM cantilever was used to determine the forces on the tip so the loading rate can be determined as a product of applied displacement rate and the AFM cantilever stiffness only when the tip interacts with a rigid surface as indicated by the nominal loading rate. Prior to the final unbinding rate, the imposed displacement is distributed between the AFM cantilever bending and deformation of protein/aptamer complexes. Hence the loading rate corresponding to the final dissociation is determined from the slope of the force curve just prior to the unbinding event as indicated by the loading rate for unbinding in Fig. 3-3. The dissociation force corresponding to the final dissociation event was determined from the load drop. The loading rate and dissociation force pairs were computed for each force curve that showed multiple binding events during the retraction. Only the last unbinding event of the multiple discrete force steps was used for analysis, as this last event is likely to have the fewest number of interacting bonds.

The dissociation forces determined from the force curves were categorized into four groups based on the measured loading rate for the last unbinding event – lowest loading rate (mean 90 pN/s range: 50 -140 pN/s); lower median loading rate (mean 750 pN/s and range 450- 1200 pN/s); higher median loading rates (mean 7000 pN/s and range 4700 - 9500 pN/s) and highest loading rate (45000 pN/s and range 25700 - 63900 pN/s).

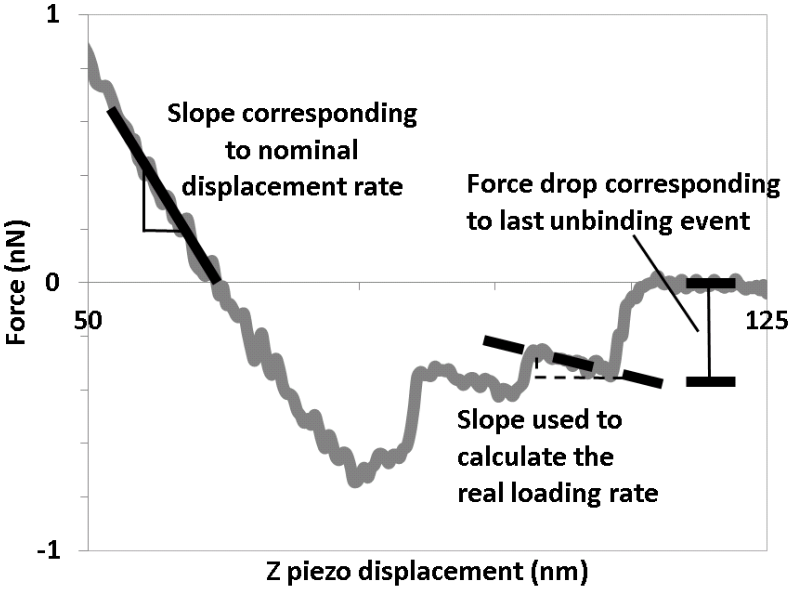

Fig. 3-3 Sample force curve for computing nominal and real loading rate

Histograms of the measured dissociation forces corresponding to specific binding at different loading rate levels – lowest, lower median, higher median and highest - are shown in Fig. 3-4(a), (b), (c) and (d), respectively. As the loading rates were increased, the range of the dissociation forces increased and the peaks in the histograms, which identify the most frequent force magnitudes, shifted towards higher magnitudes. A histogram of final load drop levels measured for a non-specific binding complex (poly(dA) and thrombin) is also plotted in Fig. 3-5 to compare the distributions corresponding to specific and non-specific binding. A comparison of the histograms show the differences in magnitude of the measured forces for specific binding (thrombin-aptamer) and nonspecific binding (thrombin-poly(dA)). For the thrombin-aptamer complex, the distribution of rupture forces shows periodic peaks in the histogram, which may indicate the existence of an elementary binding force corresponding to dissociation of a single protein/aptamer complex. In the case of thrombin-poly(dA) interaction, there are no obvious periodic peaks in the histogram of rupture forces.

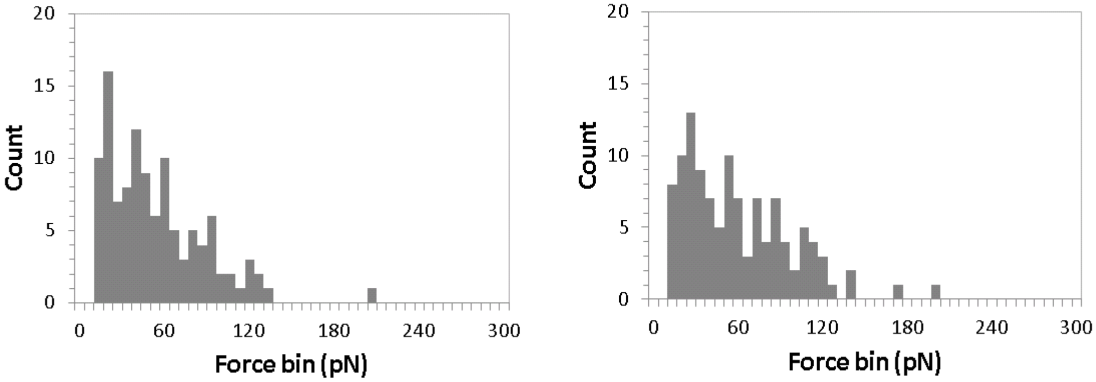

(a) Lowest real loading rate (90 pN/s) (b) Lower median real loading rate (750 pN/s)

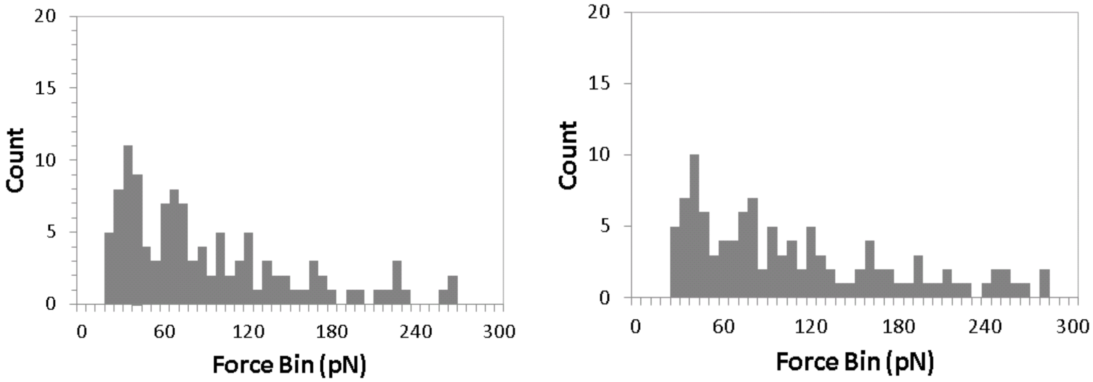

(c) Higher median real loading rate (7000 pN/s) (d) Highest real loading rate (45000 pN/s)

Fig. 3-4 Rupture force distribution of the thrombin-aptamer complex for different loading rates imposed prior to final unbinding event

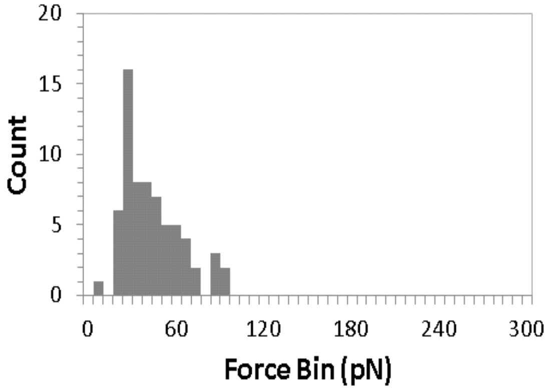

Fig. 3-5 Rupture force distribution for the thrombin-poly(dA) complex at the lowest real loading rates (90pN/s)

Auto correlations of the force distributions in Figures 4 and 5 were computed to estimate the magnitude of the elementary binding force as a function of the loading rates (Kado and Kimura 2003). For the sake of brevity, only the auto correlation functions for the force distribution corresponding to specific interaction at lowest loading rate (Fig. 3-4(a)) and non-specific interaction (Fig. 3-5) are plotted in Fig. 3-6(a) and (b), respectively. Periodically spaced peaks in auto correlation for the specific interaction (Fig. 3-6(a)) confirm the existence of the elementary binding force or the force quantum for specific binding. Similar periodically spaced peaks were observed in the autocorrelation function for other loading rate levels. However, the auto correlation function did not show periodic patterns for nonspecific binding (Fig. 3-6(b)), indicating no characteristic force quantum involved in the force interaction between thrombin and poly(dA). The period of the repeating peaks in the autocorrelation curve shown in Fig. 3-6(a) was measured to estimate the force quantum for lowest real loading level. Similar analysis was utilized to estimate the force quanta for other loading rates and the computed values for the four real loading rates are shown in Table 3-2.

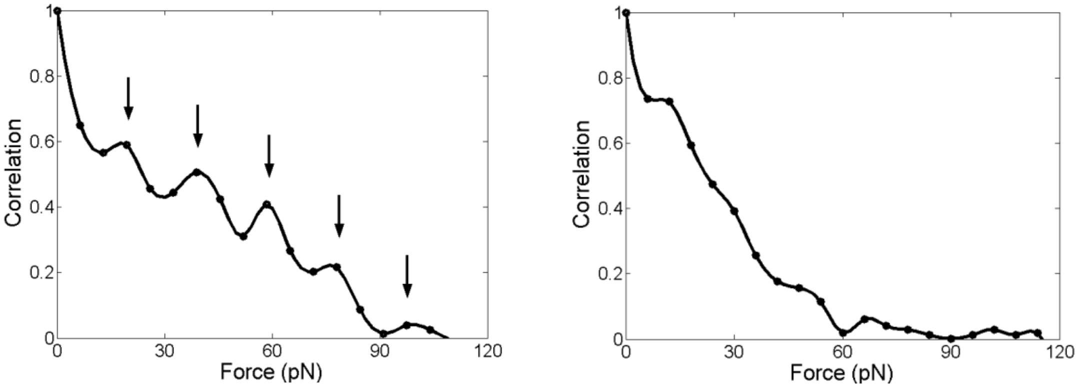

(a) Thrombin-aptamer complex (b) Thrombin-poly(dA) complex

Fig. 3-6 Autocorrelation function of rupture force distribution
at the lowest loading rates (90pN/s)

Table 3-2 Force quantum corresponding to each real loading rate region

Real loading rate (pN/s)	Force quantum (pN)
90	20
750	26
7000	33
45000	40

The characteristic rupture force of the thrombin-aptamer complex varies from 20 to 40 pN under real loading rate variations from 90 to 45000 pN/s (Table 1). The magnitude of these characteristic forces is similar to the forces of 23 to 40 pN corresponding to melting of a 12 base DNA duplex observed at loading rate ranging from 100 to 3000 pN/s (Pope, Davies et al. 2001) and 10 to 1200 pN/s (Koch and Wang 2003). Lynch et al. (Lynch, Baker et al. 2009) found the most likely unbinding forces for disruption of G-quadruplex structure formed between two DNA strands to vary from 40 to 70 pN over similar loading rates as the current experiments. Yu et al. (Yu, Schonhoft et al. 2009) found that a characteristic force of 23 – 29 pN is required to melt a G-quadruplex at loading with rates of 5 pN/s that are significantly lower than loading rates used in the current experiments. The thrombin aptamer used in this study forms a two G-tetrad quadruplex both in solution and in binding with thrombin. For the loading rates investigated in the current study, the magnitudes of characteristic forces associated with unbinding of the thrombin-aptamer complex measured in the current experiments are closer in magnitude to forces required for DNA melting than to those reported previously for disrupting G-quadruplex structures. Hence, unbinding of the thrombin-aptamer complex may result from the breaking of bonds between aptamer and thrombin rather than disruption of the G-quadruplex structure of the aptamer.

The dissociation response of protein-aptamer binding with external load may be modeled using a single energy barrier model as proposed by Evans and co-workers (Moy, Florin et al. 1994; Evans 1998; Evans 1999; Merkel, Nassoy et al. 1999; Evans 2001; Evans, Leung et al. 2001). When the thrombin-aptamer complex is not subjected to external loads, this energy barrier is quite high and results in a low probability for the complex to dissociate. When the bound complex is pulled apart under an external force, the work done by the force decreases the height of the energy barrier, and consequently increases the probability of dissociation. The probability of dissociation, p, may be expressed as a function of applied force, F as (Moy, Florin et al. 1994; Evans 1998; Evans 1999; Merkel, Nassoy et al. 1999; Evans 2001; Evans, Leung et al. 2001):

$$p(F) = \frac{F_b}{r_f t_{off}} \exp\left\{ \frac{F}{F_b} - \frac{F_b}{r_f t_{off}} \left[\exp\left(\frac{F}{F_b} \right) - 1 \right] \right\}; \text{where } F_b = \frac{k_B T}{x_b} \tag{3-1}$$

r_f is the loading rate; t_{off} is the spontaneous dissociation time; F_β is the thermal force that dominates the spread of the distribution; and x_β is the width of the transition state barrier. According to equation (3-1), a peak in the probability distribution occurs when the exponential increase in failure rate due to applied force crosses over to the precipitous decline in bond survival with increasing force (Evans 2001). The rupture force, F_{peak}, corresponding to the peak of the probability distribution with respect to loading rate is determined to be:

$$F_{peak} = F_{\beta} \ln\left(\frac{r_f t_{off}}{F_{\beta}} \right) \tag{3-2}$$

The characteristic force computed used auto-correlation analysis of the force histograms corresponds to F_{peak} at the different loading rates. The characteristic force values in Table 1 are plotted as a function of the logarithm of the average loading rate in Fig. 3-7. The line obtained by fitting equation (3-2) to the measured peak forces is also plotted in Fig. 3-7. The good agreement between the curve fit and the data shows that equation (3-2) describes the observed response and that single energy barrier model described in equations (3-1) may be used to describe the protein-aptamer interaction. The slope and intercept of the fitted line were used to determine the values of the width of transition state barrier, x_{β}, to be approximately 0.8 nm and spontaneous dissociation time, t_{off}, to be approximately 700 seconds. The estimated magnitude of the transition state barrier is comparable to the barrier width of 0.58 nm that characterizes 12 base DNA melting (Pope, Davies et al. 2001). The magnitude for the dissociation time is also within the previously reported range of 500 to 10,000 seconds measured using electrochemical impedence assays for thrombin-aptamer dissociation (Li, Shen et al. 2008). These two results suggest that a single energy barrier model may be used to describe the thrombin-aptamer dissociation over the range of loading rates used in these experiments.

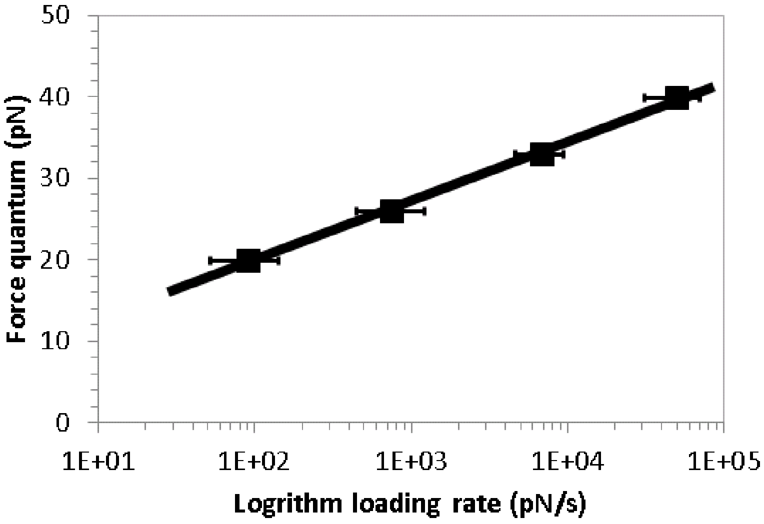

Fig. 3-7 Force spectrum: linear dependence of unbinding force on logarithm loading rate

3.5 Conclusions

AFM experiments were conducted to determine the characteristic force associated with specific binding between thrombin and its DNA aptamer. The measured rupture force distributions extend over a large magnitude of forces and demonstrate characteristics of force quanta for specific binding (thrombin-aptamer) in comparison to non-specific binding (thrombin-polyA). We find that the characteristic force for disruption of thrombin-aptamer complexes increases from 20 to 40 pN as the loading rate level increase from 100 to 40000 pN/s. The magnitude of characteristic forces is smaller than the previously reported force magnitudes associated with metling of the G-quadruplex structure. This difference suggests that, with the application of external force on the thrombin-aptamer complex, the G-quadruplex structure of the aptamer is not disrupted and the measured characteristic forces may be associated with dissociation of thrombin and the aptamer. The characteristic rupture forces were fitted to a single energy barrier model to extract the bond energy parameters associated with thrombin-aptamer binding.

3.6 Appendix

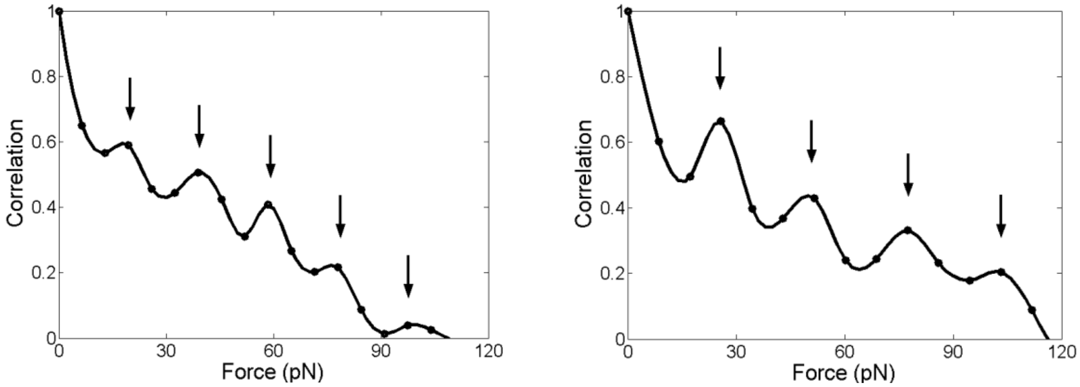

(a) Lowest loading rate (90pN/s) (b) Lower median loading rate(740pN/s)

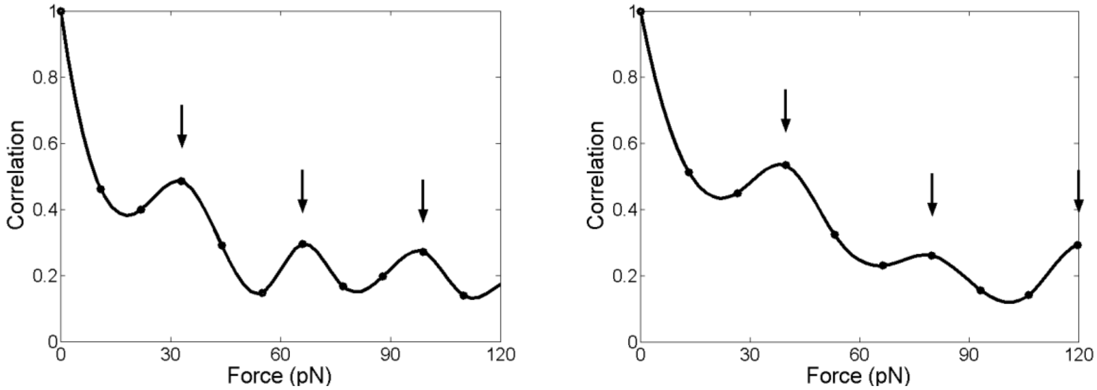

(c) Higher median loading rate (6800pN/s) (d) Highest loading rate (40000pN/s)

Appendix Fig. 3-1 Autocorrelation function of last rupture force distribution for all real loading rates

CHAPTER 4. DYNAMIC FORCE SPECTROSCOPY STUDY ON ELECTROSTATIC ACTUATION OF BINDING INTERACTION BETWEEN THROMBIN AND DNA APTAMER

(A paper prepared for submission to Biophysical Journal)

Xiao Ma, and Pranav Shrotriya

Department of Mechanical Engineering, Iowa State University, Ames, IA 50011

4.1Abstract

The application of electrical field has been proved to successfully change the binding behavior between coagulation protein thrombin and its binding pair DNA aptamer in previous studies. The purpose of this investigation is to utilize Atomic Force Microscopy (AFM) to study the force interaction between thrombin and DNA aptamer governed by electrostatic modulation. The thiolated aptamer was deposited onto gold substrate located in a liquid cell, and then repeatedly brought into contact with a thrombin-coated AFM tip under 0mV, 100mV and -100mV electrical fields respectively applied by a standard electrochemical cell. Force drop-offs during the pull-off process were measured to determine the unbinding force between the pair with loading rates spanning from 100pN/s to 40000pN/s. A large number of experiments were conducted to obtain statistically significant responses and dissociation forces associated with the last binding event were analyzed to understand the influence of electrical fields on molecular binding. The results from experiment show that the specific binding events of the pair were drastically reduced under the positive electrical fields. Due to the negatively charged nature of DNA aptamer, positive electrical fields can trigger large bending-down conformational transition of the strands, thus can inhibit the bond formation. There is no harmful influence on the molecular binding by negative electrical fields. The autocorrelation function analyses were conducted on all three cases for obtaining the elementary dissociation force, and showed that the specific binding maintain the same scale and nature of the force. The study confirms the idea of electrostatic modulation of the binding interaction between thrombin and DNA aptamer, thus proposes an application potential on biotic-abiotic interface design.

Keywords Atomic force microscopy Dynamic force spectroscopy Thrombin Aptamer Electrostatic actuation

4.2 Introduction

Previous research revealed that electrostatic fields could successfully actuate and modulate the binding behavior between the catalytic enzyme thrombin involved in coagulation and its binding pair DNA aptamer. However, the dynamic response and associated force interaction could not be characterized by those experiments. It should be noticed that explicit measurement and characterization of the binding force between thrombin-aptamer complex and unveiling the underlying kinetics which governs the molecular binding physics could provide in-depth information and insights on the electrostatic actuation based modulation of the conformation and binding behavior of biomolecules, thus may result in an important foundation and reference for biosensor, and biotic-abiotic interface design (Breisch, Gonska et al. 2005; Dudko 2009).

Our previous studies of atomic force microscopy (AFM) based dynamic force spectroscopy of thrombin-aptamer complex has revealed the binding force scale under different loading rates with the open circuit conditions, and implies the potential to investigate the force interaction of thrombin-aptamer complex under electrostatic field conditions using the AFM based DFS technique. A novel electrochemical cell could be designed to mount on the atomic force microscope stage, and then facilitates the implementation of such investigation desire.

The so-called electrochemical atomic force microscopy (ECAFM) technology has been applied in certain fields to study the electrical field influence and modification on the physical and chemical performance of target surface. Boussaad et al. (Boussaad and Tao 1999) utilized electrochemical tapping-mode AFM to study the interaction between myoglobin (Mb) and self-assembled didodecyldimethylammonium bromide (DDAB) mono- and multilayers. They discovered the heme group of the protein undergoes a fast electron-transfer reaction, and the structure of DDAB film has a potential dependence that it is changed from a solidlike phase to liquidlike phase in terms of the increase of potentials from -0.2V to -0.2V, the mechanism of which they accredited to the faster diffusion of Mb through the DDAB layers at the raised potentials. Kueng et al. (Kranz, Kueng et al. 2003; Kueng, Kranz et al. 2003) developed a new technique that combines AFM and scanning electrochemical microscopy (SECM), and enable the simultaneous monitoring and investigation of surface topography and the enzyme activity of bioactive probes under electrostatic field application. Ciorcea et al. (Chiorcea and Brett 2005) utilized ECAFM to investigate the adsorption behavior of guanine on a highly oriented pyrolytic graphite (HOPG) electrode surface with controlled potentials from 0 to 1.3V, and found the application of electrical fields provided better attachment of the guanine on the HOPG suface compared to natural adsorption. Sekine et al. (Sekine, Kaji et al. 2008; Sekine, Kaji et al. 2009) fabricated an AFM probe electrode at the tip by first insulating he probe with Parylene C, and then grounding the apex of the tip to expose the electrode. By in-situ topographical imaging of this ECAFM on the heparin-coated substrate under applied potentials from 0.5V to 1.5V, they observed the detachment of the heparin and the adsorption of fibonectin on the substrate. Hao et al. (Hao, Zhang et al. 2012) applied ECAFM to study the electrochemical behavior of the redox metalloenzyme copper nitrite reductase (CNiR) immobilized on Au(111) surface under controlled potentials from -0.2 V to 0.2 V. They discovered a strong reductive electrocatalytic signal appeared in the presence of nitrite, which indicates the conformational changes in the enzyme upon substrate binding, and thus either enhanced the enzyme/electrode contact, or opened intramolecular electron-transfer channels between the redox center and the catalytic site. The ECAFM applications have also been reported in quite a few fields of studies, such as thin film growth and formation (Kepler and Gewirth 1994; Naoi, Ooike et al. 1994; Vidu and Hara 1999; Peter, Hempenius et al. 2000; Bloess, Staikov et al. 2001; Peter, Hempenius et al. 2001; Schneegans, Moradpour et al. 2004; Geng, Jiao et al. 2006; ElKaoutit, Naggar et al. 2009; Ghorbal, Grisotto et al. 2009; Umeda and Fukui 2010; Domi, Ochida et al. 2012; Domi, Doi et al. 2013), deposition (Koinuma and Uosaki 1995; Semenikhin, Jiang et al. 2000; Tamura, Kondo et al. 2000; Li, Maynor et al. 2001; Li, Ben et al. 2002; Kubo, Hirai et al. 2003; Coughlin and Huang 2005; de Abril, Gundel et al. 2008), dissolution (Koinuma and Uosaki 1996; Macpherson, Unwin et al. 1996; Vidu, Quinlan et al. 2002; Jones, Unwin et al. 2003; Romer, Plaschke et al. 2003; Doi, Inaba et al. 2008; Huitink, Gao et al. 2010), corrosion (Reynaud-Laporte, Vayer et al. 1997; Eick, Kahlen et al. 2000; Pan, Femenia et al. 2000; Bearinger, Orme et al. 2001; Chen and Tsai 2011), phase transition (Lapkowski, Zak et al. 2001), flux generation (Holder, Gardner et al. 2005), and membrane proton conductivity (Hink, Aleksandrova et al. 2010). Besides, the development and improvement on the ECAFM technology itself have been carried on for better simultaneous monitoring of electrical field influence and topography imaging (Lugstein, Bertagnolli et al. 2002; Fasching, Tao et al. 2004; Villarroya, Perez-Murano et al. 2004; Burt, Dobson et al. 2007; Eckhard, Shin et al. 2007; Moon, Wiedemair et al. 2007; Shin, Hesketh et al. 2008).

In this study, we conducted in-situ ECAFM based dynamic force spectroscopy on thrombin and DNA aptamer binding pair subjected to applied electrical potentials to explicate the electrostatic field influence on the binding behavior, and expressed the force interaction between the complementary pair as a function of controlled potentials.

4.3 Methods

Binding forces were measured between the thrombin-coated AFM tip and gold substrate that was functionalized with 5’ thiolated 50nt-thrombin aptamers (HS-GCCTTAACTGTAGTACTGGTGAAATTGCTGCCATTGGTTGGTGTGGTTGG) (Tasset, Kubik et al. 1997). Different electrical field potentials were applied through three electrode system between the working electrode – gold substrate and reference electrode

– silver wire, to investigate the electrostatic influence on force interaction between the binding pair.\

All chemicals required for the experiments were purchased from Sigma Aldrich (www.sigma.com), and all DNA oligonucelotides were purchased from Integrated DNA Technologies (www.idtdna.com). Gold-coated silicon nitride tips were purchased from Novascan Technologies Inc. (www.novascan.com). All solutions were prepared with double distilled water (ddH2O).

Prior to thrombin functionalization, the spring constant of each AFM tip was determined via Sader's method (Sader, Chon et al. 1999). Thrombin was then functionalized on the gold coated AFM tip using the following method: First, the probe was incubated in 2mM mercaptohexadecanoic acid (MHA) for 1 h to form a carboxyl-terminated self-assembled monolayer on the gold surface, then the probe was incubated in freshly prepared 10 mg/ml carbodiimide (EDAC) in ddH$_2$O for 30 min to activate the carboxylic acid groups for protein attachment. The probe was then immersed in 10 μM human thrombin in buffered saline solution (137 mM NaCl, 2.7 mM KCl, 10 mM Na$_2$HPO$_4$, 5 mM KH$_2$PO$_4$ in ddH$_2$O at pH 7.4 as adjusted with HCl) for 90 min to immobilize the protein on the activated carboxylic acid-terminated SAM surface. Finally, the probe was washed 3 times for 5 min each in buffered saline solution and 3 times for 5 min each in ddH$_2$O. The probe was either used immediately or stored for less than 24 h in ddH$_2$O before the experiments. A single AFM tip was used to collect at the most 300 force curves and a total of 40 different AFM tips were used for the experiments.

A template transfer technique was used to form a smooth gold film on polished silicon wafers. The aptamer-functionalized surfaces were prepared by immersion of gold coated silicon wafers in 3.4 μM thiolated aptamer in binding buffer (20 mM Tris-HCl, 140 mM NaCl, 5 mM KCl, 1 mM $CaCl_2$, 5 mM $MgCl_2$, and 5% glycerol v/v in ddH_2O at pH 7.4) (Basnar, Elnathan et al. 2006) for 1 min. The functionalized surfaces were rinsed several times with ddH_2O and grounded with copper tape before being used for the unbinding experiments.

Force curve experiments for coated substrates were performed in binding buffer using a Dimension 3100 atomic force microscope with a designed electrochemical cell, as shown in Fig. 4-1. During the experiments, the AFM tip was moved towards the sample to establish contact with surface and then retracted back to its starting location at a fixed displacement rate. Three electrical fields strength of -100mV, 0mV, 100mV were applied onto the sample surface respectively via regular three electrode system. Open circuit force curve experiments were also conducted for comparison. The sample serves as the working electrode, while a silver wire is used as a reference electrode and platinum wire as a counter electrode to maintain the constant potential value. The force applied to the AFM tip during surface contact and retraction was measured to obtain the force curves. Loading rate dependence of the force interaction associated with each controlled potential was also considered by taking two different nominal displacement rates (200 nm/s and 2000 nm/s) of the AFM step motor. A total of two thousand force curves (20 samples × 10 locations/samples × 10 force curve/locations) were acquired for each displacement rate.

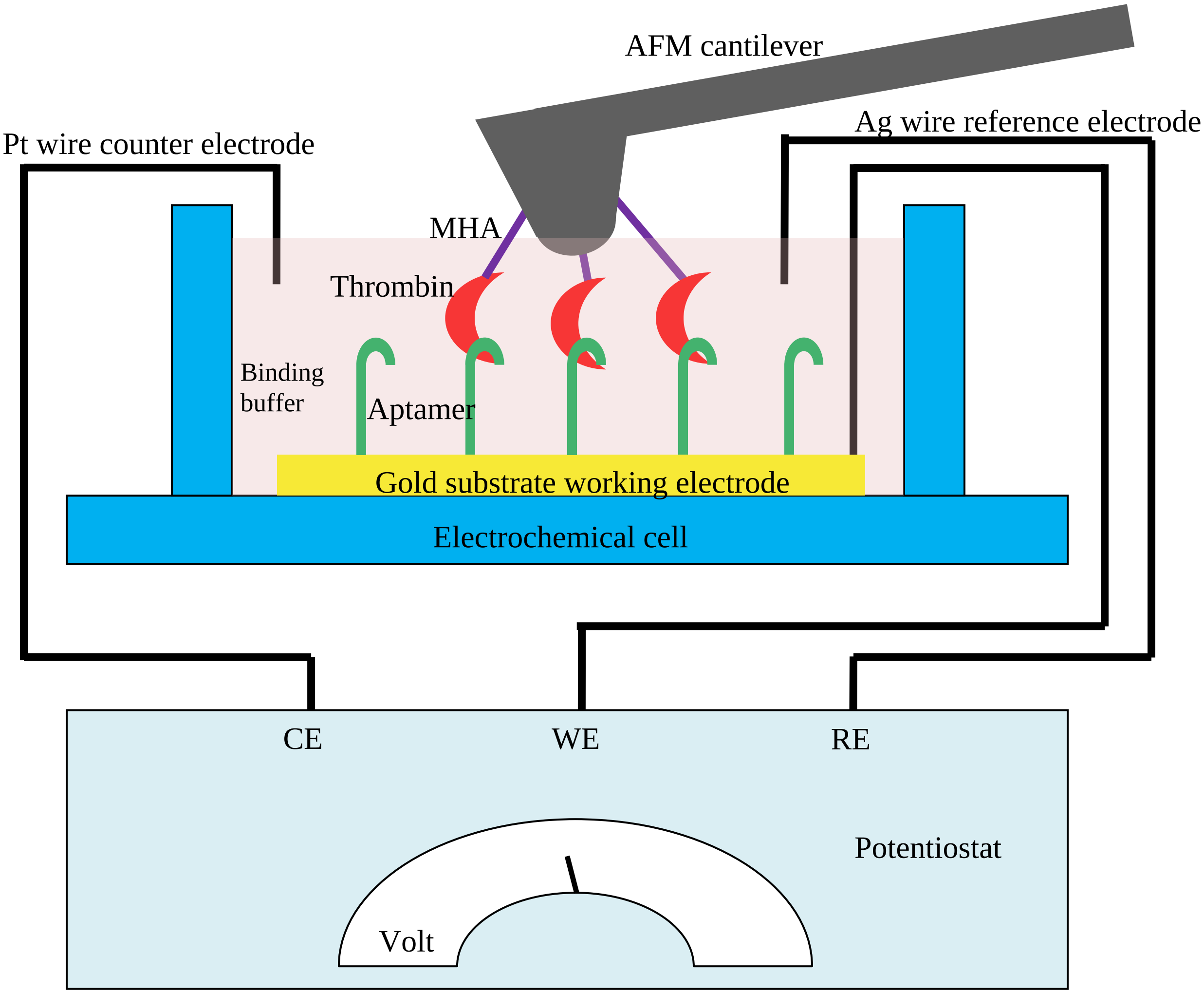

Fig. 4-1 ECAFM setup

4.4 Results and discussion

The representative force curves of multiple unbinding events corresponding to interactions between thrombin coated AFM tip and aptamer functionalized surfaces under open circuit, -100 mV, 0 mV, and 100mV are shown in Fig. 4-2.

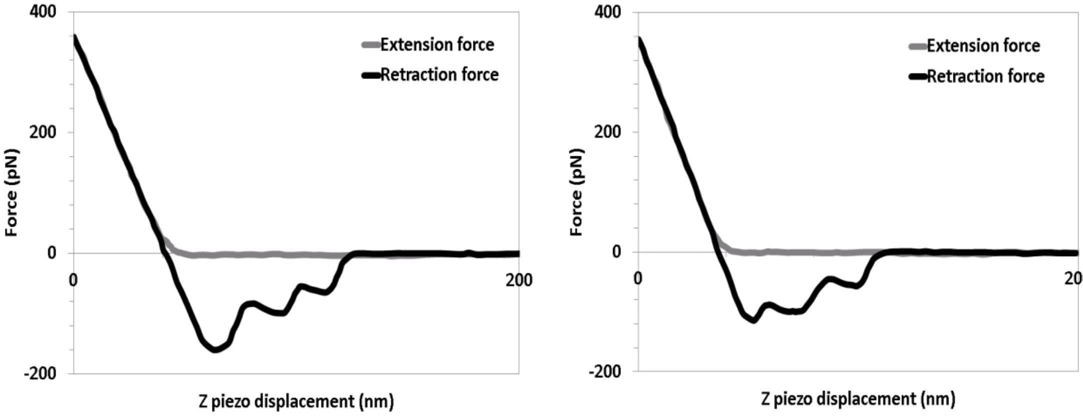

(a) Open circuit (b) -100mV

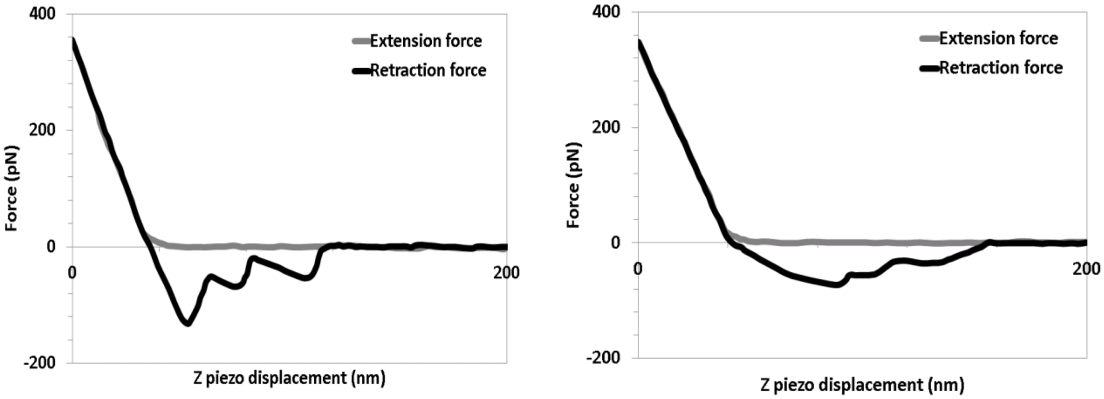

(c) 0mV (d) 100mV

Fig. 4-2 Representative force curves under electrical fields

It can be seen that for 0mV and -100mV, force curves showed similar trend and magnitude as open circuit condition. While for 100mV, the magnitude of the last rupture force decreased, and the slope of the retraction curve had an abrupt change after the pull-up phase and the whole displacement tends to be elongated, which implies the substantial influence of electrostatic field application on the dissociation process. The percentage of force curves out of all attempts corresponding to no interaction, single unbinding and multiple unbinding of all four situations are summarized in the Table 4-1. It indicated that for open circuit, -100mV and 0mV, the multiple unbinding rates could always be held at around 10%, which coincided with Pope. el al.'s studies on force-induced melting of 12mer double strand DNA (Pope, Davies et al. 2001). However, for 100mV, it implies that the electrostatic field can reduce the multiple unbinding rate to one third level of the above cases. In other words, we can summarize that the positive electrical field application can decrease both the binding strength and numbers of the thrombin-aptamer complex.

Table 4-1 Summary of force curves under electrical fields

	No interaction	Single unbinding	Multiple unbinding
Open circuit	14.9%	73.9%	11.2%
-100mV	31.4%	59.5%	10.6%
0mV	23.2%	66.3%	9.15%
100mV	56.0%	40.7%	3.35%

The rupture force of the last step of multiple unbinding events was analyzed since it mostly likely approaches single bond dissociation, and the slope before the last step was calculated to acquire the real loading rate. After collecting both of the last rupture forces and loading rates, and categorizing the loading rates into four levels, we can generate histograms of the measured dissociation force distribution at different loading rate levels – lowest (100 ± 40 pN/s), lower median (700 ± 300 pN/s), higher median (6000 ± 2000 pN/s and highest (45000 ± 15000 pN/s) , and different potential levels – -100mV, 0mV, and 100mV), as shown in Fig. 4-3 and Fig. 4-4 respectively (The detailed distributions for each loading rate level under different potential conditions could be seen in the appendix). As loading rates increased, the range of the dissociation forces were expanded and the peaks in the histograms, which identify the most frequent force magnitudes, shifted towards higher magnitudes for different potential conditions. It should be noticed clarified that the counts of rupture force shown in histogram for positive potential force measurement were much lower than that of open circuit, zero and negative potential situations, which is just resulted from the significant decrease of unbinding events, as exhibited in Table 4-1.

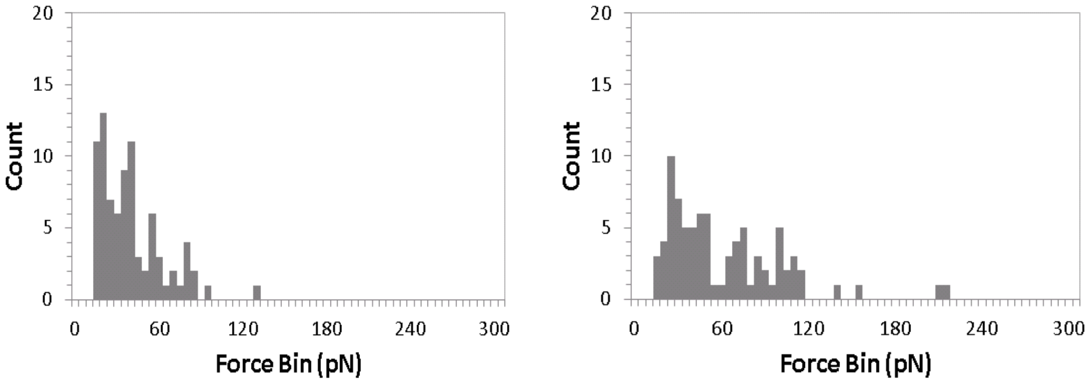

(a) Lowest loading rate (130pN/s) (b) Lower median loading rate (890pN/s)

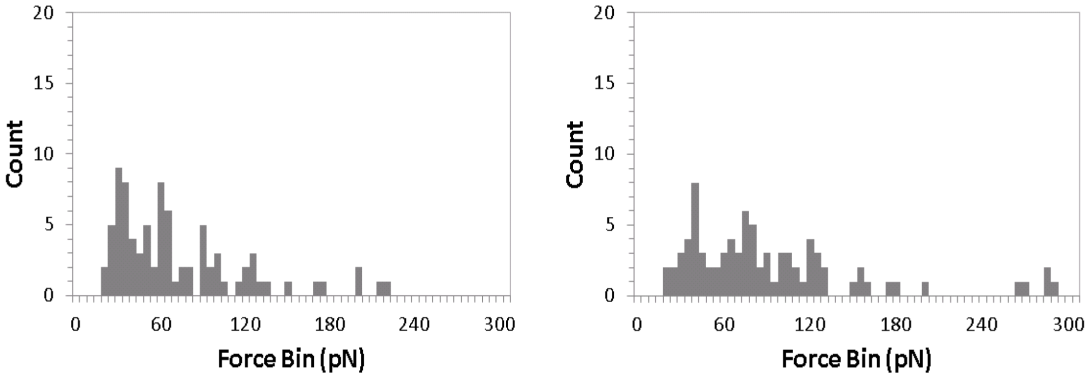

(c) Higher median loading rate (8000pN/s) (d) Highest loading rate (49000pN/s)

Fig. 4-3 Rupture force distribution of thrombin-aptamer complex for different loading rate levels under -100mV

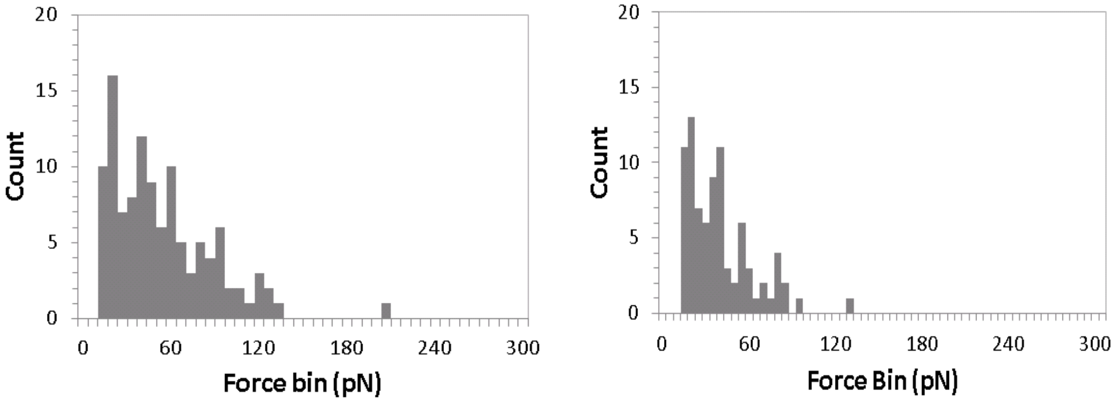

(a) Open circuit (b) -100mV

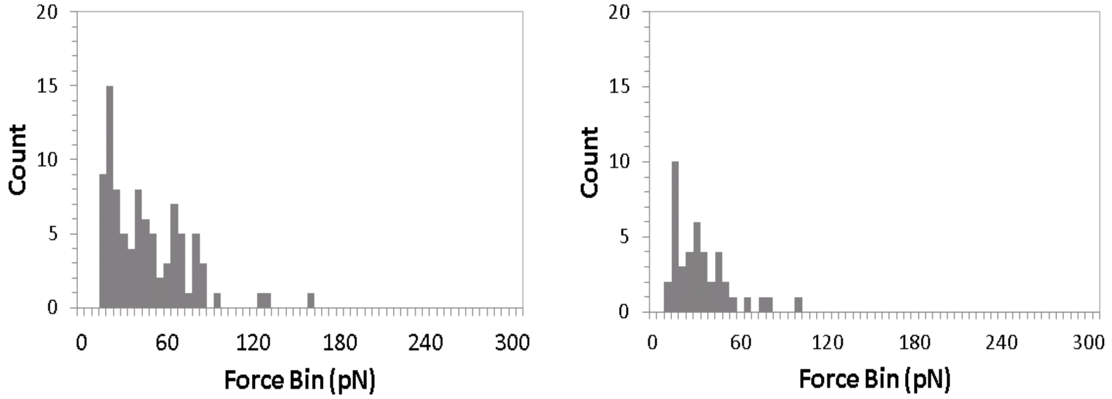

(c) 0mV (D) 100mV

Fig. 4-4 Rupture force distribution of the thrombin-aptamer complex for different potentials under lowest loading rate level

For the thrombin-aptamer complex, the distribution of rupture forces shows periodic peaks in the histogram, which may indicate the existence of an elementary binding force corresponding to dissociation of a single protein-aptamer complex. Auto correlation function (ACF) then could be applied on force distributions for estimating the magnitude of the elementary binding force as a function of the loading rates under different controlled potentials (Kado and Kimura 2003), as shown in Fig. 4-5 (The detailed ACF plot for each loading rate level under different potential conditions could be seen in the appendix). Periodically spaced peaks in auto correlation function plots confirm the existence of the elementary binding force i.e. the force quantum for each potential condition. The period of the repeating peaks in the autocorrelation plots was measured to estimate the force quantum, and the computed force quanta as a function of loading rates for all potential conditions are shown in Table 4-2.

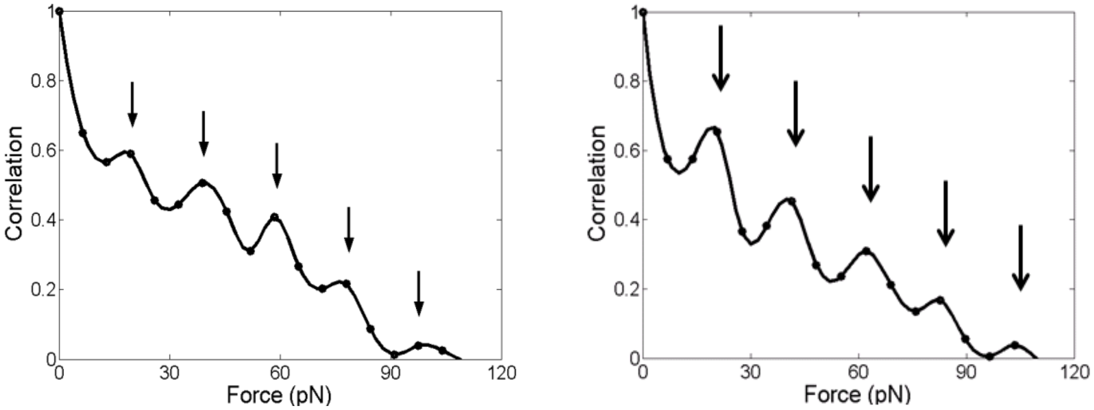

(a) Open circuit (b) -100mV

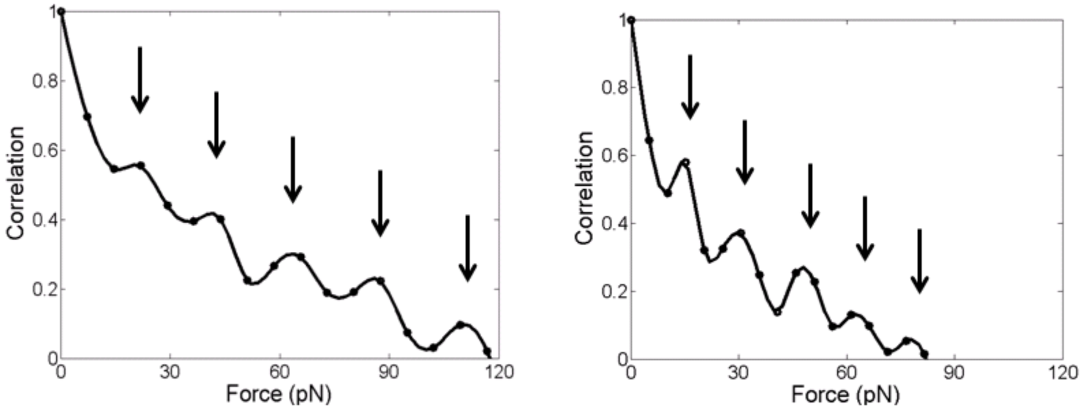

(c) 0mV (D) 100mV

Fig. 4-5 Autocorrelation function of rupture force distribution for different potentials under lowest loading rate level

Table 4-2 Force quantum corresponding to different potential conditions

	Lowest loading rate	Lower median loading rate	Higher median loading rate	Highest loading rate
Open circuit	20	26	33	40
-100mV	21	27	34	40
0mV	21	26	33	39

100mV	16	22	27	33

It can be seen that the positive electrical fields decreased the force interaction between the thrombin and aptamer, while the zero and negative electrical fields didn't show significant influence on the binding strength of the complex compared to open circuit situation. Those phenomena could be caused by the electrostatic pulling down force that generated by positive electrical field on the negatively charged DNA aptamer, which weaken the binding between the complex and thus attenuate the force interaction. While under negative electrical fields, the pushing up force exerted by negative potential on the negatively charged DNA aptamer does not influence the conformation states of the aptamer significantly, thus the binding and force interaction between the complex are not changed. Based on those force quanta and loading rates, the dynamic force spectrum under for different potential conditions can be shown in Fig. 4-6.

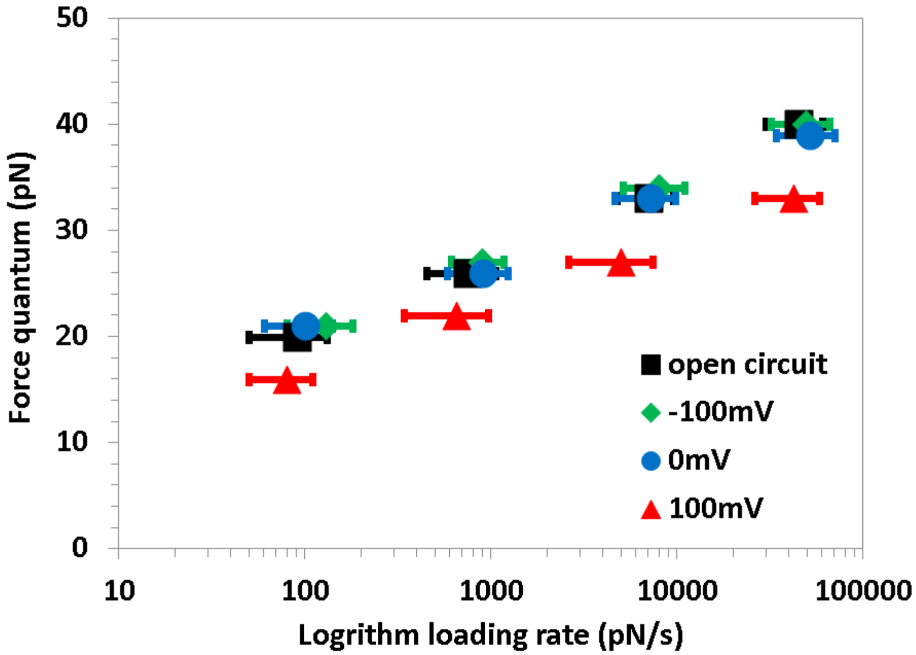

Fig. 4-6 Force spectrum under different electrical field conditions

The dissociation process of thrombin-aptamer complex with applied load may be modeled via a single energy barrier model as proposed by Evans and co-workers (Moy, Florin et al. 1994; Evans 1998; Evans 1999; Merkel, Nassoy et al. 1999; Evans 2001; Evans, Leung et al. 2001). When a bound complex is not subjected to external loads, the energy barrier to be overcome during the dissociation process is very high, and thus results in a low probability for the complex to dissociate. When the bound complex is pulled apart under applied loads, the work done by loads could decrease the height of the energy barrier, and consequently increases the probability of dissociation. The probability of dissociation p, can be expressed as a function of applied force F as (Evans 1998; Evans 1999; Merkel, Nassoy et al. 1999; Evans 2001; Evans, Leung et al. 2001)

$$p(F) = \frac{F_b}{r_f t_{off}} \exp\left\{ \frac{F}{F_b} - \frac{F_b}{r_f t_{off}} \left[\exp\left(\frac{F}{F_b} \right) - 1 \right] \right\}; \text{where } F_b = \frac{k_B T}{x_b} \tag{4-1}$$

In the equation, F_β is the thermal force that dominates the spread of the distribution; r_f is the loading rate; t_{off} is the spontaneous dissociation time; and x_β is the width of the transition state barrier. According to equation (4-1), a peak in the probability distribution appears as the exponential increase in failure rate due to applied force crosses over to the precipitous decline in bond survival with increasing force (Evans 2001). The rupture force F_{peak}, corresponding to the peak of the probability density distribution as a function of loading rate is then determined to be:

$$F_{peak} = F_\beta \ln\left(\frac{r_f t_{off}}{F_\beta} \right) \tag{4-2}$$

According to equation (4-2), the F_{peak}, i.e. the force quantum has a linear dependence on logarithm of loading rate, which has a good agreement with the trend shown in Fig. 4-6. Thus single energy barrier model described in equations (4-1) and (4-2) may be used to describe the thrombin-aptamer interaction. The slope and x-intercept of the fitted data for each potential condition were used to two important kinetic parameters, the width of transition state barrier xβ, and spontaneous dissociation time toff, as shown in Table 4-3.

Table 4-3 Kinetic parameter estimation for each potential condition

	xβ (nm)	toff (s)
Open circuit	0.81	720
-100mV	0.82	690
0mV	0.83	740
100mV	0.85	120

From Fig.4-6, since the slopes of data trend for each potential condition are all similar, thus the values of transition state barrier x_β are comparable. Meanwhile, the data trend of positive potential condition has a significantly larger x-intercept then the other three conditions, thus results in a much lower spontaneous dissociation time t_{off}, which could be the kinetic explanation of the binding-weaken effect due to the application of positive electrical fields on the thrombin-aptamer complex.

4.5 Conclusion

1) Through ECAFM technique, in-situ measurement of force interaction between thrombin-aptamer binding pair can be successfully acquired.

2) Moderate electrical fields can be utilized to weaken or keep the binding between thrombin and aptamer complex,

2a) Positive electrical fields of 100 mV can decrease the force interaction between the thrombin and aptamer, and lower the number of binding significantly;

2b) Zero and negative (-100mV) electrical fields can maintain the similar force interaction and number of binding between the thrombin and aptamer as the open circuit DFS experiment.

3) Single energy barrier model may be used to illuminate the dissociation process of thrombin-aptamer binding, and estimated kinetic parameters from fitting the model to experimental data suggest that the significant drop of spontaneous dissociation time is the root cause of the bond-weaken effect under positive electrostatic field application.

4.6 Appendix

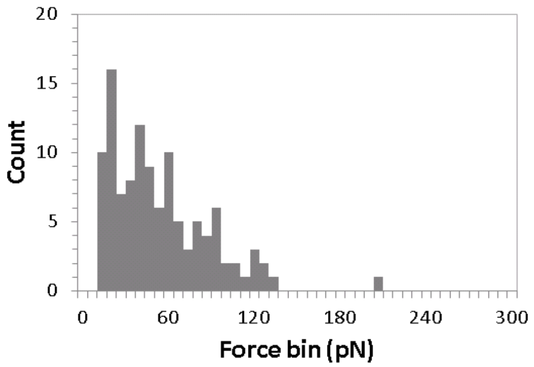

(a) Lowest loading rate (90pN/s)

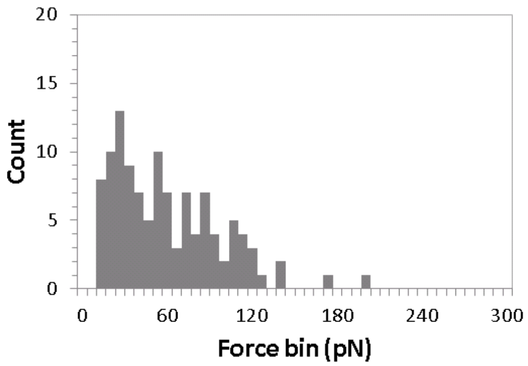

(b) Lower median loading rate (750pN/s)

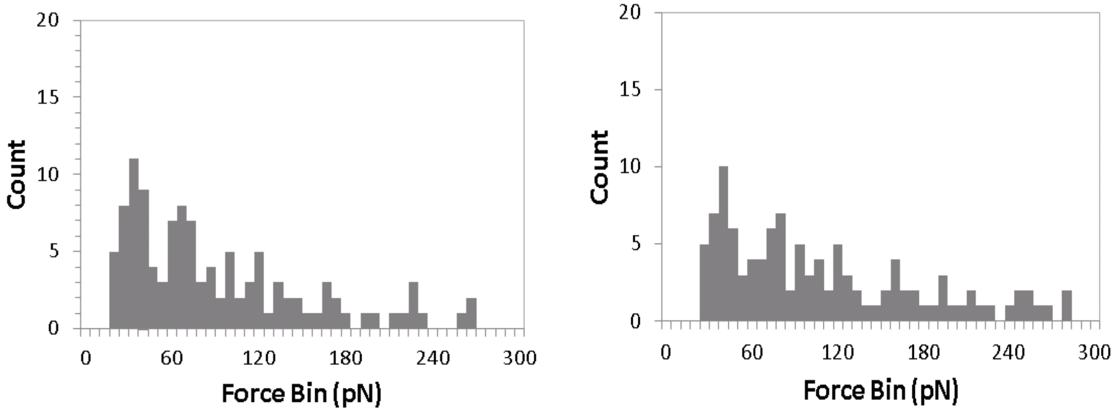

(c) Higher median loading rate (7000pN/s) (d) Highest loading rate (45000pN/s)

Appendix Fig. 4-1 Rupture force distribution of thrombin-aptamer pair for different loading rates under open circuit

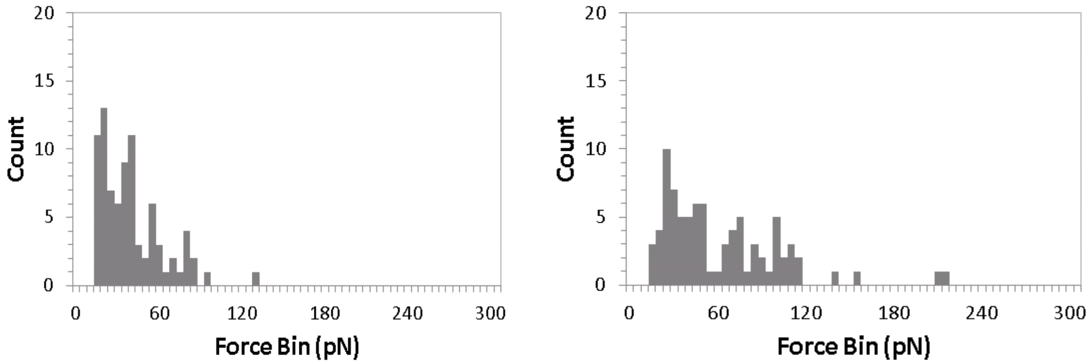

(a) Lowest loading rate (130pN/s) (b) Lower median loading rate (890pN/s)

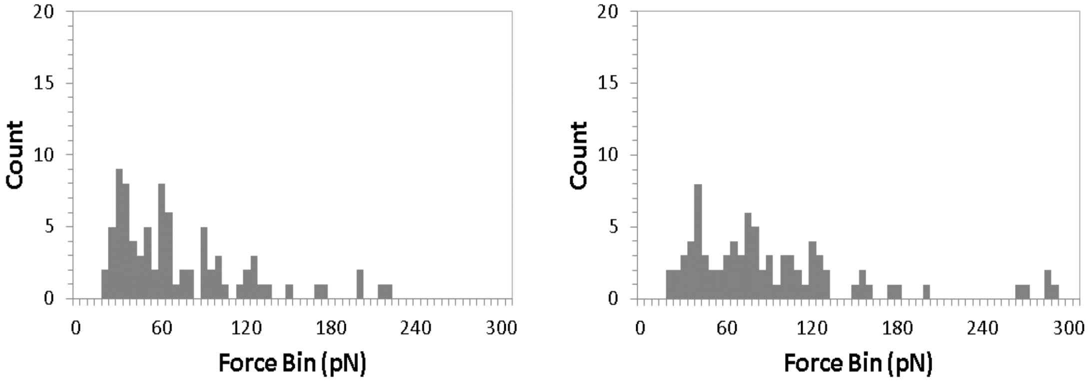

(c) Higher median loading rate (8000pN/s) (d) Highest loading rate (49000pN/s)

Appendix Fig. 4-2 Rupture force distribution of thrombin-aptamer pair for different loading rates under -100mV

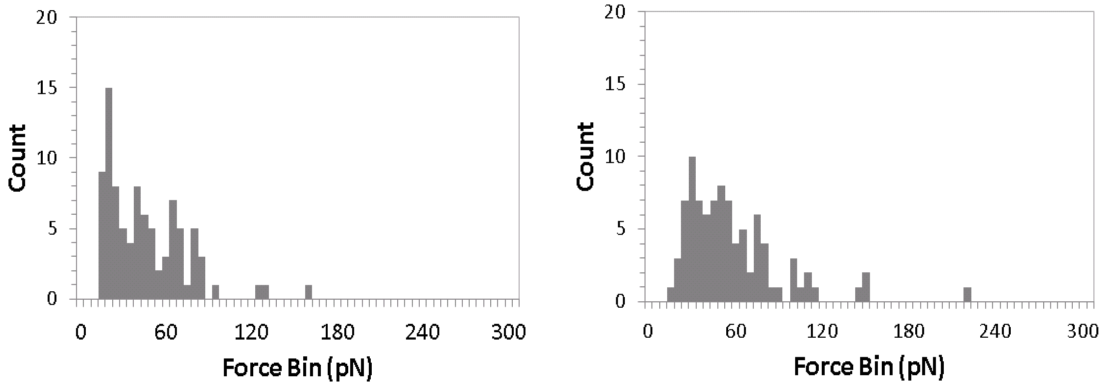

(a) Lowest loading rate (100pN/s) (b) Lower median loading rate (900pN/s)

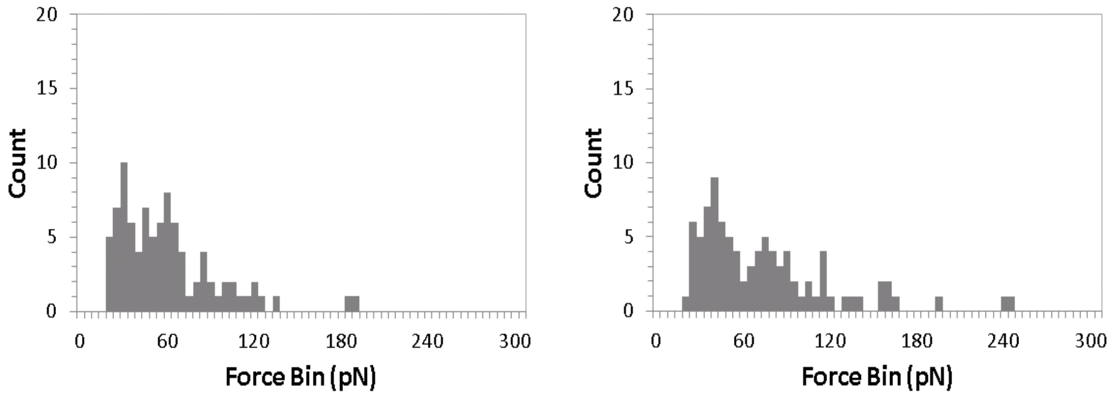

(c) Higher median loading rate (7200pN/s) (d) Highest loading rate (52000pN/s)

Appendix Fig. 4-3 Rupture force distribution of thrombin-aptamer pair for different loading rates under 0mV

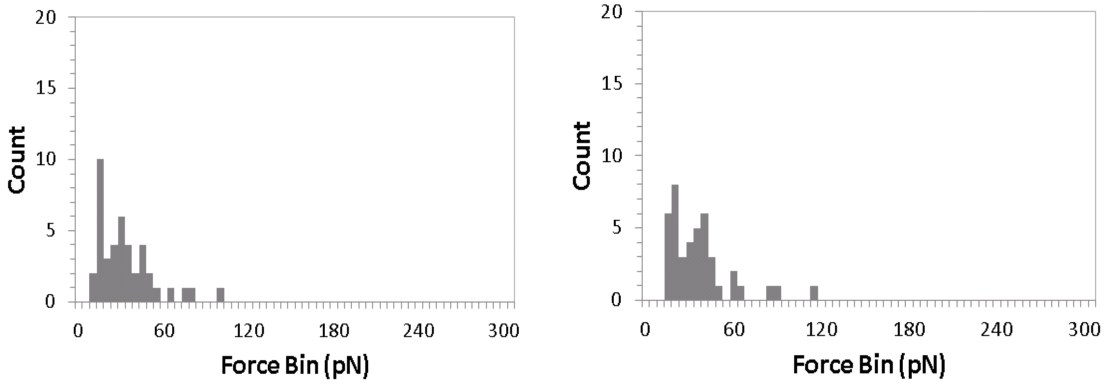

(a) Lowest loading rate (80pN/s) (b) Lower median loading rate (650pN/s)

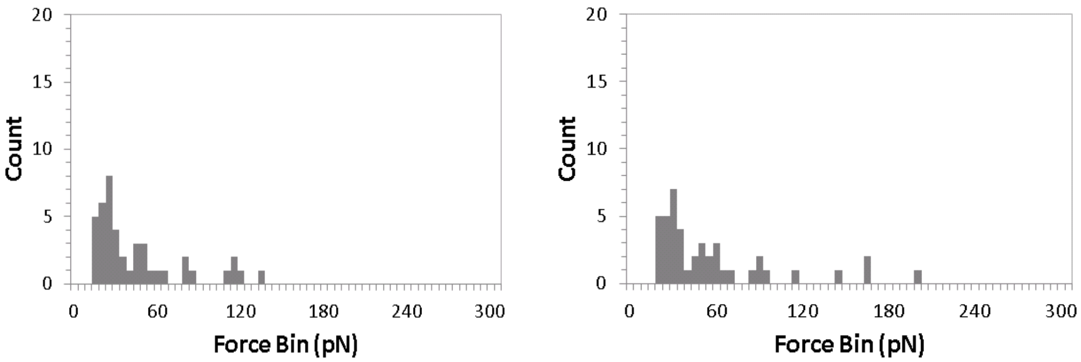

(c) Higher median loading rate (5000pN/s) (d) Highest loading rate (42000pN/s)

Appendix Fig. 4-4 Rupture force distribution of thrombin-aptamer pair for different loading rates under 100mV

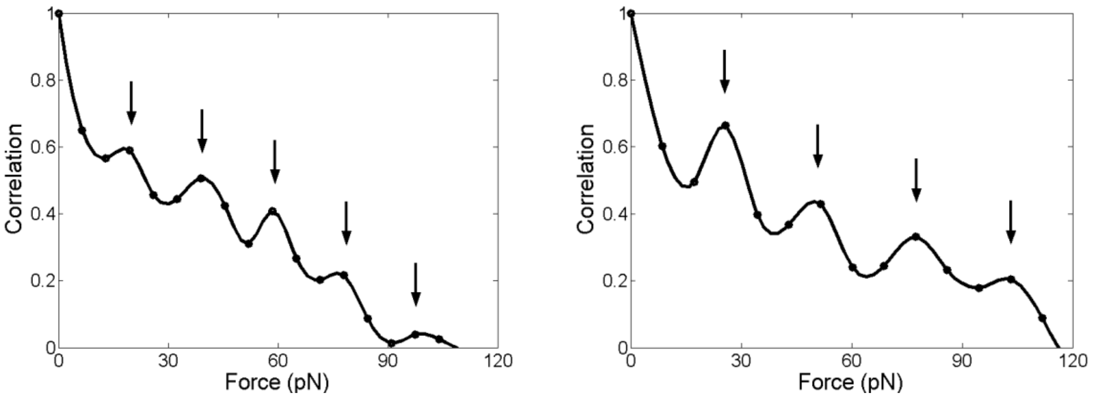

(a) Lowest loading rate (90pN/s) (b) Lower median loading rate (750pN/s)

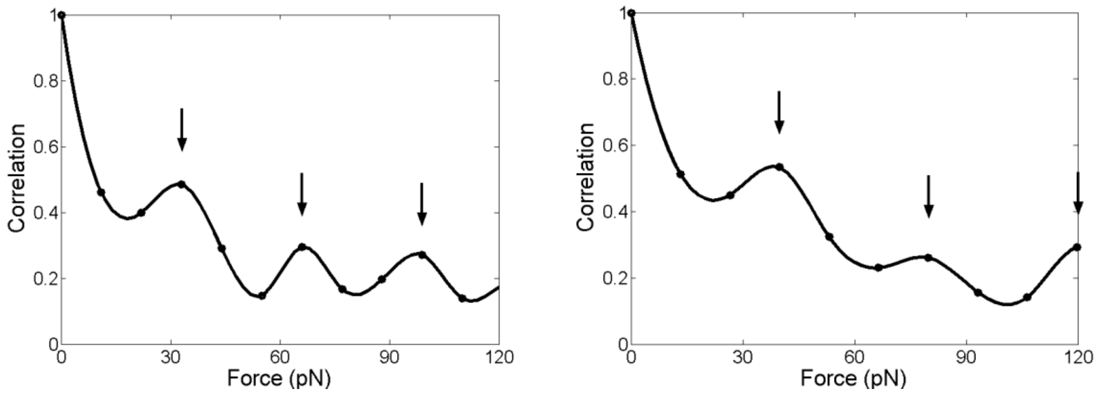

(c) Higher median loading rate (7000pN/s) (d) Highest loading rate (45000pN/s)

Appendix Fig. 4-5 Autocorrelation function of last rupture force distribution for all loading rates under open circuit

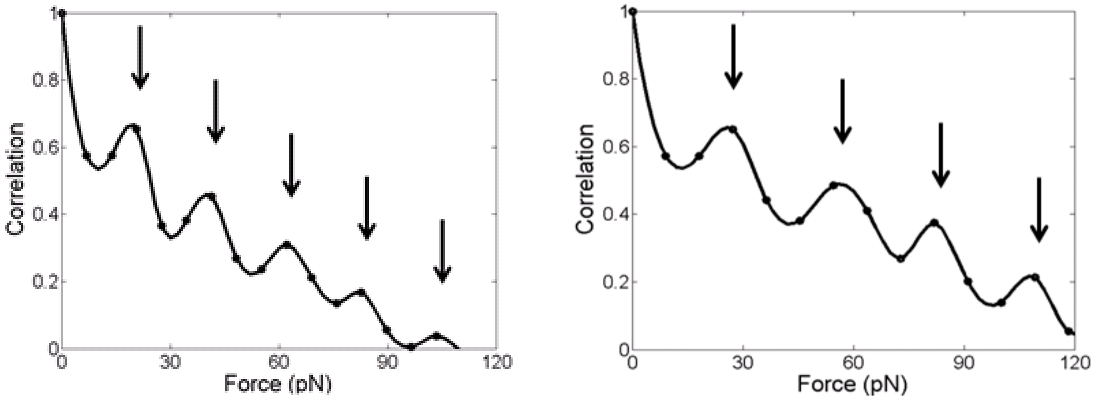

(a) Lowest loading rate (130pN/s) (b) Lower median loading rate (890pN/s)

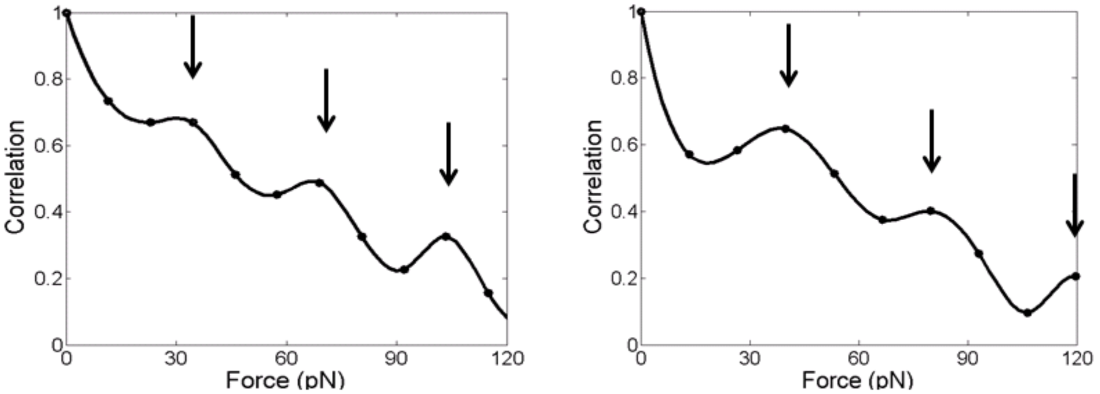

(c) Higher median loading rate (8000pN/s) (d) Highest loading rate (49000pN/s)

Appendix Fig. 4-6 Autocorrelation function of last rupture force distribution for all loading rates under -100mV

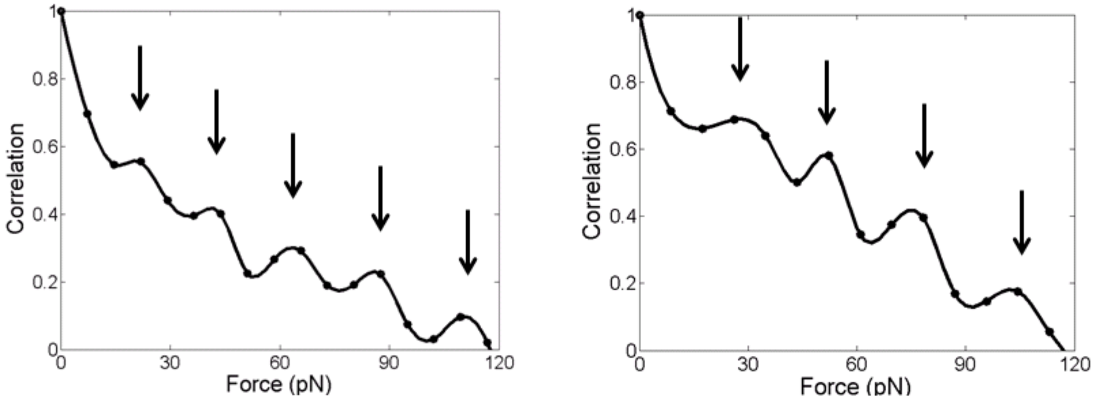

(a) Lowest loading rate (100pN/s) (b) Lower median loading rate (900pN/s)

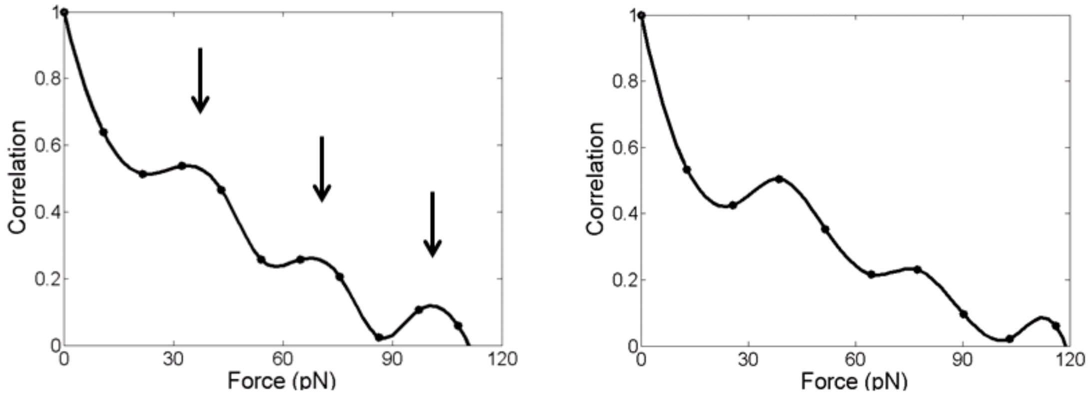

(c) Higher median loading rate (7200pN/s) (d) Highest loading rate (52000pN/s)

Appendix Fig. 4-7 Autocorrelation function of last rupture force distribution for all loading rates under 0mV

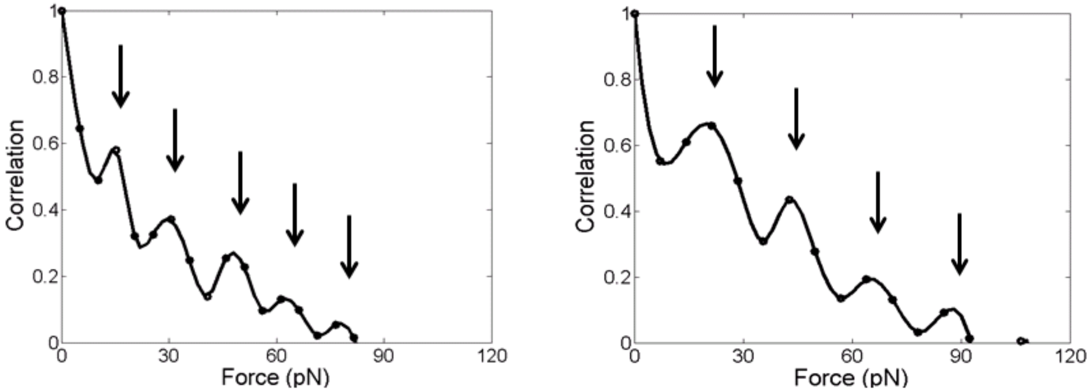

(a) Lowest loading rate (80pN/s) (b) Lower median loading rate (650pN/s)

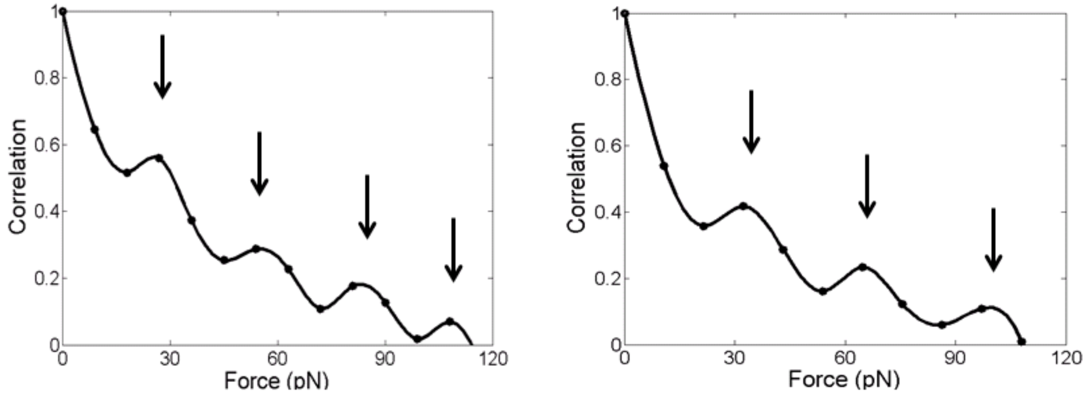

(c) Higher median loading rate (5000pN/s) (d) Highest loading rate (42000pN/s)

Appendix Fig. 4-8 Autocorrelation function of last rupture force distribution for all loading rates under 0mV

CHAPTER 5. MOLECULAR DYNAMICS SIMULATION OF ELECTRICAL FIELD INDUCED CONFORMATIONAL TRANSITION AND ASSOCIATED FRICTIONAL PERFORMANCE OF MHA MONOMOLECULAR FILMS

(A paper published on Journal of Physics D: Applied Physics, Aug. 2012)

Xiao Ma, and Pranav Shrotriya

Department of Mechanical Engineering, Iowa State University, Ames, IA50010, USA

5.1 Abstract

Sparse monomolecular film assemblies with polar end groups such as carboxyl have attracted considerable interest because of their ability to undergo conformational transition under electrical fields. We report the results from molecular dynamics simulation of electrical field induced conformational transitions and associated frictional performance of carboxyl-terminated monomolecular films. Simulation results indicate that the density of the monomolecular film has a significant influence on the conformational transition under electrical fields. In the case of loose-packed monomolecular films, carboxyl-terminated chains cluster together to form disordered film due to large interchain separation. Under the application of positive electrical field, the chain backbone rotates and lies down on the substrate forming disordered clusters, whereas under the application of negative electrical fields, the chains stand up and cluster together to form disordered clusters. Under shallow indentation with purely repulsive

indenter, loose-packed monomolecular films subjected to positive electrical field exhibit lower level of frictional response compared with films subjected to negative and no electrical fields. In the case of close-packed monomolecular films, the molecular chains assemble in an ordered film and the space is not enough for backbone chains to generate large-scale conformational transition. Due to this spatial limitation, the applied electrical field was not found to have any influence on the backbone chain rotation and associated frictional response under shallow indentations with purely repulsive indenter.

Keywords Molecular dynamics simulation Self-assembled Monolayer MHA Electrical field Conformational transition Friction

5.2 Introduction

Self-assembled monolayers (SAMs) have attracted increasing interest as an active smart surface coating for applications in Micro/Nano tribology, microfluidics, lubrication and several biomedical fields. These monomolecular assemblies can undergo conformational transition through application of external stimuli, such as temperature, pH of solvent, application of electrical fields, and light or electro-chemical surface modifications. Among different external stimuli, applying external electrical fields is practically feasible and effectively controllable method without any detrimental influence on the chemical stability of SAMs (Lahann, Mitragotri et al. 2003; Karuppiah, Zhou et al. 2009).

Lahann et al. (Lahann, Mitragotri et al. 2003) demonstrated electrical field induced conformational transition of sparse carboxyl-terminated SAMs. Due to the polar nature of the carboxyl group, it was hypothesized that the application of negative electrical field pulled the chains straight, and positive field bent the chains down upon the substrate. The conformational transition of the chain was deduced from the change of surface from hydrophilic to hydrophobic state under the application of an electrical field.

Kanaga Karuppiah et al. (Karuppiah, Zhou et al. 2009) used an atomic force microscope (AFM) to evaluate the work of adhesion and frictional response of low-density mercaptocarboxylic acid SAM under electrical fields with different polarities. They discovered higher work of adhesion when negative bias electrical fields were applied to the SAM. Contact sliding experiments showed that a higher friction level was obtained when positive bias electrical fields were applied in comparison with neutral and negative electrical fields. They attributed the contrary observation between work of adhesion and friction to crystalline order of sparse monolayer films, i.e. the higher friction under positive bias is attributed to the relatively disordered structure of the film, whereas the relatively ordered structure under negative bias may cause the friction to decrease. These experimental results indicate that the application of an electrical field modifies the surface properties of sparse monolayer films and the observed phenomena are attributed to the conformational changes in the films (Lahann, Mitragotri et al. 2003; Karuppiah, Zhou et al. 2009). It is, therefore, important to investigate the conformational changes and structure of sparse monomolecular films under electrical fields.

All-atom molecular dynamics (MD) simulation can serve as tool to identify the influence of electrical field and chain density on conformational transitions and film structure but have not been applied to carboxyl-terminated SAM films. Vemparala et al. (Vemparala, Kalia et al. 2004) conducted MD simulation to investigate the electrical field induced conformational transition of fully packed polyethylene glycol (PEG) SAMs. Due to the polar nature of glycol groups, the electrical field triggered the conformational transition from an ‘all-trans’ state to ‘gauche’ state in the end groups. However, due to the limited spatial availability in the fully packed SAM, the overall order and backbone chain orientation remained undisturbed during electrical field application.

Several research groups have applied MD simulation to study the structural transition and its influence on the frictional behaviour of SAMs. Harrison et al. (Brenner, Harrison et al. 1991; Harrison, White et al. 1995; Harrison 2001; Harrison, Schall et al. 2008) introduced the AIREBO potential to simulate structural and tribological properties of alkane SAMs using various materials such as carbon nanotubes, diamond surfaces, amorphous carbon surfaces and fullerenes as the indentation and sliding counterfaces. They compared odd number carbon (C13) with even number carbon (C14) systems that differ in the orientation of the last carbon–carbon bond. An analysis of the probability distribution of methyl angle showed that the odd system has comparatively larger extent of deformation, and greater likelihood of gauche defects than the even system. Detailed sliding-direction force distribution suggested that the odd system contains greater fraction of atoms that are capable of generating small pushing and resisting forces, while the even system prevails in enduring large pushing and resisting forces. They also reported that flexible hydrocarbon SAMs can significantly reduce the mechanical excitation in the form of vibrational and rotational energy of the interface lattice layers upon sliding, thus effectively lowering the frictional resistance. Mikulski et al. (Mikulski and Harrison 2001) examined the periodicities associated with the sliding process between hydrocarbon SAM and diamond counterface. They explained the periodicities as result of commensurate contact between the SAM and the corresponding structure on the diamond counterface that can synchronize the motion of chains during the sliding process, thus friction forces also exhibit periodicities in accordance with structural periodicities. White et al. (Harrison, White et al. 1992) explored the directional dependence of friction coefficient on the sliding between two diamond (1 1) hydrogen-terminated SAMs in different crystallographic directions. They found the friction coefficient increases with increasing applied normal load and decreasing temperature for certain crystallographic sliding directions, whereas it is approximately independent of the sliding velocity. Chandross et al. (Chandross, Webb et al. 2004; Chandross, Lorenz et al. 2005) used MD to study the adhesion and friction between ordered and disordered SAMs on silicon dioxide substrate. They introduced the disorder into SAMs by removing randomly selected chains from the originally well-ordered crystalline substrate to generate defects and attaching chains onto an amorphous substrate. By applying relatively slow shear velocities and constant pressures onto SAMs, typical stick-slip motion was observed in full coverage ordered SAMs and disappeared in disordered ones. Compared with the full coverage ordered SAMs, the friction coefficient of the disordered SAMs was found to be not sensitive to the coverage density, chain length and substrate.

Experimental reports indicate that polar end groups such as carboxyl can generate conformational transition by application of electrical fields due to the non-concentric charge distribution of the polar groups. Simulation results show that the orientation of bonds in functional groups and crystallographic directions influence friction responses to large extent for dense and ordered SAMs, and characteristic phenomena such as stick-slip motion and periodicities of friction were observed. For sparse and disordered SAMs, the coverage density and chain length were found not to influence the frictional performance. In this paper, MD simulations are conducted to investigate the conformational transition and changes in film structure induced due to the application of external electrical fields on SAMs of carboxyl-terminated alkanethiol chains. Frictional performance of the SAM is investigated as function of the applied electrical field, film density, normal load and indenter shape.

5.3 Method

5.3.1 Initial Ensemble and Interatomic potentials

All-atom MD simulations were conducted using an open source shared parallel code - LAMMPS (http://lammps.sandia.gov/) to investigate the conformational transitions and frictional performance of carboxyl-terminated alkanethiol monomolecular assemblies under applied electrical fields (Luedtkea 1992; Bhushan, Israelachvili et al. 1995; Plimpton 1995). In order to generate the initial ensemble, 576 molecules of carboxyl-terminated alkanethiol - mercaptohexadecanoic acid ((S-(CH2)15-COOH) (MHA) - chains were arranged in the ($\sqrt{3} \times \sqrt{3}$) R30 ° lattice structure at an approximate 30 ° initial tilt angle with respect to the normal vector on the Au(1 1 1) plane (Zhang, Goddard et al. 2002; Zhang and Jiang 2002). The initial chain orientation and arrangement was chosen to mimic the tilt angles and film structures reported for similar SAM systems (Zhang, Goddard et al. 2002; Zhang and Jiang 2002). At full coverage density, the alkanethiol SAMs formed a hexagonal close-packed $(\sqrt{3} \times \sqrt{3})$ R30° lattice structure on the Au(1 1 1) surface with an interchain spacing of 5 Å.

The molecules were arranged in two different interchain spacings of 5 Å (full coverage) and 10 (sparse coverage). In order to provide spatial room for the backbone chains to undergo conformational transitions the interchain spacing of 10 was chosen for sparse coverage ensemble such that the conformational transitions are influenced by interchain interactions. At even smaller coverage densities, the chains were either nonuniformly distributed or had minimal interactions between neighboring chains. The simulation box, boundary conditions and electrical field orientation for loose-packed SAMs are shown schematically in Fig. 5-1. For close-packed SAMs, the boundary condition and electrical field orientation are similar, but the scale length of the simulation box was reduced to half (the length of *X*-axis was reduced to 207 Å, the length of *Y*-axis was reduced to 60 Å and the interchain spacing was reduced to 5 Å). The simulation box was periodic along in-plane directions and the electrical field was applied along the out-of-plane direction with positive field along the positive axis.

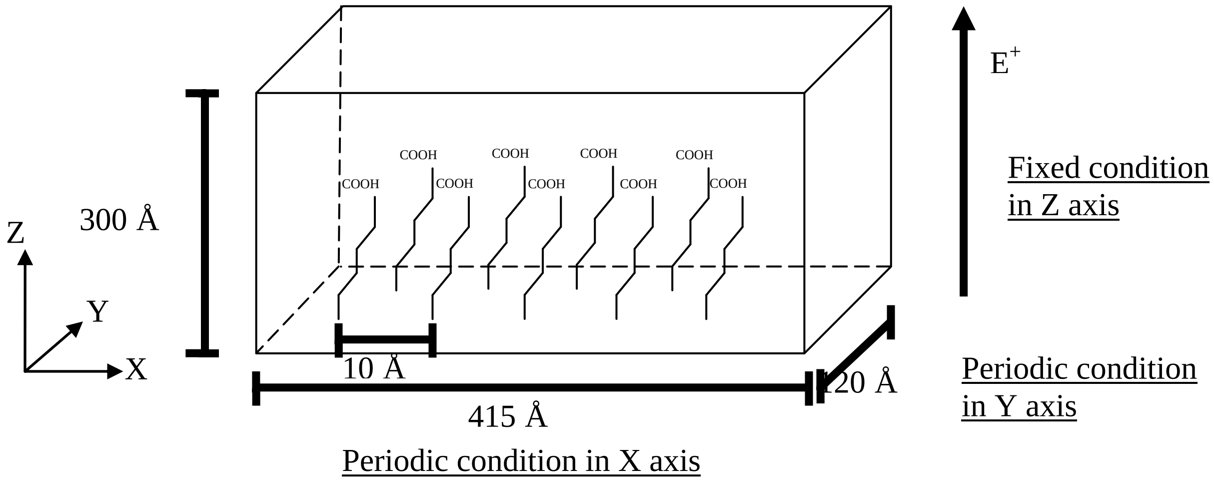

Fig. 5-1 Schematic representation of the simulation box for loose-packed SAMs, periodic along the x and y directions and fixed along the z direction

The interatomic potentials of the simulated system can be divided into three parts: bonded, nonbonded and external electrical field terms as shown in the equation below.

$$\begin{gathered} V = V_{Bonded} + V_{Nonbonded} + V_{Electrical\ Field} = \\ (V_{Bond} + V_{Angle} + V_{Dihedral}) + (V_{Lennard\ Jones} + V_{Coulombic} + V_{Morse}) + V_{ElectricalField} \end{gathered} \tag{5-1}$$

The covalent bonds in the MHA chains were simulated using appropriate CHARMM molecular potentials (Brooks and Karplus 1983; Smith, Jaffe et al. 1993). The bond between sulfur and substrate gold atoms was simulated using the Morse potential in order to accurately simulate the experimentally observed (√3 × √3) R30° superlattice structure and chain orientations (Pertsin and Grunze 1994; Zhang, Goddard et al. 2002). Lennard-Jones (LJ) potential was used to simulate interactions among atoms other than bonded and Morse potential interactions (Sorensen, Liau et al. 1988; Rappe, Casewit et al. 1992; Li 2001). The gold atoms forming the Au(1 1 1) plane were fixed and interacted through LJ potential with the atoms in the SAM chains. These intramolecular and intermolecular potential function parameters have been previously reported to accurately capture the equilibrium conformations, vibrational frequencies and excess enthalpies of the simulated molecules (Lifson and Warshel 1968; Engler, Andose et al. 1973). Only the atoms in the carboxylic acid end group were assigned point charges following the Mulliken charge analysis (Mulliken 1955). The long-range electrostatic pair interactions between the charged atoms were computed using Ewald summation routines available in LAMMPS. Details of potentials, point charges and associated numerical parameters for all the interactions simulated in the molecular simulation are presented in appendix.

5.3.2 Procedure for conformation simulation

In order to investigate the conformational transition, MD simulations were performed with a 1fs time step in three steps: initialization, thermalization and application of external electrical fields. For the initialization process, the system was given temperature of 0.45 K with NVT ensemble to minimize the initial energy of the ensemble. Subsequently, the system was kept at temperature of 200 until equilibrium was achieved with NVT ensemble. After that, external electrical fields with different field strengths were applied onto the SAM system with NVE ensemble till the system reached equilibrium. After equilibrium, the MD simulations were continued for period of 100 ps to extract statistical information about chain conformations. The simulations were repeated for different electrical field magnitudes ranging from positive maximum value of 2 V/Åto negative maximum value of −2V/Å with an increment of −0.5V/Å.

5.3.3 Procedure for indentation and sliding simulation

Contact and frictional response of the SAM systems were investigated with two different indenter geometries: cylindrical and spherical. The indenters were modelled as rigid and repulsive surface. The repulsive potential simulates hard indenter and has the following potential (Kelchner, Plimpton et al. 1998; Shimizu, Eda et al. 1998; Ohzono and Fujihira 2000):

$$V(r) = k(R - r)^3 H(R - r) \tag{5-2}$$

where r is the distance between the atoms in the indented SAM and the centre of the indenter surface, is the indenter radius and k is the stiffness constant for the indenter surface. H is Heaviside step function in order to ensure that only the atoms in contact with the indenter surface are subjected to repulsive force. In the simulations, the indenter radius, *R*, and stiffness, *k*, are set equal to 50 and 70 Nn/Å^2, respectively. The value of the indenter radius is chosen such that the rigid surface makes contact with multiple chains during the indentation and sliding simulations. The value of the indenter stiffness is chosen to ensure that the SAM atoms do not penetrate the indenter surface. In order to measure the response of the SAM covered surface, the indenter was moved downwards in range of velocities from 0.1 to 0.5 Å/ps and the contact load was monitored to determine the load–displacement response.

For the simulations, the SAM surfaces were first equilibrated under the desired electrical field following the procedure described above. Subsequently, the indenter was brought into contact with the SAM surface and frictional performance was determined at different normal loads and applied electrical fields. Sliding simulations for the SAM surface were performed in three steps: indentation, dwell and sliding. For the indentation process, the indenter was moved downwards at velocity of 0.25 Å/ps till it reached desired force level. At the dwell stage, the indenter was held stationary till the contact loads on the indenter reached steady value. For the sliding process, the indenter was maintained at constant height and moved forward at 1 Å/ps sliding velocity along the surface of the SAM system. The contact loads applied on the indenter were recorded to determine the normal and tangential forces. In order to examine the influence of SAM deformation and applied electrical field on friction performance, simulations were carried out for a range of indentation loads and applied electrical fields of −2, 0 and +2 V/Å.

5.4 Results

5.4.1 SAM conformation as function of electrical field

The total energy of the chains for typical conformation simulation is shown in Fig. 5-2. In the first stage of simulation at 0.45 K, the system undergoes energy minimization within 20 ps. As the temperature is increased to 200 K during the thermalization process, the total energy increases as the kinetic energy increases and reaches an equilibrium value after 20 ps. Applying an electrical field onto the system increases the potential energy and thus also increases the total energy of the system, which reaches an equilibrium value in 20 ps. The simulation was continued for 60 ps to capture statistical information on the chain conformation.

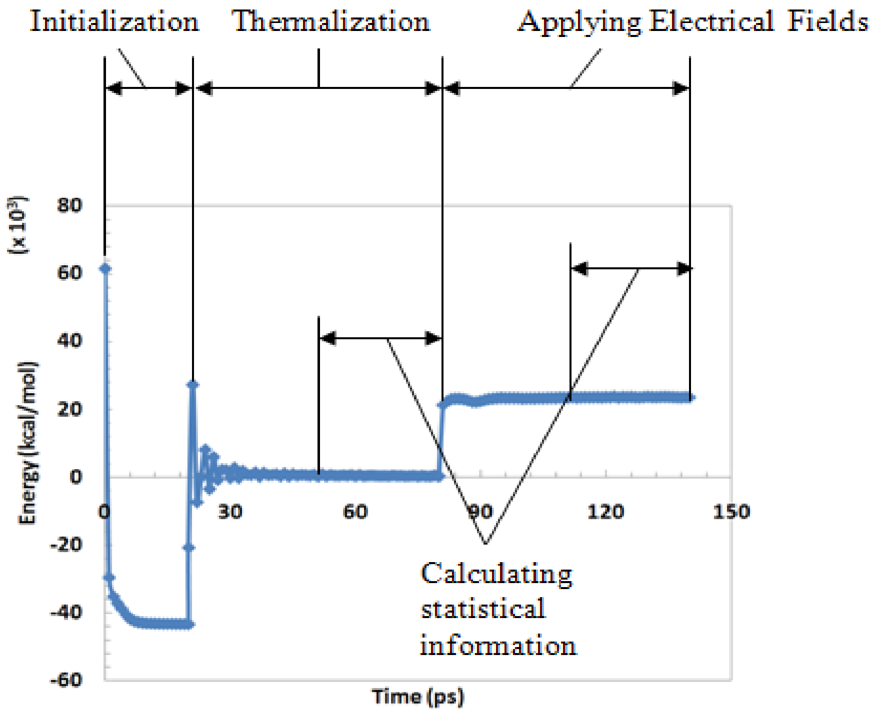

Fig. 5-2 Energy output for conformation simulation

The typical configurations of loose-packed MHA chains obtained under application of electrical fields of 2, 0 and −2V/Å are shown in Fig. 5-3(a), (b) and (c), respectively. The representative configurations of single chains for similar fields are shown in Fig. 5-4(a), (b) and (c). For the sparsely packed SAM, chains cluster together due to the intermolecular interaction and form disordered film structure on the gold surface. The application of electrical field changes the conformation of individual chains and also the chain arrangement in the SAM. The carboxyl head group consists of negatively charged oxygen atoms and positively charged carbon and hydrogen atoms, thus forming charged dipoles. Under the application of the positive electrical field, the force couple generated due to the carboxyl end group pulls the backbone chain down parallel to the surface and chains lie down in the form of clusters. The spatial constraints and the interchain interaction ensure that the backbone chains forming the cluster align parallel and anti-parallel to each other. Under neutral and negative electrical fields the chains remain standing up and their head groups cluster together due to the long-range attractive interactions. Under the negative electrical field, the moment generated due to the head group pulls the chain up but the stiffness of the backbone chain and long-range interaction between the neighbouring chains maintain the chain backbone in almost similar configuration as the neutral electrical field. However, the head group orientations for the chains under neutral and negative electrical fields are very different. The negatively charged oxygen atoms are repelled away and are more prominent in the top-most layers under negative electrical fields as compared with neutral fields.

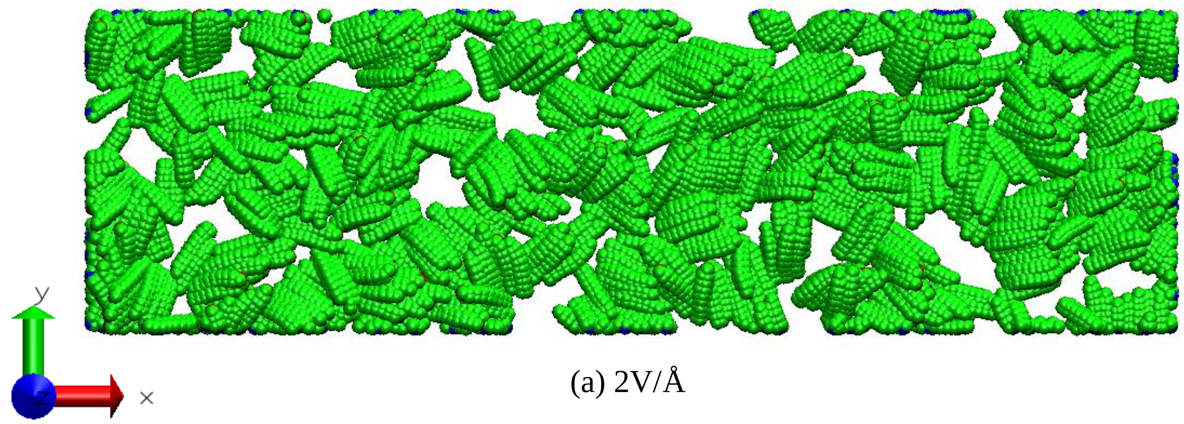

(a) 2V/Å

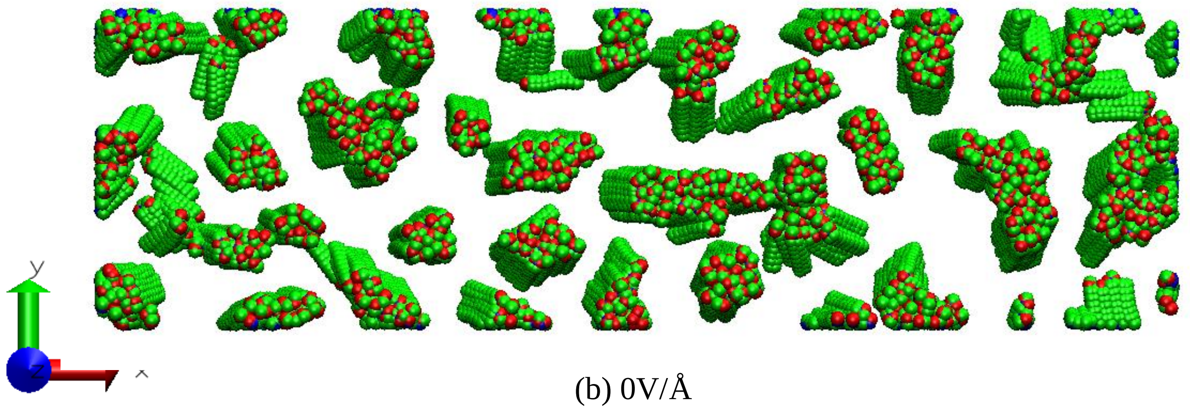

(b) 0V/Å

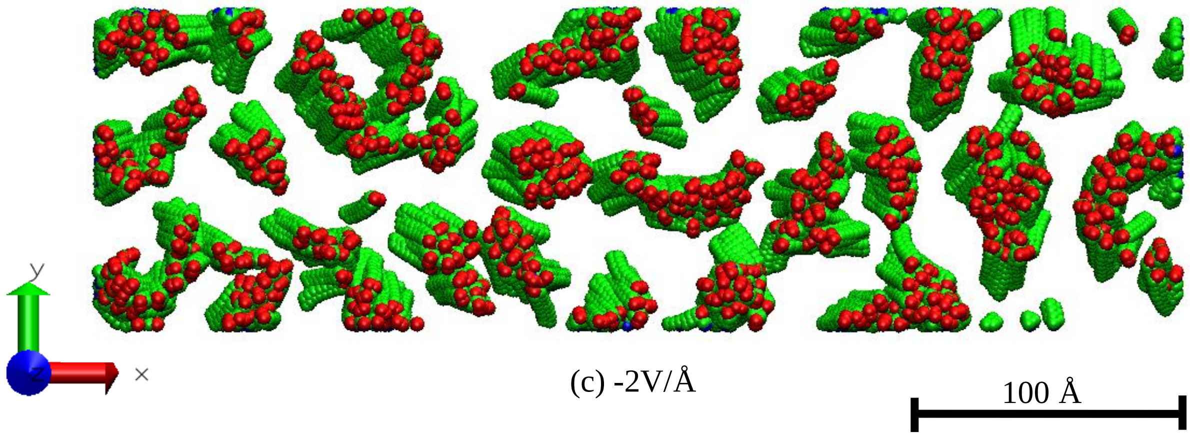

(c) -2V/Å

Fig. 5-3 Top layer snapshot and typical configuration of loose packed MHA chains after applying electrical fields

[Color representation: sulfur (black), carbon (blue), hydrogen (green) and oxygen (red)]

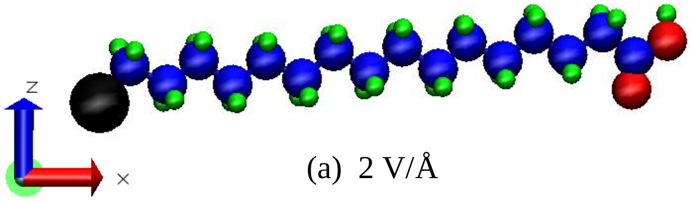

(a) 2 V/Å

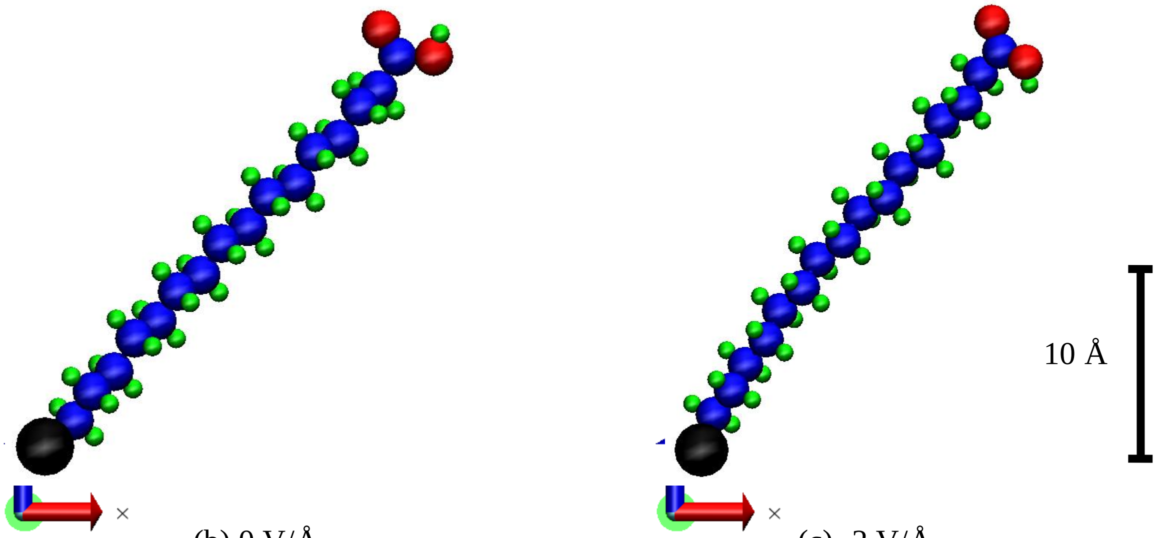

(b) 0 V/Å

(c) -2 V/Å

Fig. 5-4 Single chain snapshot and typical configuration of loose packed MHA chains after applying electrical fields

[Color representation: sulfur (black), carbon (blue), hydrogen (green) and oxygen (red)]

The influence of moment generated due to the polar head group can be clearly seen in the conformational transitions of individual chains, as shown in Fig. 5-4. The stiffness of the backbone chain ensures that the conformational change occurs only through chain rotation about the sulfur atom rather than bending of the backbone. Under the positive electrical field the chains are pulled down, whereas the backbone tilt remains similar for both neutral and negative electrical fields. The head group orientation in individual chains also strongly depends on the electrical field. In the carboxyl head group, the negatively charged oxygen atoms were pulled down under the positive electrical field, whereas they were pushed away under the negative electrical field.

The typical configuration of close-packed MHA SAMs obtained under application of electrical fields of 2, 0 and −2V/Å are shown in Fig. 5-5(a), (b) and (c), respectively. The configuration of a single chain in the close-packed MHA SAM for similar fields is shown in Fig. 5-6(a), (b) and (c). Due to the limited spatial availability, the backbone chains of the close-packed SAM maintain their orientation and regular arrangement for different fields.

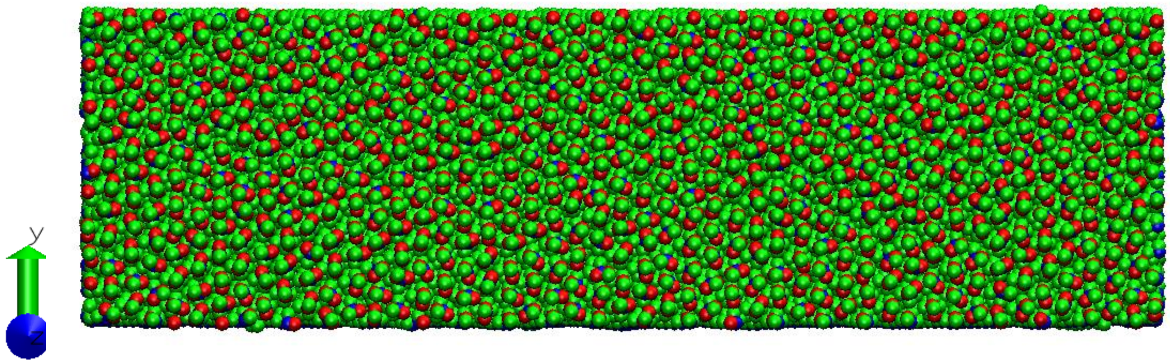

(a) 2 V/Å

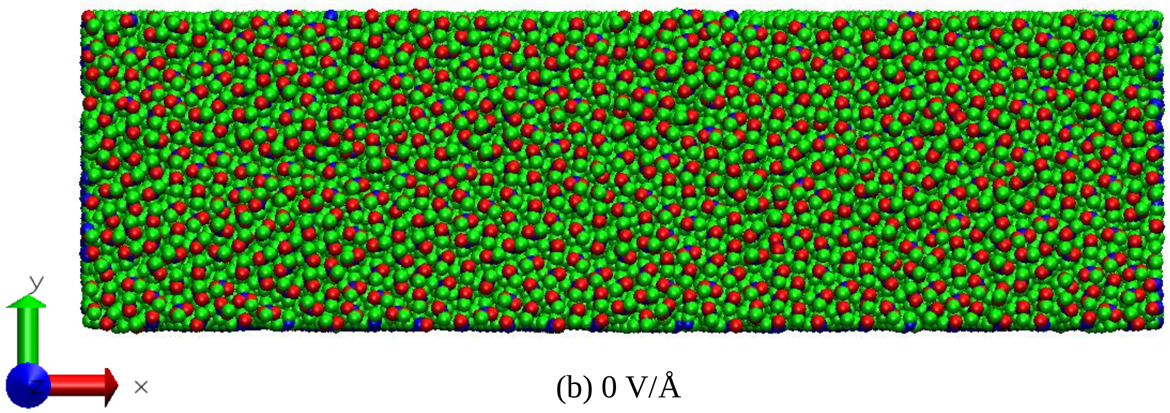

(b) 0 V/Å

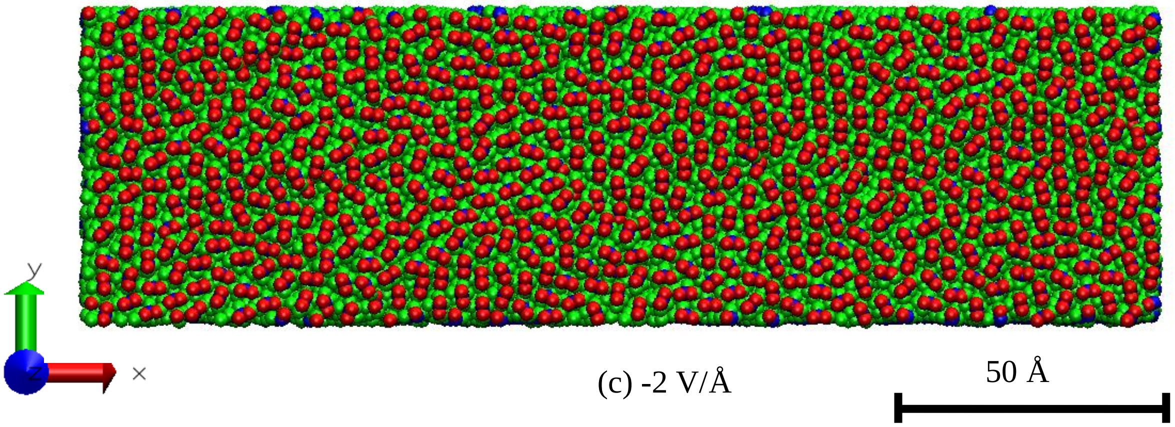

Fig. 5-5 Top layer snapshot and typical configuration of close packed MHA chains after applying electrical fields

[Color representation: sulfur (black), carbon (blue), hydrogen (green) and oxygen (red)]

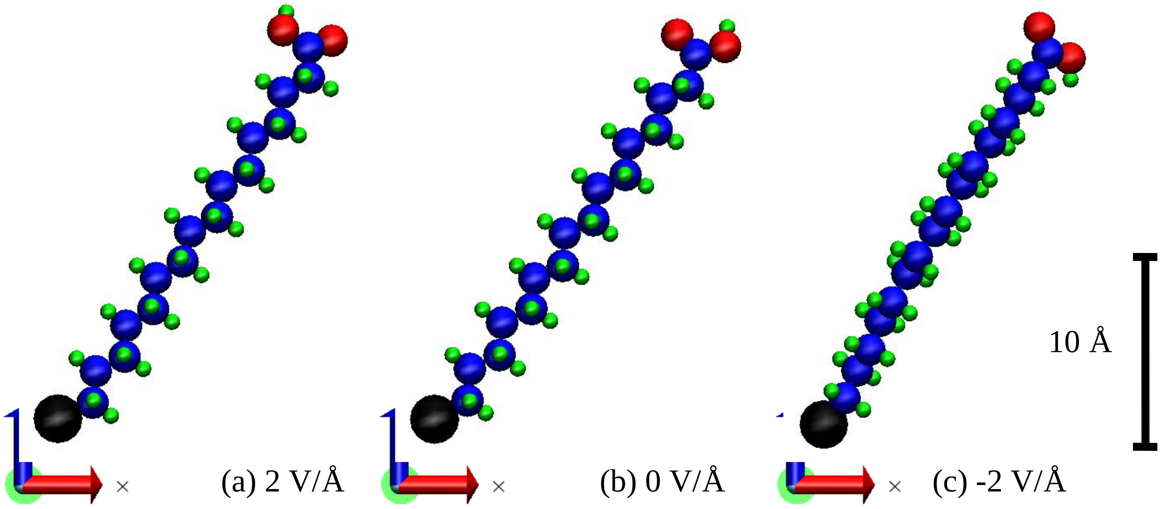

Fig. 5-6 Single chain snapshot and typical configuration of close packed MHA chains after applying electrical fields

[Color representation: sulfur (black), carbon (blue), hydrogen (green) and oxygen (red)]

The force couple generated due to the charged carboxylic head group results in the chain conformation shown in Fig. 5-6. Under the positive electrical field, the negatively charged oxygen atoms are pulled lower, whereas the application of the negative electrical field pushes them away from the gold surface. The changes in head group orientations result in different atoms being exposed on the SAM surface, as shown in Fig. 5-5. Under the positive and neutral electrical fields, hydrogen atoms as well as oxygen atoms are exposed; however, under the negative electrical field, negatively charged oxygen atoms are pushed out.

The field-induced conformational transitions of loose-and close-packed MHA chains are analysed through the height distribution of oxygen atoms. The average oxygen height for the two different SAM arrangements is presented in Table 5-1 as function of the applied electrical field. In addition, the height distributions for oxygen atoms in the loose-packed SAM are plotted in Fig. 5-7 for different electrical field magnitudes. The corresponding height distributions of oxygen atoms for close-packed SAMs did not show a large variation with changes in the electrical field and thus are not included in the paper.

Table 5-1 Average height of oxygen atoms

	2V/Å	1.5V/Å	1V/Å	0.5V/Å	0V/Å	-0.5V/Å	-1V/Å	-1.5V/Å	-2V/Å
Loose packed SAMs	6.85Å	7.49Å	11.3Å	18.0Å	18.8Å	18.0Å	17.4Å	17.3Å	17.5Å
Close packed SAMs	19.7Å	-	-	-	19.8Å	-	-	-	20.2Å

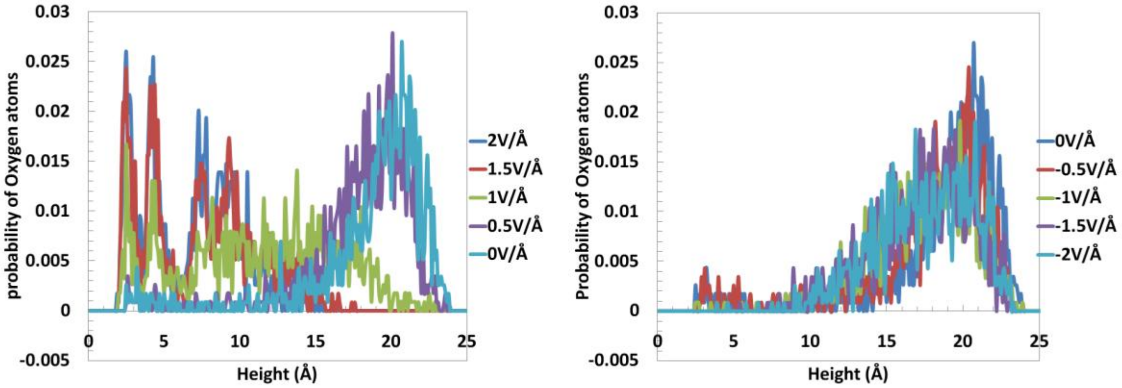

(a) Positive electrical fields

(b) Negative electrical fields

Fig. 5-7 Oxygen distribution calculation of loose packed MHA chains

As the magnitude of the applied positive electrical field increases, the average oxygen height in loose-packed MHA SAMs decreases indicating the pulling down of the chains under the electrostatic forces. The peaks in the oxygen height distribution functions show that at neutral and low electrical fields, the probability of finding the carboxylic end group near the average value is high indicating that all of the chains stand up. At moderate values of field strength, the average values of oxygen height reduce and chain head groups are distributed over a height range indicating that backbone chains have range of configurations from slightly bent to completely lying down. As the field is increased to the maximum value, the head groups settle around two different heights with narrower distributions indicating that most of the chains are pulled down to the surface.

While under negative electrical fields, the height distribution of the oxygen atoms did not show significant variation though the average oxygen atom height did show a slight decrease associated with the rotation of carboxylic head group to expose the negatively charged oxygen atoms.

Thus, positive electrical fields can trigger more prominent conformational transition for MHA chains in the sparsely packed SAMs and the chain conformation remains almost similar under neutral and negative electrical fields. For close-packed MHA SAMs, electrical fields have little influence on the height of the SAMs, all of the close-packed MHA chains always maintained their original height of around 20 Å. Thus, it is difficult for close-packed MHA chains to generate significant conformational transition.

The simulation results on the conformational transition of MHA SAMs under electrical fields are consistent with Lahann et al.'s (Lahann, Mitragotri et al. 2003) and Kanaga Karuppiah et al.'s (Karuppiah, Zhou et al. 2009) experimental observation of conformational transition. Lahann et al. (Lahann, Mitragotri et al. 2003) used sum-frequency generation (SFG) spectroscopy to show that for similar magnitude of electrical fields applied to sparse monomolecular SAMs, the positive electrical field pulled individual chains down to the surface, whereas the negative electrical field maintained the chain in the standing configuration. Kanaga Karuppiah et al. (Karuppiah, Zhou et al. 2009) used adhesion measurements with AFM tips to show that the application of similar magnitudes of electrical field resulted in changes in the surface properties indicating conformational transition of the SAM. In addition, MD simulation results on close-packed PEG SAMs (Vemparala, Kalia et al. 2004) show that the application of electrical fields on close-packed SAMs does not result in the deformation of backbone chains due to the spatial limitation, as observed in our simulation results on close-packed MHA SAMs.

In summary, the simulation results presented above show that at full coverage the SAM films form regularly packed uniform structure that is not disturbed during the application of electrical fields. However, at sparse coverage, the chains are arranged in irregular clusters on the surface and the orientation of the chains in the clusters changes with electrical fields. Under positive electrical fields, the chains in the cluster lie parallel and anti-parallel to each other. Under neutral and negative electrical fields, the clusters of chains are formed through coming together of chain head groups.

5.4.2 Friction simulation

The SAM surfaces were first equilibrated under the desired electrical field following the procedure described in the previous section. Subsequently, the SAM surfaces were indented with non-repulsive indenter. The load– displacement curve obtained from cylindrical indenter of 50 Å radius indenting the sparse SAM surface at velocity of 0.25 Å/ps under an electrical field of 2 V/ Å is plotted in Fig. 5-8. A similar qualitative response was determined for spherical indenters and sparse SAMs under different voltages as well as different indenter velocities from 0.1 to 0.5 Å/ps.

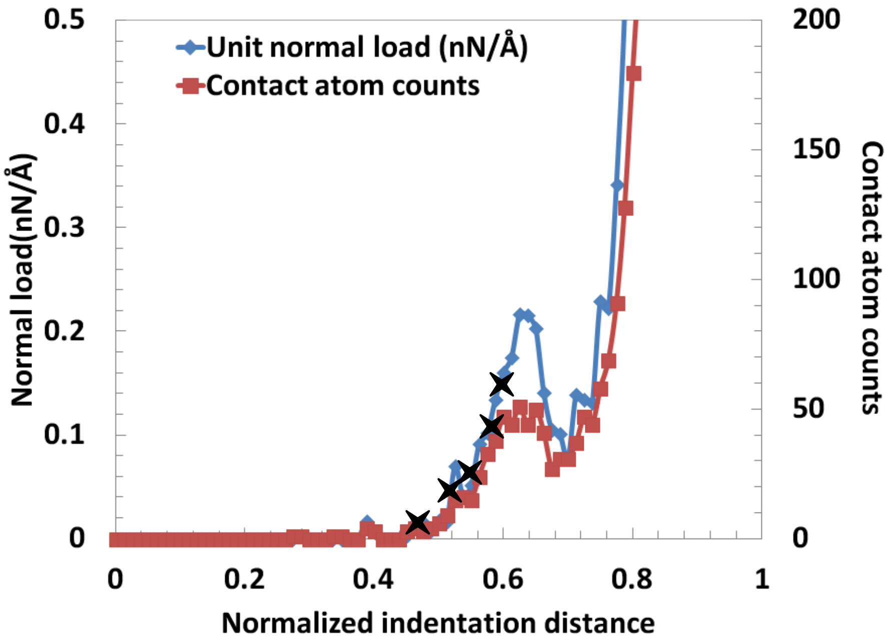

Fig. 5-8 Load–displacement profile for SAM indentation with a cylindrical indenter and selection of indentation depth for sliding simulations

In the case of rigid surface indenter, only the atoms in contact with the indenter are subjected to repulsive force and the number of atoms in contact with the indenter can quantify the average force acting on the contacting atoms. The chains may accommodate the deformation induced due to indentation either through backbone rotation that changes the interchain spacing, or through bending of covalent bonds along the chain backbone, or through compression of covalent bonds along the backbone.

The indenter load and the number of atoms in contact with the rigid indenter surface are plotted as function of the normalized indentation depth in Fig. 5-8. The normalized indentation depth, d, is defined as follows:

$$d = \frac{h_0 - h}{h_0} \qquad 0 < h < h_0 \tag{5-3}$$

where h is the height from the gold substrate (the same as the height in Fig. 5-6), and h_0 is the initial height of the indenter. The initial height for all the simulations was maintained to be about 10 Å above the highest atoms forming the SAM.

As the indenter is brought into contact with the SAM surface, the indentation load and the number of atoms in contact with the indenting surface increase with depth indicating that the average force per atom remains constant. As the indentation depth increases, the number of atoms in contact remains constant but the overall indentation load keeps on increasing, indicating that the average indention force per atom increases. But at critical indentation depth, both indentation load and number of atoms in contact suddenly drop before continuing monotonic increase with increasing indentation depth. The low coverage density of sparse SAMs allows interacting chain to move away from the indenter, therefore at the critical indentation depth, the repulsive forces are strong enough to drive the chains away from the indenter, which leads to the sudden load drop and reduction in number of atoms in contact with the indenter. Further indentation leads to monotonic increase as more chains and the rigid gold surface start interacting with the indenter. In the fully packed SAM film, the indentation response showed similar response of load drop at critical indentation depth for indenter shapes, applied electrical fields and indentation velocities. The chains do not have spatial room to move away from the indenter and thus, almost one magnitude larger indentation loads were associated with the observation of load-drop phenomena as compared with indentation loads for sparsely packed SAMs.

For both sparse and fully packed SAMs, the frictional behaviour shows two distinct responses corresponding to lower normal load and higher normal load level, respectively. In the current simulations, the indenter is modelled as repulsive rigid surface, therefore the frictional forces are based purely on repulsive forces applied to the atoms in contact with the indenter surface. These repulsive forces can either lead to localized deformation of the individual chains or at larger magnitudes can move whole chains along with the indenter leading to wear and distortion of the SAM structure. In the current simulations, the gold substrate is idealized as a rigid substrate, consequently, the simulations will lead to non-physical results at large loads since the deformation of the gold substrate is not simulated. Therefore, only the frictional results that correspond to low loads, shallow indentations and localized deformation of the SAM surface are reported. The friction response of the sparsely packed MHA films was measured at indentation load levels ranging from 0 to 0.2nN/Å for the cylindrical indenter and 0 to 2.5 nN for the spherical indenter, respectively. In the case of fully packed MHA films normal loads for sliding simulations varied from 0 to 1.2 nN/Å for the cylindrical indenter and 0 to 15 nN for the spherical indenter, respectively. The load level and the corresponding depths chosen for simulating the friction response are indicated by symbol (×) on the load– displacement curve in figure 8. These loads and depths were chosen to characterize the friction response before and after the observed load drop during the indentation.

The friction response on the SAM surface subjected to electrical fields was simulated in three steps: indentation to the desired load level with the indenting surface moving vertically down at speed of 0.25 Å/ps, dwell of indenting surface at the given height to reach constant normal load level and horizontal sliding of the indenter at constant height at horizontal velocity of 1 Å/ps. During the dwell period, constant load level was reached within 2–3 ps of simulation time and the dwell simulation was carried out for total of 20 ps to ensure that equilibrium is achieved. At each indentation depth, the equilibrium normal load levels reached during the dwell period were consistently lower than the indentation loads measured for the same depth. However, the equilibrium load levels for different depths still followed the same trend, i.e. initial increase, load drop and subsequent monotonic increase. After the dwell period, the indenting surface was moved horizontally at constant height with horizontal velocity of 1Å/ps. The ratio of the normal and tangential loads was monitored to determine the frictional coefficient on the SAM surface.

The average values of the friction coefficient measured during sliding simulations for shallow indentation of cylindrical and spherical indenters on loose-packed SAMs are plotted as function of normalized normal load in Fig. 5-9(a) and (b), respectively. The friction coefficients computed for sliding of cylindrical and spherical indenters on close-packed MHA SAMs are shown in Fig. 5-10(a) and (b), respectively. The range of friction coefficient (0.1–0.3) obtained in our simulation is comparable to the reported friction coefficient computation results for alkanethiol SAM surfaces in sliding contact (Harrison, White et al. 1995).

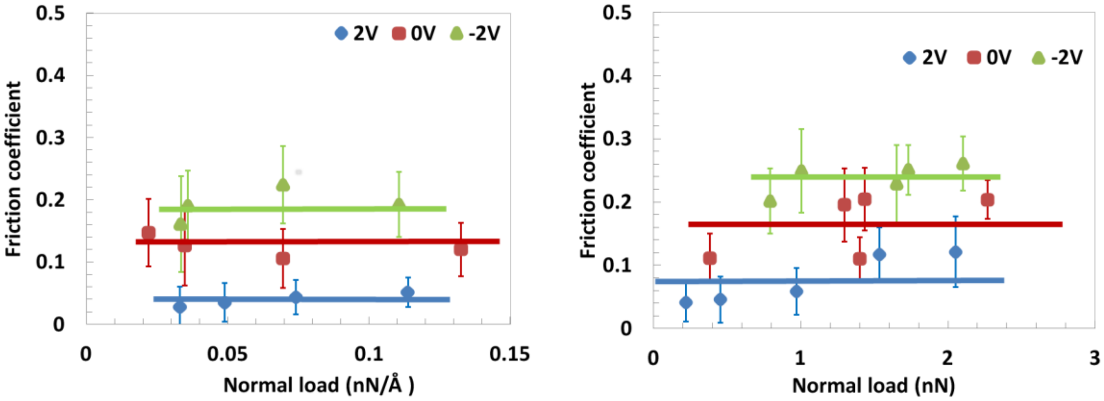

(a) cylindrical indenter (b) spherical indenter

Fig. 5-9 Frictional coefficient of loosed packed MHA SAMs

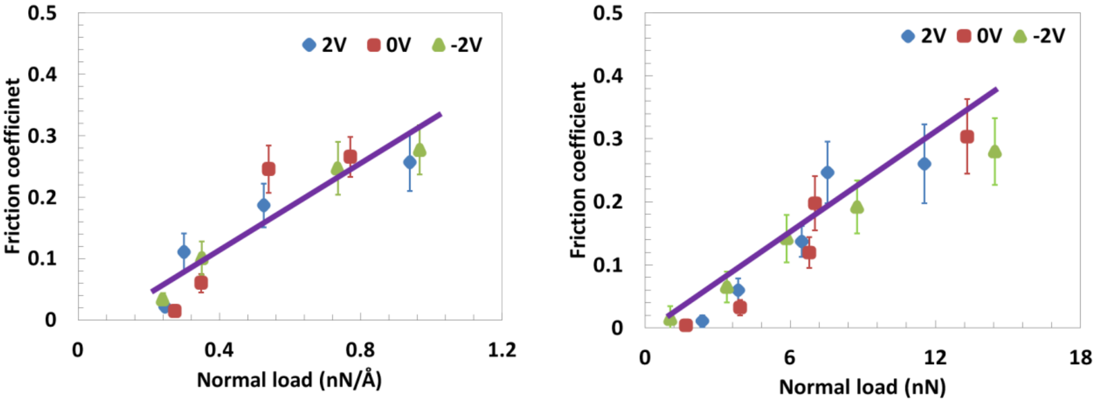

(a) cylindrical indenter (b) spherical indenter

Fig. 5-10 Frictional coefficient of closed packed MHA SAMs

During sliding simulations at shallow indentation, the repulsive force applied on the chains only cause bending and deformation of individual chains but the overall structure of the SAM film remains undisturbed. In order to demonstrate the localized deformation of individual chains, snapshots of a single chain from sparse MHA SAM subjected to an electrical field of 2 V/Å during sliding simulations with cylindrical indenter of radius 50 Å are shown in Fig. 5-11. Due to the interaction between the indenter and chains, the end group was pushed downwards and after the interaction, the chains can rebound to its original configuration. Similar chain deformations due to indenter interactions were observed for other indentation depths and applied electrical fields at shallow indentation.

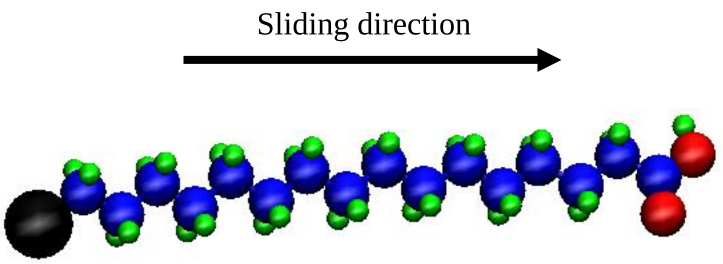

(a) Before sliding

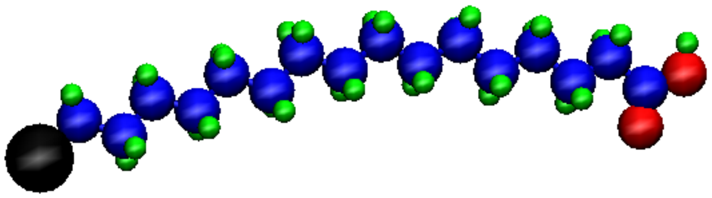

(b) During sliding

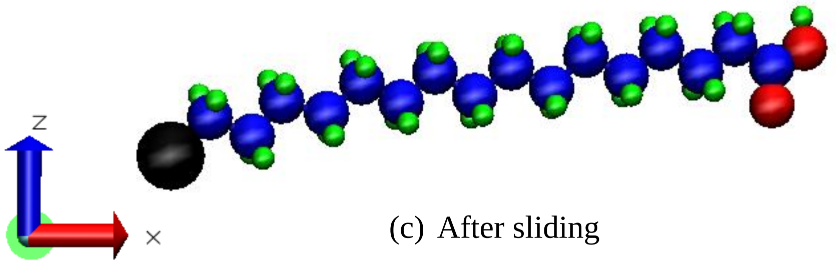

(c) After sliding

Fig. 5-11 Conformation changes in single chain from SAMs during the sliding process

For shallow indentation of loose-packed MHA SAMs (shown in Fig. 5-9), the frictional coefficients are independent of the applied load but demonstrate strong dependence on the applied electrical field. The friction coefficient is the lowest for the application of the positive electrical field and increases in value as the applied electrical field is changed to neutral and negative values. The dependence of the frictional coefficient on the applied electrical field is associated with different chain conformations. Changes in energy associated with bond, angle and dihedral potentials during the indenter sliding were monitored in order to quantify the deformation mechanism for the chains under an indenter load. The change in the respective energies during the sliding of the indenter is tabulated in Table 5-2.

Table 5-2 Percentage change of bonded energy

Bonded potential	$\frac{(E^{b}_{after} - E^{b}_{before})}{E^{b}_{before}}$
2V/Å	27.4%
0V/Å	34.7%
-2V/Å	36.5%

As the electrical field changes from positive to negative values, the total bond energies undergo increasingly larger changes. For similar indenter load levels, the chains in the standing up conformation undergo much larger energy change and consequently, larger deformation than chains in the lying-down conformation. The positive electrical field induces lying-down conformational transition, so chains have little space to generate a bending deformation. While, under neutral and negative electrical fields, the chains remain in the standing-up conformational status, and thus have more space to generate bending deformation and thus can induce more resistance and energy absorption during the indenter sliding process. In addition, the large separation between the chains ensures that the chain deformation due to the indenter is not constrained due to neighboring chains. Thus, as the indentation load is increased, more chains come into contact with the indenter but the load required to deform each chain remains nearly the same ensuring that the friction coefficient remains nearly constant.

The close-packed SAMs under shallow indentation show trend of increasing friction coefficient with increasing normal load. As the indentaion load is increased, more chains come in contact with the indenter and are deformed during sliding. Close packing of the chain ensures that the deformation of chains is influenced due to the presence of neighbouring chains and hence, the load required to deform each additional chain increases as the available space is used up. Consequently, as the indentation load is increased additional chains come into contact and the increase in load required to deform the additional chains ensures that the friction coefficient keeps on increasing. The chains in the close-packed SAMs remain standing and do not undergo significant conformational transition under the applied electrical field and consequently, the frictional response is found to be independent of the applied electrical field.

Previous simulation results have also shown that the frictional coefficients remain independent of normal loads for disordered SAMs (Chandross, Webb et al. 2004; Chandross, Lorenz et al. 2005), and increase linearly with indentation loads for fully packed regular SAM structures (Harrison, White et al. 1992; Harrison, White et al. 1995).

In the case of shallow indentation with repulsive rigid indenting surface, localized chain deformation is the primary mechanism that determines the resistance to tangential motion. Electrical field induced chain conformation and SAM density determine the magnitude as well as the dependence of tangential resistance on the applied normal load. The simulations reported in this paper are performed by assuming that the underlying substrate is rigid surface.

5.5 Conclusions

Simulations of chain conformation and frictional response in SAMs of carboxyl head group alkanethiols under an applied electrical field lead us to the following conclusions:

(1) Sparse monomolecular films are composed of clusters that form due to coming together of head groups under interchain attraction. The application of an electrical field changes the conformation as well as the chain arrangement in the clusters.

(1a) Under the application of positive electrical fields, the chain backbone rotates to undergo transition from standing to lying-down conformation. In addition, the chains arrange in parallel and antiparallel arrangements to form disordered clusters on the surface.

(1b) Under the application of negative electrical fields, the chain backbone remains in the standing-up conformation and the chains still form the disordered clusters on the surface.

(2) Close-packed SAMs under electrical fields do not undergo any conformational transition associated with backbone rotation.

(3) Under shallow indentation with repulsive rigid indenting surface, the SAM chains provide tangential resistance through localized chain deformation. For sparsely packed SAMs, positive electrical fields induce smaller frictional coefficient than neutral and negative fields. While for close-packed SAMs, all kinds of electrical fields lead to similar frictional coefficients.

5.6 Appendix

Interatomic potential functions and associated numerical parameters

Bonded	Bonds	Harmonic: $\sum_{i,j} k_{ij}\left(r_{ij}-r_0\right)^2$
	Angles	Harmonic: $\sum_{i,j,k} k_{ijk}\left(\theta_{ijk}-\theta_0\right)^2$
	Dihedrals	Charmm: $\sum_{i,j,k,l} k_{ijkl}\left[1+\cos(n\varphi_{ijkl}-\varphi_0)\right]$
Nonbonded	Lennard Jones	Universal Force Field: $V=\sum_{i,j} 4\varepsilon_{ij}\left[\left(\frac{\sigma_{ij}}{r_{ij}}\right)^{12}-\left(\frac{\sigma_{ij}}{r_{ij}}\right)^{6}\right]$
	Electrostatic	Coulombic: $\sum_{i,j} C\frac{q_iq_j}{r_{ij}}$
	Morse	For Au/S interaction: $\sum_{i,j} D_{ij}\left[e^{-2\alpha(r_{ij}-r_0)}-2e^{-\alpha(r_{ij}-r_0)}\right]$
Electrical field		q_iEz_i

Bond (Harmonic) potential parameters:

	k_{ij} (Kcal/mol)	r_0 (Å)
S-C	450	1.81
C-C	200	1.53
C-H	300	1.08
C-C(=O)	405	1.53
C=O	580	1.23
(O=)C-O	450	1.38
OH	450	0.96

Angle (Harmonic) potential parameters:

	k_{ijk} (Kcal/mol)	θ_0 (Degree)
S-C-H	40	109.5
S-C-C	50	112.5
H-C-H	40	109.5
C-C-H	40	109.5
C-C-C	45	111
C-C-C(=O)	70	109.5
H-C-C(=O)	70	109.5
C-C=O	85	118.5
C-C(=O)-O	85	120
O=C-O	85	120
C-O-H	50	109.5

Dihedral (Charmm) potential parameters:

	k_{ijk} (Kcal/mol)	φ_0 (Degree)	n
S-C-C-H	1.6	0	3
S-C-C-C	1.6	0	3
H-C-C-H	1.6	0	3
H-C-C-C	1.6	0	3
C-C-C-C	1.6	0	3
C-C-C-C(=O)	1.6	0	3
H-C-C-C(=O)	1.6	0	3
C-C-C=O	0	0	3
H-C-C=O	0	0	3
C-C-C(=O)-O	0	0	3
H-C-C(=O)-O	0	0	3
C-C-O-H	1.8	180	2
O=C-O-H	1.8	180	2

Morse potential parameters:

	D_{ij} (Kcal/mol)	α ($Å^{-1}$)	r_0 (Å)
Au-S	3.182	1.378	2.903

Nonbonded intermolecular potential function (LJ potential) parameters:

	ε_{ij} (Kcal/mol)	σ_{ij} (Å)
Au-C	0.06399	3.1726
Au-H	0.04142	2.7465

Au-O	0.04837	3.0245
S-S	0.27400	3.5948
S-C	0.16962	3.5119
S-H	0.10980	3.0402
S-O	0.12822	3.3480
C-C	0.10500	3.4309
C-H	0.06797	2.9700
C-O	0.07937	3.2708
H-H	0.04400	2.5711
H-O	0.05138	2.8315
O-O	0.06000	3.1181

Point charges in carboxyl headgroup:

C	O (double bond)	O (single bond)	H
0.53	-0.38	-0.548	0.398

CHAPTER 6. SIMULATION AND EXPERIMENTAL INVESTIGATION OF ELECTRICAL FIELD MODULATED SELF ASSEMBLED MONOLAYER

(A paper prepared for submission to Langmuir)

Xiao Ma, Pranav Shrotriya, Kanaga Karuppiah, Sriram Sundararajan
Department of Mechanical Engineering, Iowa State University, Ames, IA50011

6.1 Abstract

Sparse self assembled monolayers (SAMs) have high feasibility and flexibility to undergo conformational transition under various external condition changes. The effect of electrical field actuated SAMs conformational transition was investigated by both molecular dynamics (MD) simulation and atomic force microscopy (AFM) experimental methods. Simulation results showed that under positive electrical field, SAM chains were pulled down onto the substrate, and exhibited longer distance order; while under negative electrical field SAM chains were pushed straight up from the substrate, and exhibited shorter distance order. Experimental results proved the conformational transition that illustrated by simulation, and indicated that the order of monolayer structure might be a more prominent factor than surface chemistry for frictional performance, which could also be supported by the SAM structural analysis from simulation.

Keywords Molecular dynamics simulation Atomic force spectroscopy
Self-assembled monolayer Conformational transition

6.2 Introduction

Research on sparse self assembled monolayers (SAM) has recently been a promising topic due to their flexibility to undergo conformational transition under various external condition changes (Vemparala, Kalia et al. 2004; Pei and Ma 2005; Ghorai and Glotzer 2007; Gus'kova, Mena-Osteritz et al. 2007; Osnis, Sukenik et al. 2012), and thus implies a potential for smart surface design in micro/nano electronics (Schon, Meng et al. 2001; Schon, Meng et al. 2001; Fan, Yang et al. 2002; Stapleton, Harder et al. 2003; Fan, Yao et al. 2004), microfabrication (Ulman 1990; Jackman, Wilbur et al. 1995; Wilbur, Kumar et al. 1996; Azzaroni, Schilardi et al. 2003; Liu and Cui 2005), tribology (Srinivasan, Houston et al. 1998; Maboudian, Ashurst et al. 2000; Sundararajan and Bhushan 2001), and biomedical applications (Kane, Takayama et al. 1999; Zhao, Wang et al. 2011). Among various methods to actuate molecules and induce conformational transition, application of electrical field is a compelling and controllable way with considerable feasibility and engineering application perspective.

Lahann et al. (Lahann, Mitragotri et al. 2003) invented a way to generate sparse mercapto-hexadecanoic acid (MHA) SAM and induced the electrical field on thin film to generate conformational transition. Due to the polar nature of the carboxyl group, under positive electrical field chains were bent down upon the substrate, while under negative electrical field chains were pushed straight up. This conformational transition could shift the surface of MHA from hydrophilic to hydrophobic nature. Liu et al. (Liu, Fujisawa et al. 2000) utilized scanning force microscopy (SFM) to study the microtribological properties of Langmuir-Blodgett (LB) monolayer films under modulation of electric fields. They found the friction force of the film increased with a DC field. However, by applying a specific combination of AC voltage and frequency, the friction force almost reached zero and the wear-life of the film was greatly extended.

Karuppiah et al. (Karuppiah, Zhou et al. 2009) measured the adhesion and frictional response of a sparse MHA SAMs under electrical fields by using atomic force microscopy (AFM). Higher adhesion was found under negative electrical fields, while lower friction level was obtained. This contrary phenomenon was explained by the change in the structural and crystalline order of the SAMs. Specifically, the more ordered structure under negative electrical field decreased the friction, though higher adhesion was caused by the hydrophilic interaction between the probe tip and SAM end group. This indicates that the order of structure for the thin film has a more prominent influence on frictional performance than deformation.

Vemparala et al. (Vemparala, Kalia et al. 2004) applied MD to investigate the electrical field actuated conformational transition of polyethylene glycol (PEG) SAMs. Due to the polar nature of the glycol groups, the conformational transition from “all-trans” status to “gauche” status was observed. Under negative electrical field the distribution of chains is more ordered with exposed oxygen atoms, while positive electrical field introduces considerable disorder in the system and the oxygen atoms are buried inside. Pei et al. (Pei and Ma 2005) conducted MD simulation to investigate the electric field induced switching behaviors of low-density mixed ω-carboxyalkyl/alkyl covered H-Si(111) surfaces. They found the reversibly conformation transition between the all-trans state and mixed gauche-trans state triggered by the applied electric fields ranging from -0.2 V/Å to 0.7 V/Å. They also discovered that by lowering the ionic strength and additions of acetonitrile molecules in the surrounding solution, the value of critical intensity of the electric field required for triggering the conformational transition was substantially decreased, hence switching could be facilitated. Other studies on the SAM's conformational transition and associated tribological performance have also been reported (Tupper and Brenner 1994; Bonner and Baratoff 1997; Harrison, Tutein et al. 1999; Harrison 2001; Bat-Uul, Fujii et al. 2004; Jang, Jang et al. 2005; Leith and Morton-Blake 2005; Sung and Kim 2005; Hu, Zhang et al. 2006; Wu, Lin et al. 2007; Harrison, Schall et al. 2008; Chang, Fang et al. 2009; Fang, Chang et al. 2009; Ramin and Jabbarzadeh 2011; Zhao, Duan et al. 2011; Wu, Fang et al. 2013).

In this paper, molecular dynamics simulation is utilized to investigate the conformational transition of MHA SAMs actuated and modulated by electrical fields. Atomic force microscopy was conducted to validate the conformation transition results of simulation and determine the most prominent factor influencing frictional performance of SAMs, which can be further explained by the simulation.

6.3 Experiment

6.3.1 Preparation of low-density MHA SAM

In order to generate the low-density mercaptohexadecanoic acid (MHA) SAM on gold substrate for implementation of the comformational transition, a SAM precursor mercaptohexadecanoic acid (2-chlorophenyl)diphenylmethyl ester (MHAE) containing a bulky end group was adopted to constrain the packing density by immersing the gold substrate in a 1-mM MHAE ethanolic solution for 24 h at room temperature. After removal of the solution and drying procedure, the bulky ester end group could be removed by incubating the sample in a 50% trifluoroacetic acid (TFA) in anhydrous ethanol for 2 min following by the rinsing and drying procedures. Then the substrate covered by MHA SAM with low packing density was expected to achieved (Karuppiah, Zhou et al. 2009), as shown in Fig. 6-1. X-ray photoelectron spectroscopy (XPS), and ellipsonmetry measurements were performed to confirm the complete cleavage of the bulky ester end group and presence of MHA SAM on substrate (Karuppiah, Zhou et al. 2009).

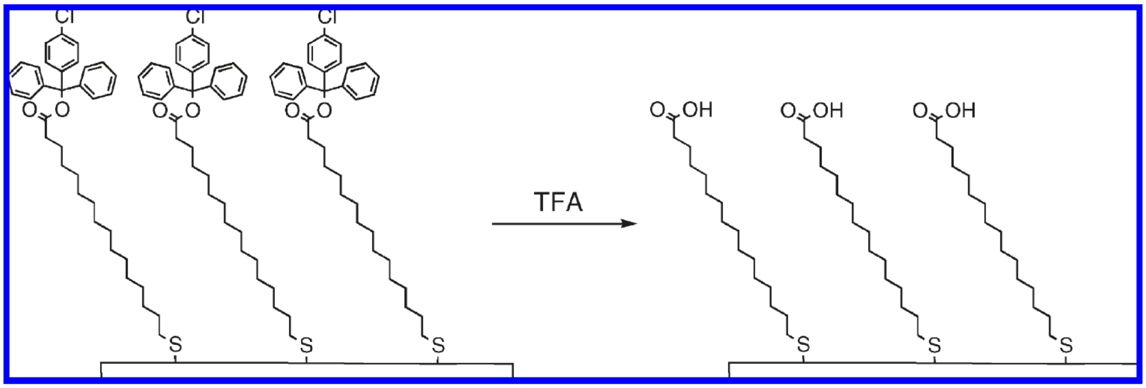

Fig. 6-1 Scheme of preparation of low-density MHA SAM

6.3.2 AFM based experiment for adhesion and friction measurement

Pull-off force and friction experiments were conducted using Dimension 3100 (Nanoscope IV, Veeco Instruments, Santa Barbara, CA) AFM to study adhesion and friction. under electrical field application of -10V, 0V and 10V respectively. The gold coated cantilever/probe was connected to ground, and a electric bias with respect to the ground was applied to metallic sample holder which was connected to gold substrate via conductive copper tape (Karuppiah, Zhou et al. 2009), as shown in Fig. 6-2.

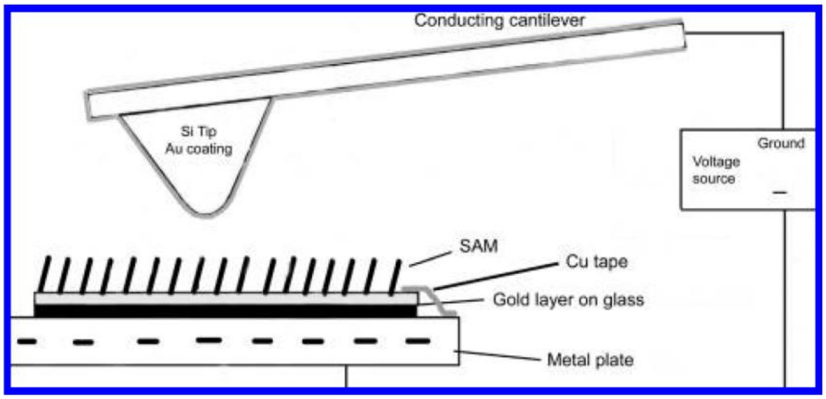

Fig. 6-2 Scheme of AFM setup and electrical field application

6.4 Simulation

6.4.1 Model and interatomic potential

MD simulations were performed by using LAMMPS (http://lammps.sandia.gov/) to investigate conformational transitions of MHA SAMs under applied electrical fields. 576 chains of MHA (S-$(CH_2)_{15}$-COOH) were generated as the (√3 × √3) R30° lattice structure at an approximate 30 °initial tilt angle with respect to the normal vector on Au(1 1 1) plane (Zhang, Goddard et al. 2002). The molecules were arranged in sparse coverage density withinter-chain space of 10Å.

The interatomic potentials applied to the SAMs are composed of three parts: bonded, nonbonded and applied electrical field terms.

$$V = V_{bonded} + V_{nonbonded} + V_{electrical\ field} = (V_{bond} + V_{angle} + V_{dihedral} + V_{improper}) + (V_{lennard\ jones} + V_{coulombic} + V_{morse}) + V_{electrical\ field} \tag{6-1}$$

The covalent bond interaction in the MHA SAMs were computed using CHARMM potentials (Brooks, Bruccoleri et al. 1983; Jaffe, Smith et al. 1993; Smith, Jaffe et al.

1993), and Morse potential is utilized to simulate the bond between sulfur and gold atoms (Pertsin and Grunze 1994; Zhang, Goddard et al. 2002). Lennard Jones (LJ) potential was used to calculate interaction among atoms other than bonded and morse potential interactions (Sorensen, Liau et al. 1988; Rappe, Casewit et al. 1992). Point charges were assigned to carboxyl group in MHA SAMs following the Mulliken charge analysis (Mulliken 1995), and the long-range electrostatic pair interactions between the charged atoms were computed using Ewald summation routines available in LAMMPS. External electrical fields were used to simulate the influence of electrical field.

6.4.2 Procedure of simulation

MD simulations were performed with time step of 1fs in three consecutive procedures: initialization, thermalization and application of electrical field. The MHA SAMs were first assigned a temperature as 0.45 K with NVT ensemble to minimize the initial energy, then the system was kept at temperature of 200 K with NVT ensemble until it reached equilibrium. Finally, electrical fields with different field strength ranging from -2 V/Å to 2 V/Å, were applied onto the thin film with NVE ensemble till the system acchived equilibrium. After equilibrium, the MD simulations were continued for a period of 60ps to apply statistical analysis.

6.5 Results and discussion

Total energy output from MD simulation is shown in Fig. 6-3. In the first stage of simulation at 0.45 K, SAMs reached energy minimization state within 20ps. As the temperature increased to 200 K, the total energy increased along with the increase of kinetic energy and achieved an equilibrium state within 20ps. After electrical field was applied onto the system, the total energy increased along with the increase of potential energy and reached an equilibrium state within 10ps. The simulation was then continued for 50ps to apply statistical analysis for illustrating conformational transition.

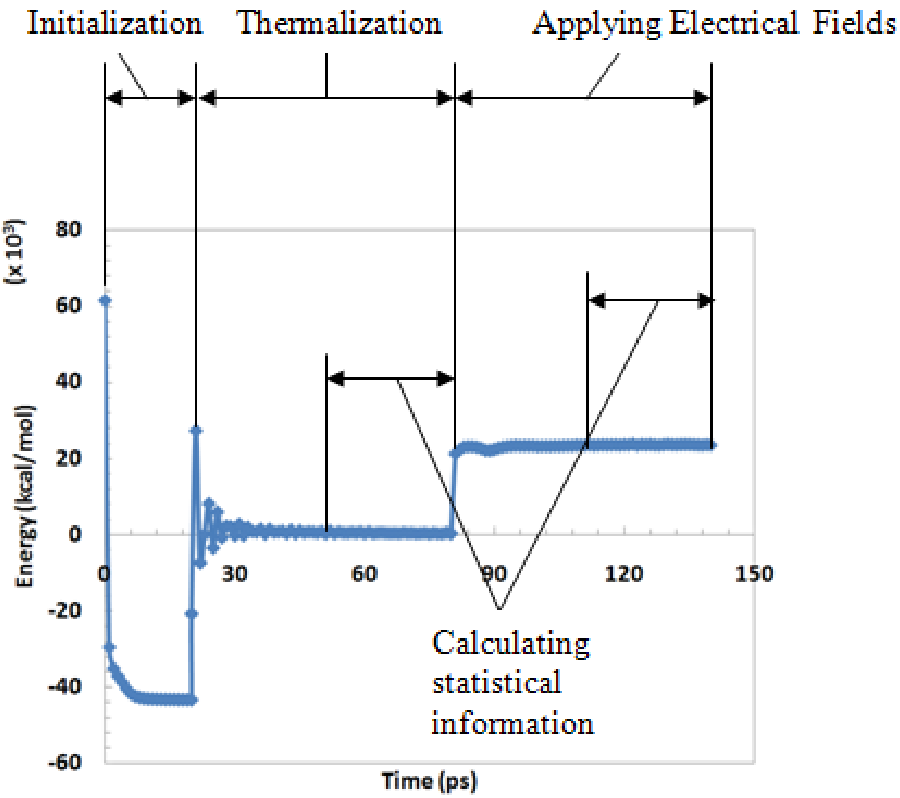

Fig. 6-3 Energy output for conformation simulation

The top layer snapshot of sparse MHA SAMs under different electrical field conditions from MD simulation are shown in Fig. 6-4. For all of the three cases, the chains aggregated together and showed clustered configuration no matter whether electrical fields were applied. Backbone chains were bent down onto the substrate under the positive electrical field, while the chains were pulled straight up under the negative electrical field. From the single chain snapshot shown in Fig. 6-5, within the carboxylic acid head group, the negative charged oxygen atoms were pulled downwards and buried inside under positive electrical field, while they were pushed up and exposed under negative electrical field.

The average height of double bond oxygen atoms in carboxylic end group from MD simulation was shown in Table 6-1, and the detailed height distribution of double bond oxygen atoms was analyzed and shown in Fig. 6-6. When positive electrical fields were applied to SAMs, the average height of oxygen atoms in the carboxylic end group of sparse MHA SAMs decreased gradually, and reached the minimum value at 2 V/Å, which implied chains were pulled down towards the substrate by electrostatic forces. Under zero and negative electrical fields, the peak of height distribution located around 20Å indicated chains were kept in standing state. At the maximum positive field strength of 2 V/Å, the double bond oxygen atoms in end groups showed very sharp peaks in height distribution at 2.5 Å and 7.3 Å, as shown in Fig. 6, which indicated the SAMs reoriented to achieve those energy-stable states and most of chains had been pulled down onto the substrate. For zero electrical field, height distribution of the double bond oxygen atoms always exhibited a broader distribution. Under negative electrical fields of -2 V/Å, there was no significant variation on the height distribution of double bond oxygen atoms, though a slight decrease of the average height was identified with respect to zero electrical field, which might be related to the rotation of carboxylic end group so as to expose the negatively charged oxygen atoms. In summary, positive electrical fields can induce more prominent conformational transition for sparse MHA SAMs compared to negative electrical fields.

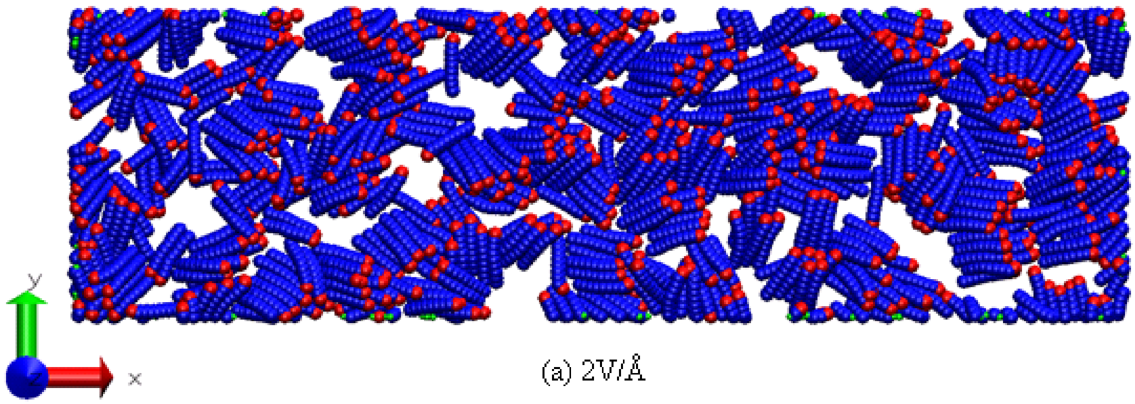

(a) 2V/Å

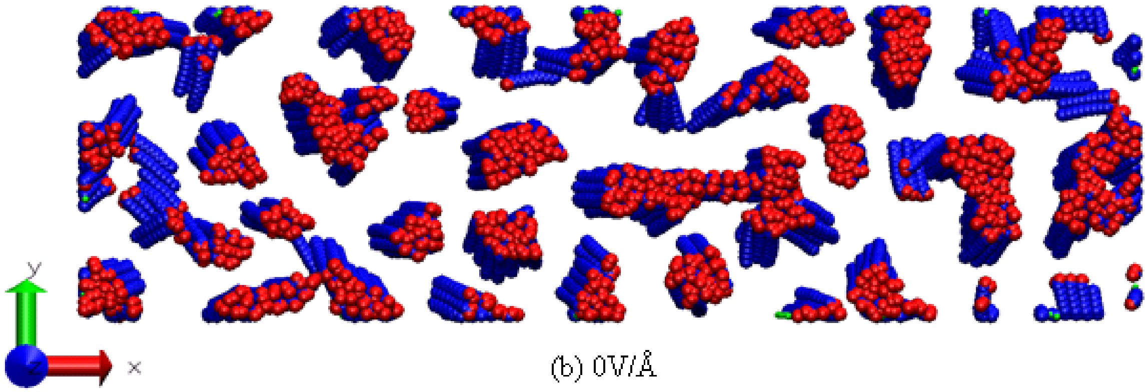

(b) 0V/Å

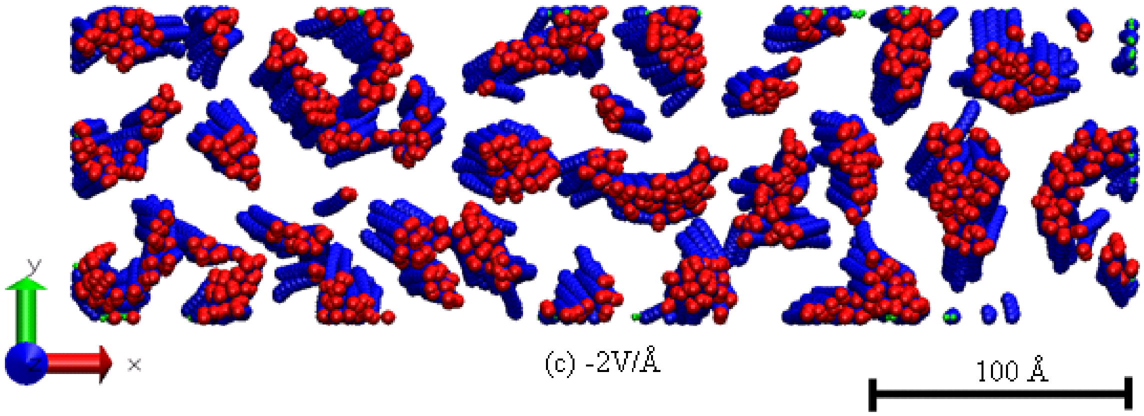

(c) -2V/Å

Fig. 6-4 Top layer snapshot of low-density MHA chains after applying electrical fields

[Color representation: sulfur (black), carbon (blue), hydrogen (green) and oxygen (red)]

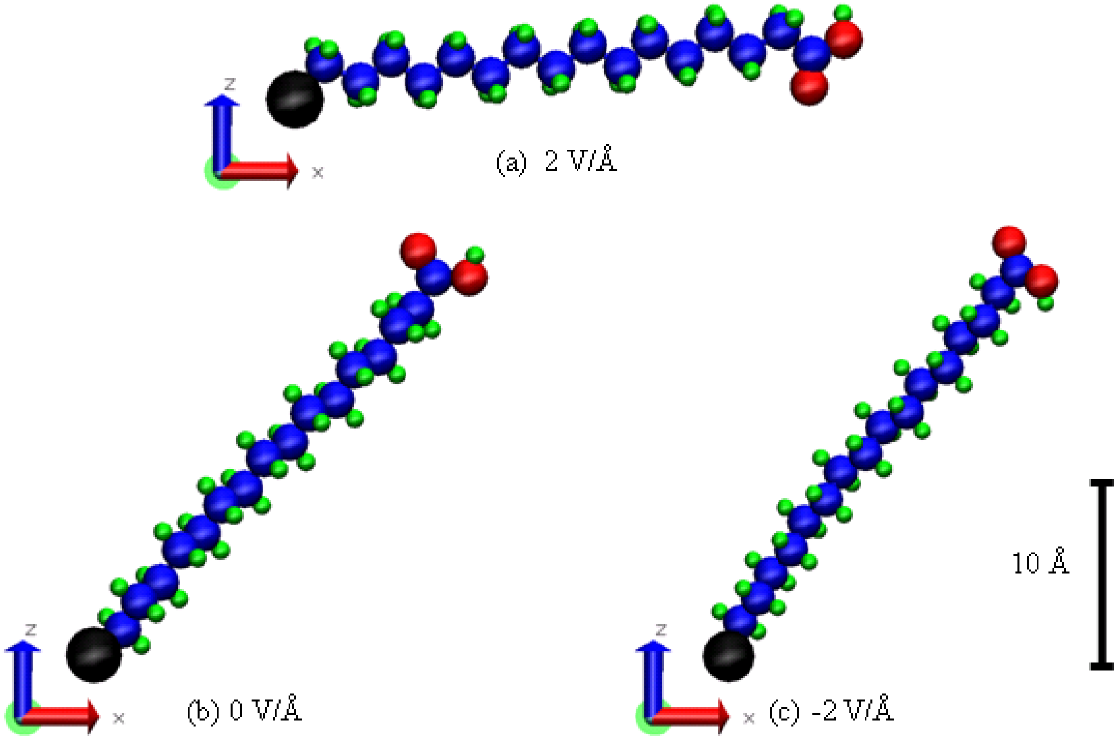

Fig. 6-5 Single chain snapshot of loose packed MHA chains after applying electrical fields

[Color representation: sulfur (black), carbon (blue), hydrogen (green) and oxygen (red)]

Table 6-1 Average height of oxygen atoms

	2V/Å	1.5V/Å	1V/Å	0.5V/Å	0V/Å	-0.5V/Å	-1V/Å	-1.5V/Å	-2V/Å
Ave. Oxygen height	5.3Å	7.5Å	11.5Å	18.0Å	19.0Å	17.8Å	17.6Å	17.6Å	17.5Å

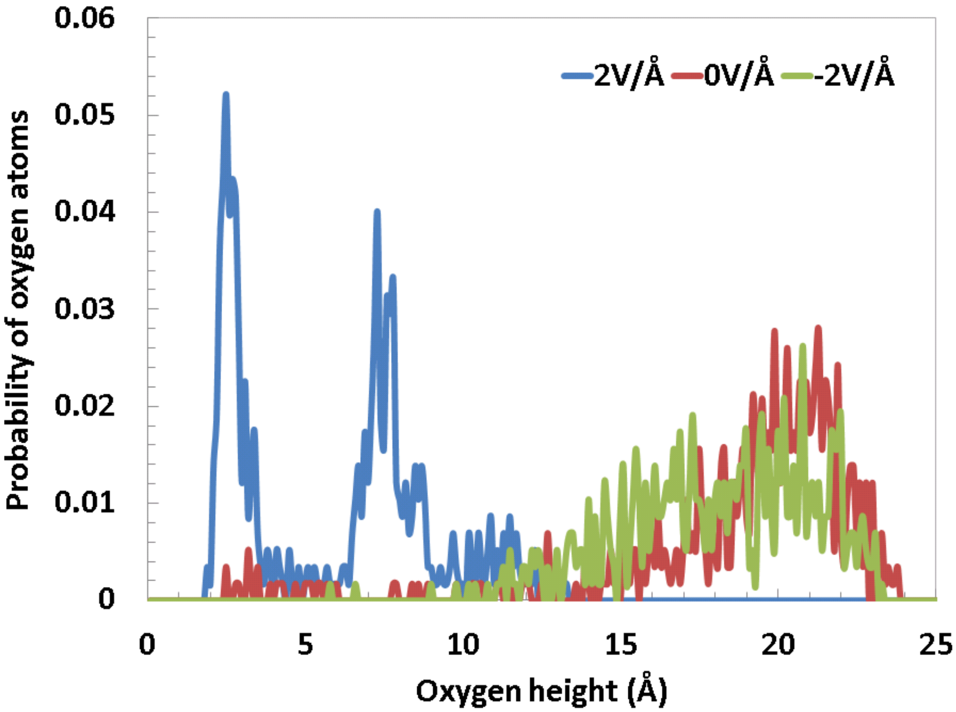

Fig. 6-6 Height distribution of double bond oxygen atoms in carboxylic end group

The comparison of height distribution for double bond oxygen atom in carboxylic group and carbon in the last methylene group from MD simulation are shown in Fig. 6-7, in terms of positive, zero and negative electrical field, respectively. Under positive electrical field of 2 V/Å, peaks of carbon atoms in backbone chains shifted to the right side of double bond oxygen atoms in end groups, which implied the height of the hydrocarbon backbone chain was higher than that of carboxylic end group, thus the hydrophobic portion of the SAMs, i.e. backbone chains was exposed as the top surface of SAMs. In contrast, under zero and negative electrical fields, peaks of double bond oxygen atoms in end group shifted to the right side of carbon atoms in backbone chains, which implied the height of carboxylic end group was higher than that of hydrocarbon backbone chain, thus the hydrophilic portion of the SAMs, i.e. the carboxylic end group was exposed as the top surface of SAMs. In summary, we can postulate that the polarity change of electrical fields can trigger the hydrophilicity transition of MHA SAMs, thus alter the surface chemistry. This result is consistent with the adhesion measurement from AFM experiments, as shown in Fig. 6-8.

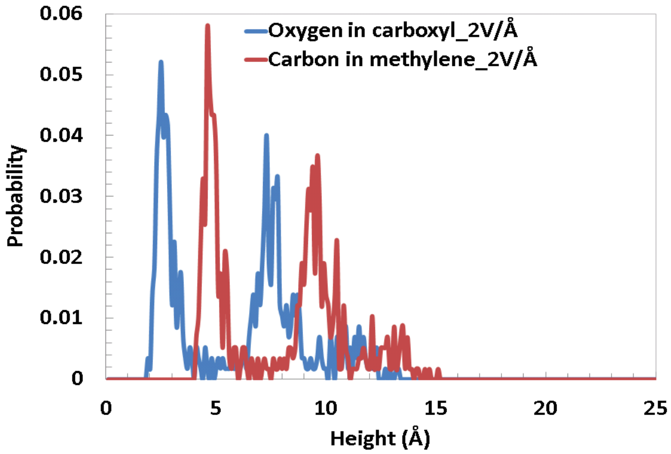

(a) Positive electrical field (2 V/Å)

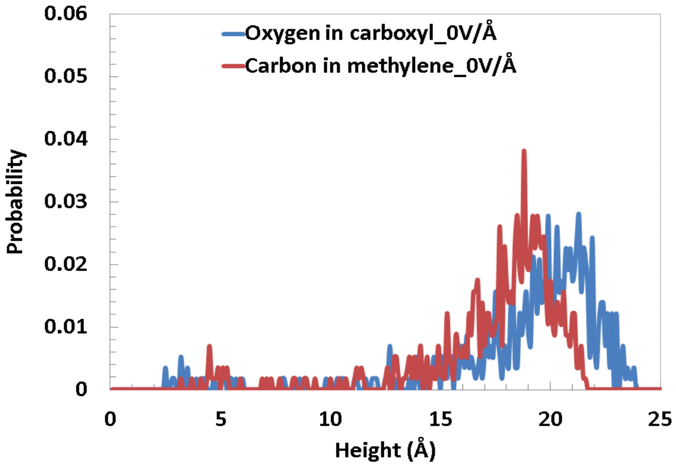

(b) Zero electrical field (0 V/Å)

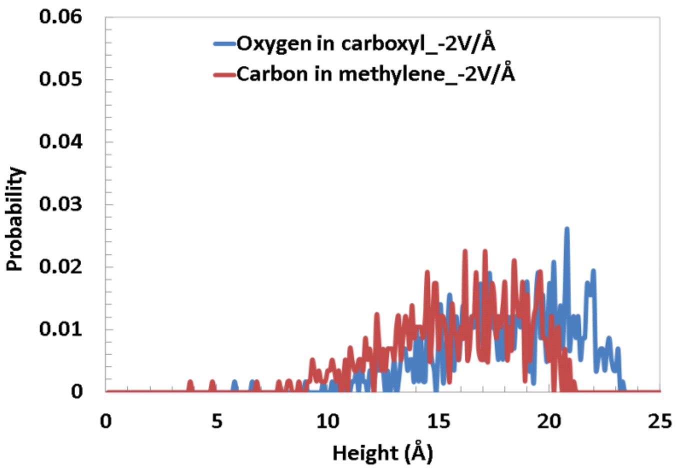

(c) Negative electrical fields (-2 V/Å)

Fig. 6-7 Comparison of oxygen and carbon height distribution

The pull-off force measurement results shown in Fig. 6-8 exhibit that the adhesion under negative electrical fields is much higher than that of positive electrical fields, which might indicate that negative electrical field keeps the SAM in a upright configuration so that the hydrophilic carboxylic eng group could interact with the hydrophilic gold-coated probe, and results in a larger adhesion force. While under positive electrical field, the SAMs are pulled down onto the substrate and expose the hydrophobic backbones to the probe, thus results in a smaller adhesion force corresponding to hydrophobic-hydrophilic interaction.

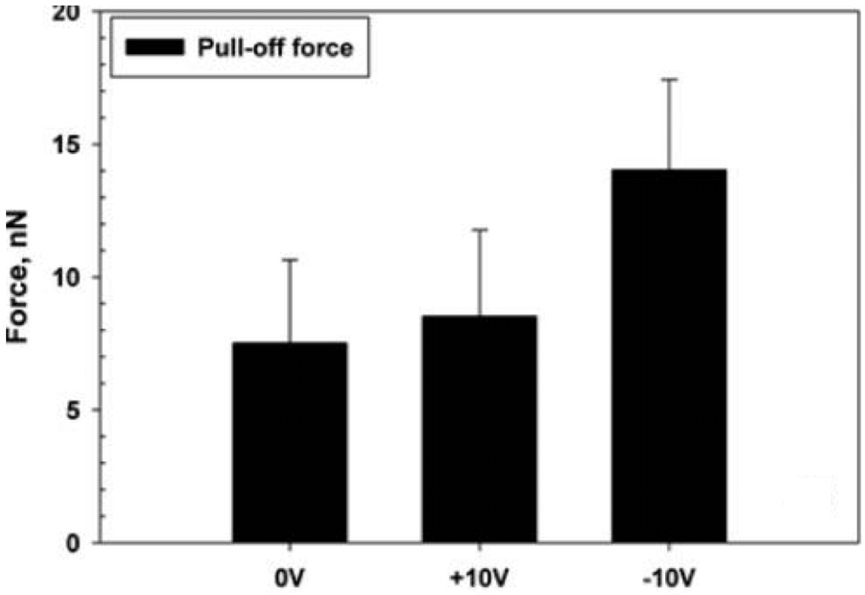

Fig. 6-8 Pull-off force measurement from AFM experiments

Another statistical result for comparing the number of carboxylic end group and the last methylene group from MD simulation in the top 6Å layer is shown in Table 6-2. It shows that the percentage of carboxylic group increased as electrical field polarity shifted from positive to negative, while that of the last methylene group decreased greatly. Such a shift demonstrates the fact that under positive electrical field, there are more methylene groups in hydrocarbon backbone chains than carboxylic end groups exposed on the top surface of the SAMs, while under negative electrical field, there are more carboxylic end groups than methylene groups in hydrocarbon backbone chains. This table can also accounts the conformational transition of MHA SAMs under different electrical fields, and has a good agreement with the adhesion measurement results from AFM experiments.

Table 6-2 Comparison of counts for carboxyl and methylene group in top 6Å

	Carboxyl		Methylene	
	Absolute counts	Percentage	Absolute counts	Percentage

2 V/Å	74	21.57%	269	78.43%
0 V/Å	429	56.23%	334	43.77%
-2 V/Å	315	65.35%	167	34.65%

As a contrary to our expectation on the friction measurements, i.e. the response of friction force as a function of applied potentials match that of adhesion force, the interesting results showed that the application of positive electrical fields led to a much higher friction force than that of zero and negative electrical fields, as shown in Fig. 6-9. The experimental results suggested that the relatively disordered structure of SAMs under positive electrical fields caused the friction force to increase, while the relatively ordered structure of SAMs under zero and negative electrical fields could maintain a lower level of friction. Hence, we postulate that the contribution from the structure order outweighs the contribution from surface chemistry, and thus governs the friction performance of SAMs under different electrical field conditions.

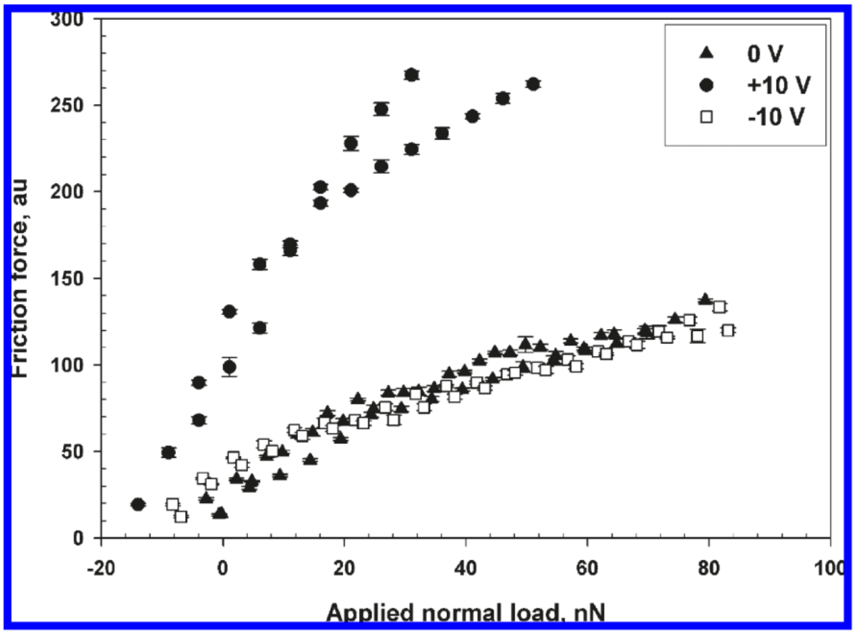

Fig. 6-9 AFM friction measurement for various applied electrical fields

From MD simulation, the 2D statistical analysis of radial distribution function (RDF) for double bond oxygen atoms in carboxylic end groups were conducted and shown in Fig.6-10, which exhibits that under all of the three electrical field conditions, RDF had peak values at 5Å. This means the chains showed clustered state and reduced the inter-chain distance from 10Å to 5Å, which is governed by the balanced distance constraint of Lenard-Jones potential well. The difference among the three cases is that the peak value of RDF reached the highest under negative electrical field, which indicates the chains were more ordered distributed at the characteristic distance 5Å. For zero electrical field, the peak value of RDF at 5Å was quite close to the negative potential case, yet showed a bit broader and scattered distribution, which might be due to the less constraint on the molecular motion since no electrical field was applied. The peak value of RDF at 5Å under positive electrical field was lowest among the three cases, which implies the chains were less ordered distributed at this characteristic distance compared to negative and zero electrical field conditions. Meanwhile we also observed that from 20Å to 30Å, the chains under positive electrical field exhibited significantly higher values of RDF than the other two potential conditions, which compensates the case that chains had the lowest RDF value at 5Å and clarifies the fact that there is more probability for SAMs to distribute at this distance region than the other two potential conditions. In summary, we may postulate that under negative and zero electrical field condition, the SAMs exhibit more extent of shorter distance order, and under positive electrical field condition, the SAMs exhibit more extent of longer distance order. Those results could provide a quantitative explanation of the implication from AFM experiments that MHA SAMs under positive electrical fields exhibit a relatively disordered structure compared to the other two potential conditions, which might be the more prominent factor that governs the change of friction response under different electrical fields.

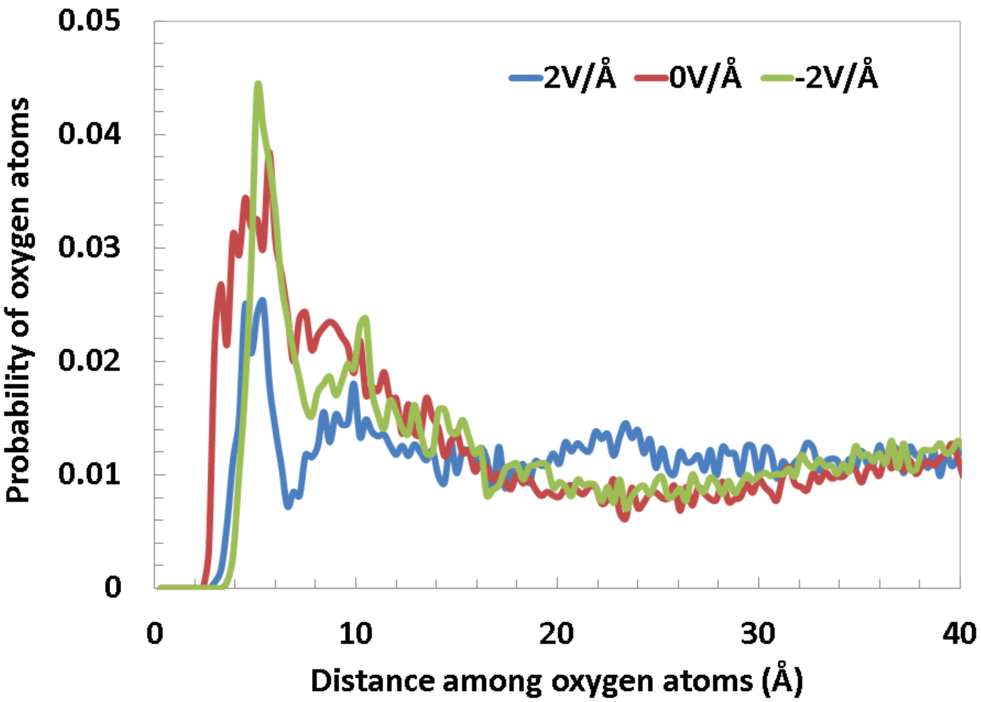

Fig. 6-10 RDF of oxygen atom distribution

Another statistical analysis of structure factor for carbon atoms in each methylene group and carboxyl end group from MD simulation could further illustrate the structural order of the backbone chains. The expression of structure factor is shown as follows.

$$S(k) = \frac{1}{N^2}\left\langle \left|\rho(\mathbf{k})\right|^2 \right\rangle \tag{6-2}$$

$$\rho(\mathbf{k}) = \sum_{i=1}^{N} \exp(-i\mathbf{k}\bullet r_i) = \sum_{i=1}^{N} \exp\left[-i(k_x r_{ix} + k_y r_{iy})\right] \tag{6-3}$$

where ρ(**k**) is the Fourier transform of the local particle density, and **k** = (k_x, k_y) is the two-dimensional scattering vector. The analysis results of structural factor under different electrical fields are shown in Fig. 6-11.

In the Fig. 6-11, number 1 to 16 denote the order of carbon atoms in methylene groups and carboxylic end group, e.g. no.1 corresponds to carbon atoms that are connected with sulfur atoms, and thus locate at the lowest height in initial configuration, while no. 16 corresponds to carbon atoms in the carboxylic end group, and thus locate at the highest height in initial configuration. We could see that under zero and negative electrical fields, carbon atoms showed apparently greater structure factor values than that under positive electrical fields for almost all methylene groups. Thus this result can also identify that under positive electrical fields, MHA SAMs show a relatively disordered structure compared with the other two potential conditions, which could be a possible explanation on friction measurement from AMF experiments.

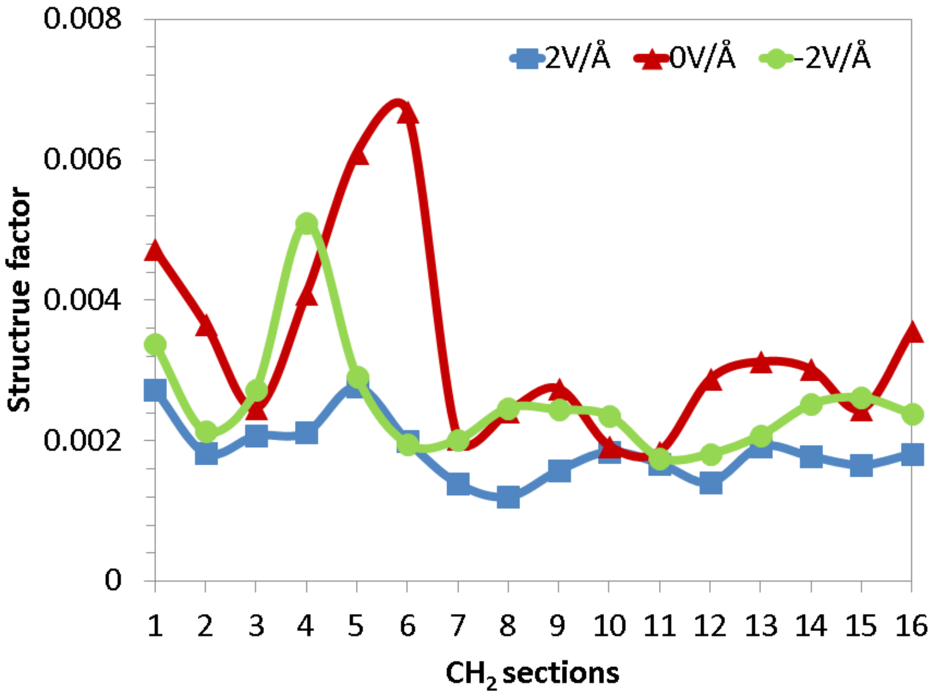

Fig. 6-11 Structure factor of carbon atoms in each methylene group

6.6 Conclusion

Combining molecular dynamics simulation and atomic force microscopy based pull-off force and friction, we are able to characterize the conformational transition and understand the mechanism that governs the friction response of MHA SAMs under the modulation of applied electrical fields, and obtain the following conclusions:

1) MD simulation shows that applied electrical field can induce conformational transition on sparse SAM films, change the surface chemistry and structural order. Under positive electrical field, MHA SAMs are pulled down onto the gold substrate, and expose the hydrophobic backbone chains on the top surface. While under negative electrical field, the chains are pushed straight up from the gold substrate, and exhibit expose the hydrophilic carboxylic end group on the top surface. The conformational transition can be verified by the AFM pull-off force experiments, in which the lower adhesion force between the SAMs and gold coated probe under positive electrical field indicates a unfavorable hydrophobic-hydrophilic interaction, and the greater adhesion force between the two under negative electrical field implies a favorable hydrophilic-hydrophilic interaction.

2) According to AFM friction measurement, the friction force under positive electrical field is much higher than those under zero and negative electrical field, and thus implies that the structural order might be a more prominent factor to influence the frictional performance than surface chemistry. The underlying mechanism behind this unexpected result could possibly explained by MD simulation, i.e. MHA SAMs under positive electrical field has less ordered structure compared with zero and negative electrical field. More specifically, positive potential induces a relatively longer distance

order upon the SAMs, while zero and negative electrical field induce a relatively shorter distance order. In this way, we may postulate that it is the structural order serving as a more dominant factor on the friction response of MHA SAMs other than surface chemistry.

CHAPTER 7. MOLECULAR DYNAMICS SIMULATION OF PEG SAM'S CONFORMATIONAL TRANSITION AND FRICTIONAL PERFORMANCE BASED ON ELECTROSTATIC STIMULATION

(A paper prepared for submission to Journal of Physics D: Applied Physics)

Xiao Ma, and Pranav Shrotriya
Department of Mechanical Engineering, Iowa State University, Ames, IA50011

7.1 Abstract

Recently self-assembled monolayer (SAM) of organic molecules such as polyethylene glycol (PEG) terminated alkanethiols have attracted considerable attention due to their unique and flexible structure upon which conformational transition can be generated under certain applied stimuli. By utilization of Molecular Dynamics (MD) simulation, the structural conformation transition of PEG terminated SAMs and corresponding frictional performance transformation based on external electrical field stimulation were investigated and reported in this research. Harmonic / class2 potentials with consideration of gold-thiol interaction as a morse potential were applied in the model to simulate the atomic and molecular interaction. Simulation results indicated that significant conformational transition of close packed PEG SAMs generated due to the electrostatic forces. Under positive electrical fields, the PEG groups were compressed and twisted into the helical form which is known as the "Gauche" conformation. While under negative electrical fields, the PEG groups were stretched into the straight form which is known as the “All-trans” conformation. Such conformational transition could induce substantial transformation of frictional performance upon PEG SAMs. Interaction between the SAMs with a repulsive indenter upon penetration and sliding showed that under positive electrical field, “Gauche” conformation decrease the inter-chain space for deformation, thus led to a comparatively lower frictional coefficient; while under negative electrical field, “All-trans” conformation increased inter-chain space for deformation, thus generated a higher frictional coefficient. During the simulation of interaction of SAMs with indenter, two kinds of frictional phase were observed. Under shallow indentation and sliding, a lower level of frictional coefficient was obtained and the configuration integrity of the molecular chains was not influenced by the indenter. While under deep indentation and sliding, much higher loads caused a greater level of frictional coefficient and the backbone chains can be dragged along with the indenter away from their original locations. The Molecular Dynamics simulation in this research provides meaningful insights upon the structural transition and tribological performance transformation of the PEG SAMs based on electrostatic stimulation.

Keywords Molecular Dynamics Simulation Self-Assembled Monolayer
conformational transition tribological performance
electrostatic stimulation

7.2 Introduction

Self-Assembled Monolayer has received enormous attention as a feasible means to control physical and chemical properties of solid surfaces (Lahann, Mitragotri et al. 2003), thus has remarkable potentials in microfabrication (Ulman 1990; Jackman, Wilbur et al. 1995; Wilbur, Kumar et al. 1996; Azzaroni, Schilardi et al. 2003; Liu and Cui 2005), microelectronics (Schon, Meng et al. 2001; Schon, Meng et al. 2001; Fan, Yang et al. 2002; Stapleton, Harder et al. 2003; Fan, Yao et al. 2004), tribology (Srinivasan, Houston et al. 1998; Maboudian, Ashurst et al. 2000; Sundararajan and Bhushan 2001), and biological applications (Kane, Takayama et al. 1999; Zhao, Wang et al. 2011). There are several means to induce conformational transition upon SAMs so as to change surface properties through applications of external stimuli, such as temperature (Ghorai and Glotzer 2007), pH of solvent (Osnis, Sukenik et al. 2012), applied electrical fields (Vemparala, Kalia et al. 2004; Pei and Ma 2005), electrochemical modifications (Willner 2005) and side-chain substitution (Gus'kova, Mena-Osteritz et al. 2007).

Among different external stimuli to induce conformational transition, applied electrical field is a feasible, scalable and controllable method without any detrimental influence on the chemical stability of SAM. Vemparala et al. (Vemparala, Kalia et al. 2004) examined the electrical field induced conformational transition of polyethylene glycol (PEG) terminated SAMs with high coverage density on gold substrate by using molecular dynamics (MD) simulation. Due to the polar nature of glycol groups, the electrical field triggered the conformational transition from “all-trans” state to “gauche” state. The antiparallel electrical field with respect to the surface normal caused a reversible transition and ordered distribution of chains, whereas the parallel electrical field with respect to the surface normal introduced a large extent of disorder upon the SAMs. Pei et al. (Pei and Ma 2005) applied MD simulation to study the electrical field induced surface-switching behaviors of mixed ω-carboxyalkyl/alkyl SAMs deposited on H-Si(111) surfaces with low coverage density. They identified the reversibly conformation transition between the all-trans state and mixed gauche-trans state induced by the applied electrical fields ranging from -0.2 V/Å to 0.7 V/Å. They also showed that the surface switching behavior could be facilitated by lowering the ionic strength and additions of acetonitrile molecules in the surrounding solution, since the threshold intensity of the electric field required for triggering the surface swithcing was substantially decreased. Karuppiah et al.(Karuppiah, Zhou et al. 2009) utilized atomic force microscope (AFM) to evaluate the adhesion and friction response of a low-density mercaptocarboxylic acid (MHA) SAM under electrical field modulation with different polarities. They discovered higher adhesion force when negative electrical fields were applied upon the SAMs, and attributed this performance alteration to surface chemistry transition. The surface friction showed a contrary trend that higher friction level was obtained when positive electrical fields were applied. They explained this phenomenon in terms of structural order of the thin film, i.e. the higher friction under positive bias is ascribed to the relatively disordered structure of the SAMs, whereas the relatively ordered structure under negative bias tends to decrease the friction.

Several research groups have applied MD simulation to study the conformational transition and its influence on frictional behavior of SAMs. Harrison et al.(Brenner, Harrison et al. 1991; Harrison, White et al. 1992; Harrison, White et al. 1995; Harrison, Tutein et al. 1999; Harrison 2001; Mikulski and Harrison 2001; Harrison, Schall et al. 2008) introduced an AIREBO potential to simulate structural and tribological properties of hydrocarbon SAMs using various nanostructures as the indentation and sliding counterfaces, such as carbon nanotubes, diamond surfaces, amorphous carbon surfaces and fullerenes. They compared odd number carbon (C_{13}) with even number carbon (C_{14}) system which differs in the orientation of the last carbon–carbon bond. The analysis of probability distribution of methyl angle shows that the odd system has a comparatively larger deformation and shift, and more gauche defects than the even system. More detailed sliding-direction force distribution showed that the odd system contains more atoms that are capable of generating small pushing and resisting forces than even systems. They also identified that the comparatively flexible hydrocarbon SAMs significantly reduce the mechanical excitation of the interface lattice layers upon sliding, thus can decrease the friction effectively. Chandross et al. (Chandross, Webb et al. 2004; Chandross, Lorenz et al. 2005) conducted MD simulation to investigate the adhesion and friction between ordered and disordered SAMs on silicon dioxide substrate. They created the disorder upon SAMs by removal of randomly selected chains from the ordered crystalline substrate, and then deposited chains onto an amorphous substrate. They observed stick-slip motion in full coverage ordered SAMs in terms of relatively slow shear velocities and constant pressures on the SAMs, while it disappeared in disordered one. The friction coefficient of the disordered SAMs was found to be not sensitive to the coverage density, chain length and substrate compared with the full coverage ordered SAMs. Kapila et al.(Kapila, Deymier et al. 2006) studied the friction between alkylsilane SAMs attached to two rigid silica substrates. They investigated friction coefficient, friction force and normal load as a function of separation between substrates, temperature of films and sliding velocity of substrates. Their results showed that the frictional behavior of films as a function of separation between substrates follows the thermal activation model proposed by Briscoe and Evans (Briscoe and Evans 1982), while the normal loads on the films depends on the temperature of films and sliding velocity of substrates. Tupper et al. (Tupper and Brenner 1994) performed MD simulation to study the friction of the relative sliding between two alkanethiol SAMs, and found the friction force is proportional to the applied load. They also discovered the chain length and the applied load did have effect on the SAM structure but didn't influence the frictional property very much. Wu et al. (Wu, Lin et al. 2007; Wu, Fang et al. 2013) used MD simulation to study the friction mechanisms of n-hexadecanethiol SAM adsored on a gold substrate and scratched by a gold slider in terms of sliding height, direction, velocity and temperature. They discovered the amplitude of the stick-slip action cycle increases with the lower sliding height until reaching a critical value. Below the critical sliding height the there is irreversible changes in SAM organization and loss of lubricating efficiency. They also found a significantly lower friction level for the anti-tilt sliding above the critical height, and which is inverted below the critical height. Chang et al. (Chang, Fang et al. 2009) investigated the nanoscratched mechanisms of alkanethiol SAM on a gold substrate using MD simulation under different nanoscratched depths, the workpiece temperatures, the scratched speed, the SAM chain lengths and the shapes of the indentors. They discovered that the disorder, plastic mobility and friction coefficient of the SAM increased with a larger nanoscratched depth. The friction coefficient is found to be increased with a larger scratched speed. Longer chain length lead to larger tilt and bending, and a spherical indenter causes higher reaction forces than a Vickers indenter. Ramin et al. (Ramin and Jabbarzadeh 2011) applied MD simulation to investigate the tribological behavior of dodecanethiol SAM on Au(111) surfaces via different loading and shear rate conditions. They discovered that when loading is lower than 700MPa, the fluctuations of the SAM is quite small. Above this loading the SAM backbone chain starts to compress and film thickness is significantly decreased. When loading is higher than 5GPa, the SAM undergoes disorganization and finally crushes. They also found the friction coefficient increases by enhancing the shear rate. Hu et al. (Hu, Zhang et al. 2006) applied MD simulation to investigate the atomic friction between SAM on Au(111) surfaces with emphasis on the performances of commensurate and incommensurate SAM in relative sliding. They found a clean periodic stick-slip friction pattern on commensurate SAMs, while random fluctuation and lower shear stress on incommensurate SAMs. They always found a higher friction forces on commensurate SAMS than those on incommensurate SAMs. The linear dependence of shear stress on normal pressure and logarithmic dependence on sliding velocity were also characterized. Sung et al. (Sung and Kim 2005) utilized MD simulation to understand the nano-tribological phenomena of the nano-metric scribing process between the alkanethiol SAMs with probe tip. They found the SAM molecules were displaced and dragged by the probe tip during the scribing process, and the scribed pattern width was largely dependent on the probe shape other than tip-sruface contact size. They also showed that high-speed scribing results in excessive removal of the SAM molecules from the surface. Bonner et al. (Bonner and Baratoff 1997) applied MD simulation to study the interaction between scanning force microscopy (SFM) with alkanethiol SAMs on gold substrate by modeling the probe of SFM as a deformable pyramidal cluster connected by orthogonal springs to a rigid support. When penetration increased, they found the sliding caused stick-slip friction response, and the contact region of SAM tilted collectively towards the scan direction. They also discovered the defects shown in the SAM when the drag was beyond a critical load.

In summary, applied electrical fields can induce substantial conformational transition upon SAMs with polar end group that has non-concentric charge distributio. Simulation results show that the orientation of bonds in end groups, crystallographic directions, tilt angle and stick-slip motion could be largely influenced by penetration depth, sliding velocity, temperature and indenter shape, and thus leads to distinctive friction responses of various SAMs.

In this paper, MD simulation is conducted to investigate the conformational transition induced by applied electrical fields on close packed PEG SAM. Associated transformation upon frictional performance of PEG SAM is investigated as a function of the applied electrical fields, normal loads and indenter shape.

7.3 Method

7.3.1 Initial ensemble and interatomic potentials

Molecular dynamics (MD) was utilized to calculate the trajectory of all atoms on PEG SAM under applied electrical fields through numerical integration of Newton’s equations of motion via an open source shared parallel code - LAMMPS (http://lammps.sandia.gov) (Plimpton 1995), then associated conformational transition and friction response could be computed through post-processing of the above data file.

In order to generate the initial ensemble, 576 chains of polyethylene glycol (PEG) terminated SAM ($S\text{-}(CH_2)_{13}\text{-}(O\text{-}CH_2\text{-}CH_2)_3\text{-}O\text{-}CH_3$) were located on fixed Au(1 1 1) plane with the (√3 × √3) R30° lattice structure and a approximate 30° initial tilt angle with respect to the normal vector (Zhang, Goddard et al. 2002; Zhang and Jiang 2002). At full coverage density, the interchain spacing is 5Å which is determined by the lattice structure. The 2D initial configuration of the SAMs and the direction of applied potentials are shown in Fig. 7-1.

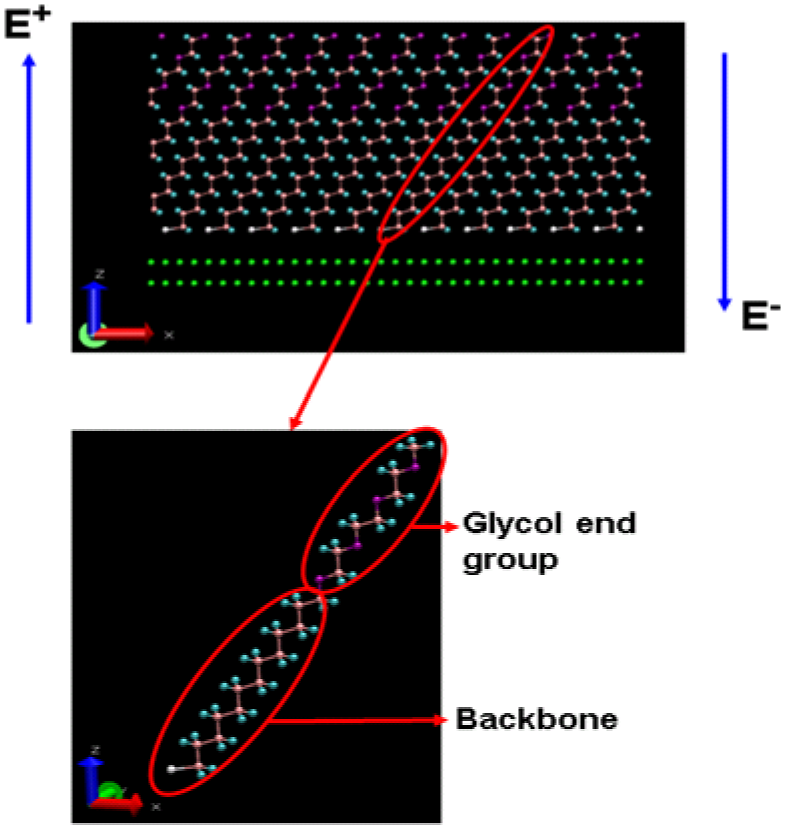

Fig. 7-1 Initial configuration of PEG SAMs

[color representation: gold (green), sulfur (white), carbon (pink), hydrogen (cyan) and oxygen (purple)]

The interatomic potentials for modeling the SAMs were divided into three parts: bonded, nonbonded and external electrical field terms, as shown in the following equation.

$$V = V_{bonded} + V_{nonbonded} + V_{electrical\ field} = \\ (V_{bond} + V_{angle} + V_{dihedral}) + (V_{lennard\ jones} + V_{coulombic} + V_{morse}) + V_{electrical\ field} \tag{7-1}$$

The covalent bonds in PEG SAMs were simulated via CHARMM / class2 molecular potentials ((Brooks, Bruccoleri et al. 1983; Jaffe, Smith et al. 1993; Smith, Jaffe et al. 1993; Tasaki 1996; Tasaki 1996). More specifically, CHARMM potential was applied to simulate bond (stretching) and angle (bending) interactions, and class2 potential was used to simulate dihedral (torsion) interaction. The bonds between sulfur and gold atoms were simulated via Morse potential (Pertsin and Grunze 1994; Zhang, Goddard et al. 2002). Lennard Jones (LJ) potential was used to simulate interactions among atoms of PEG SAM other than bonded and morse potiential interactions (Sorensen, Liau et al. 1988; Rappe, Casewit et al. 1992). Those intramolecular and intermolecular potential function parameters have been previously reported to accurately capture the equilibrium conformations, excess enthalpies, and vibrational frequencies of the molecular systems (Lifson and Warshel 1968; Engler, Andose et al. 1973). Point charges were only assigned on the atoms in the glycol end group following the Mulliken charge analysis (Mulliken 1955; Mulliken 1955; Mulliken 1955; Mulliken 1955). The long-range electrostatic pair interactions between charged atoms were computed using Ewald summation routines which are available in LAMMPS.

7.3.2 Procedure for conformation simulation

In order to investigate conformational transition of PEG SAM under electrical field stimulation, MD simulation was conducted with a 1fs time step in three steps: initialization, thermalization and electrical field application. For the initialization, a temperature of 0.45K was assigned to the system for 20ps with NVT ensemble to minimize the initial energy of the random vibration. Then the temperature was raised to 200K on the SAMs for thermalization with NVT ensemble until the system reached equilibrium. After that, applied electrical fields were exerted onto the SAMs with NVE ensemble until the system achieved equilibrium. The simulations were repeated for different electrical field strengths ranging from 2V/Å to -2V/Å with an increment of -0.5V/Å. After equilibrium, MD simulations were continued for a period of 60ps to apply statistical analysis.

7.3.3 Procedure for indentation and sliding simulation

The schematic Fig. 7-2 shows the indentation and sliding process. In order to consider the influence of indenter shape, two geometries, i.e. cylindrical and spherical indenters were adopted in the simulation. The indenters were modeled as a rigid and repulsive surface with the following potential functions (Kelchner, Plimpton et al. 1998; Shimizu, Eda et al. 1998; Ohzono and Fujihira 2000).

$$F(r) = -k(r-R)^2 H(R-r) \tag{7-2}$$

where r is the distance between the indented SAM atoms and the center of the indenter, R is indenter radius and k is the stiffness constant of indenter surface. The value of R is set to 25 Å such that rigid indenter surface makes contact with multiple chains during the indentation and sliding simulations. The value of k is set to 70 nN/Å^2 such that the SAM atoms do not penetrate the indenter surface. H is a Heaviside step function to ensure that only the atoms in contact with indenter surface are subjected to repulsive force.

Based on different conformational states under corresponding electrical fields, indentation and sliding simulation can be performed consecutively. There are three steps in this simulation: indentation, dwelling and sliding. For the indentation, the indenter was moved downwards at a velocity of 0.25Å/ps and brought into contact with PEG SAMs to achieve desired load level with NVE ensemble. Then the indentor was kept stationary with NVE ensemble until the contact load achieved a steady value. After that the indenter was maintained at a constant height and moved forward at a velocity of 1Å/ps along the contact surface of the SAMs for 100ps with NVE ensemble. In order to examine the influence of applied potentials and SAM deformation on friction performance, simulations were conducted for a range of indentation loads and different potential levels at 2 V/Å, 0 V/Å and -2 V/Å.

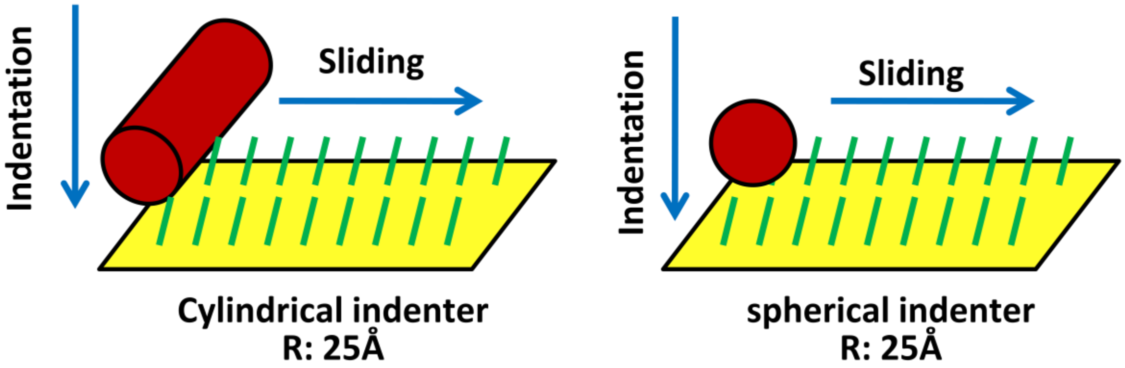

Fig. 7-2 Scheme of indentation and sliding simulation

7.4 Results

7.4.1 Conformation simulation

The total energy output of the system for a typical conformation simulation is shown in Fig. 7-3. The system was first kept at 0.45 K to reach energy minimization within 20 ps. When the temperature was raised to 200 K, the total energy increased as the kinetic energy was enhanced, and within 20 ps the SAMs could achieve equilibrium state. Then applying an electrical field onto the system increased the potential energy, and thus also increased the total energy of the SAMs, and the system reached equilibrium within 20 ps. The simulation was continued for 40 ps to compute statistical results.

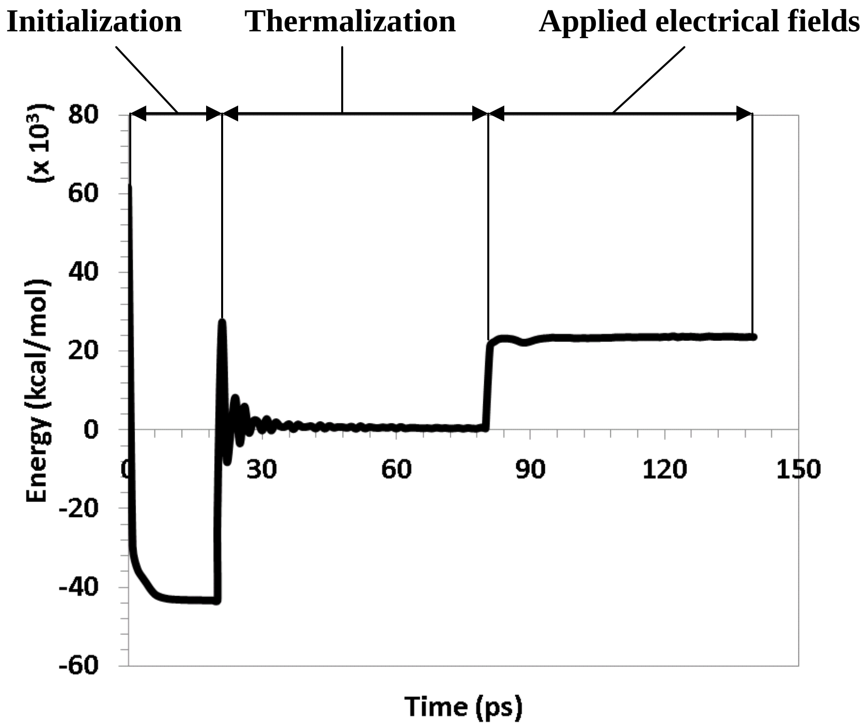

Fig. 7-3 Energy output for conformation simulation

The representative configurations of individual PEG chains after applying electrical field are shown in Fig. 7-4. It can be qualitatively observed that the backbone chain was kept standing-up configuration under zero potential, and was pushed up under both of the positive and negative electrical field with a smaller tilt angle. The glycol end group was heavily twisted and showed a "gauche" conformation under positive electrical fields, whereas it was stretched straight and showed an "all-trans" conformation under negative electrical fields.

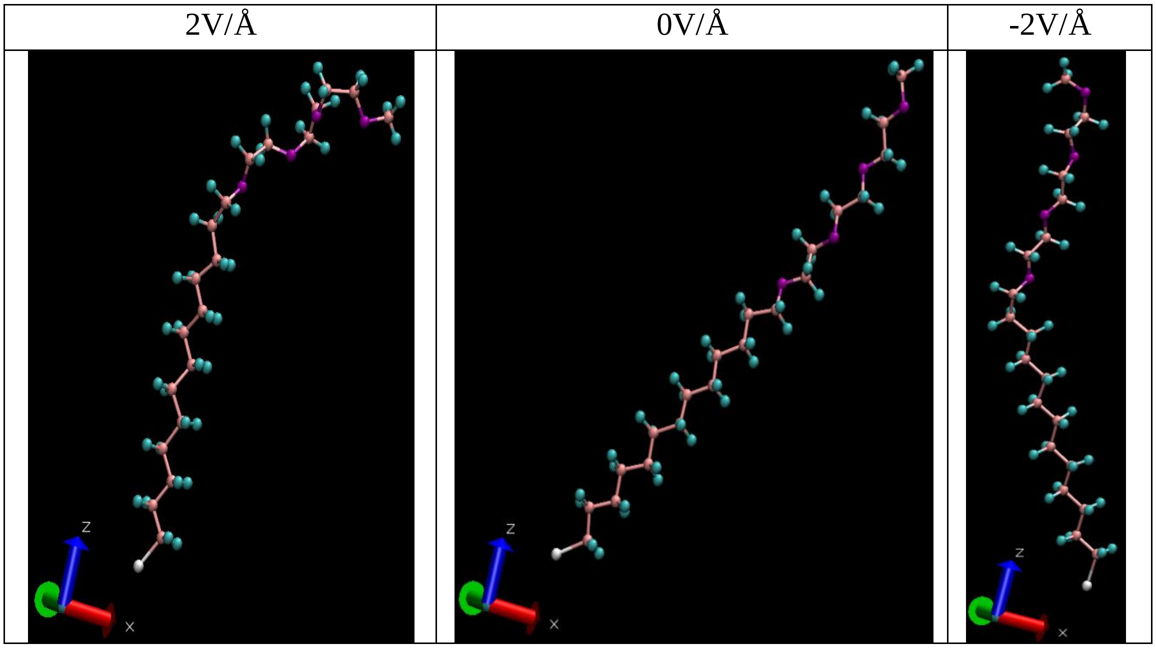

Fig. 7-4 Representative configuration snapshot of individual PEG chains after applying electrical fields

[color representation: sulfur (white), carbon (pink), hydrogen (cyan) and oxygen (purple)]

By extracting the top layer with a thickness of 6Å, the typical configuration and structural transition of PEG SAM surface corresponding to the application of electrical fields are shown in Fig. 7-5. Because of the electrostatic interaction exerted on charged atoms in glycol end group, the negative charged oxygen atoms were buried inside under positive electrical fields, whereas they were exposed outside under negative electrical fields. It can be also found that because of the twisting effect on glycol end group under positive electrical fields, some chains fell off the top layer.

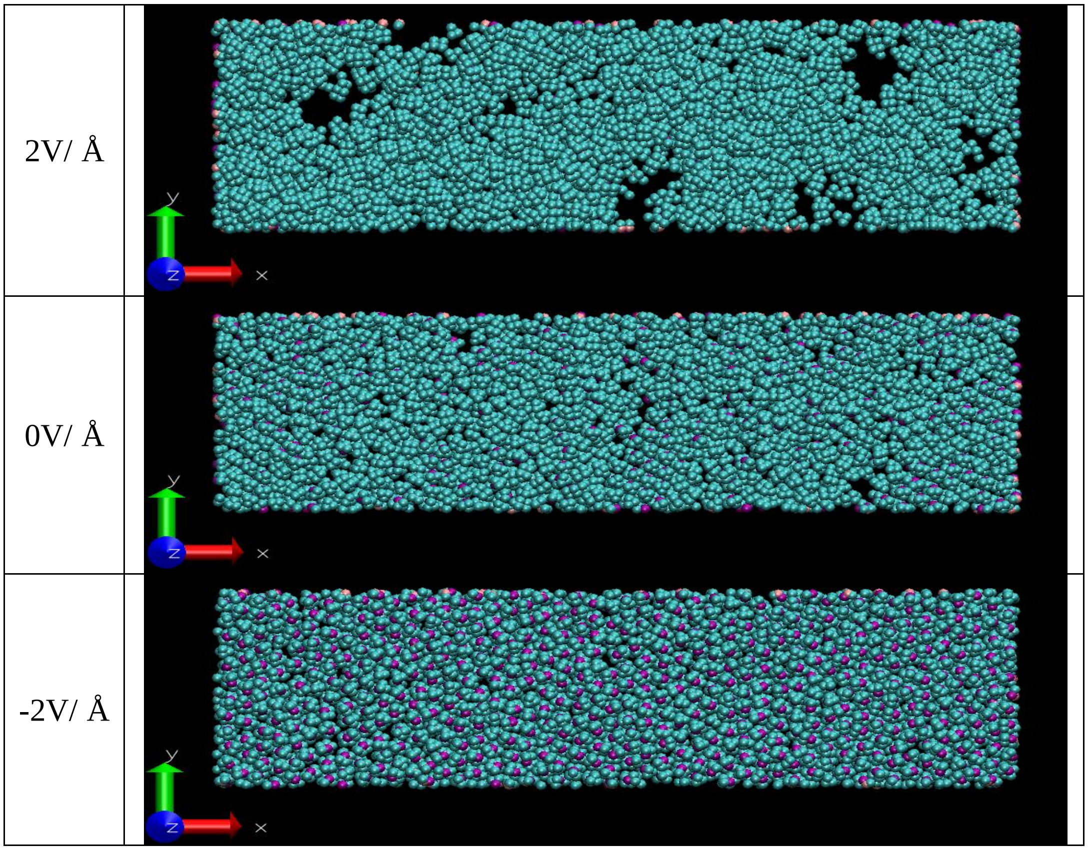

Fig. 7-5 Top view of typical configuration of PEG SAMs after applying electrical fields [color representation: carbon (pink), hydrogen (cyan) and oxygen (purple)]

The orientation of the backbone chains can be exhibited quantitatively through the average tilt angle calculation, which is defined as the angle between backbone chains and surface normal, as shown in Fig. 7-6. It should be noticed that ±1.5V/Å were likely to be the threshold values of tilt angle that at those potential intensities the backbone chain of PEG SAMs were raised up sharply. However, considering the configuration of the glycol end group shown in Fig. 7-4, we could postulate different raising-up mechanisms upon the backbone chains. Under positive electrical fields, the glycol end groups were greatly twisted in a helix "gauche" conformation, which was quite space consuming, and thus the stronger interchain molecular interactions caused the larger repulsive forces to decrease the tilt angle of backbone chains. While under negative electrical fields, the electrostatic force exerted on the glycol end groups directly stretched the chains, and thus decreased the tilt angle of backbone chains.

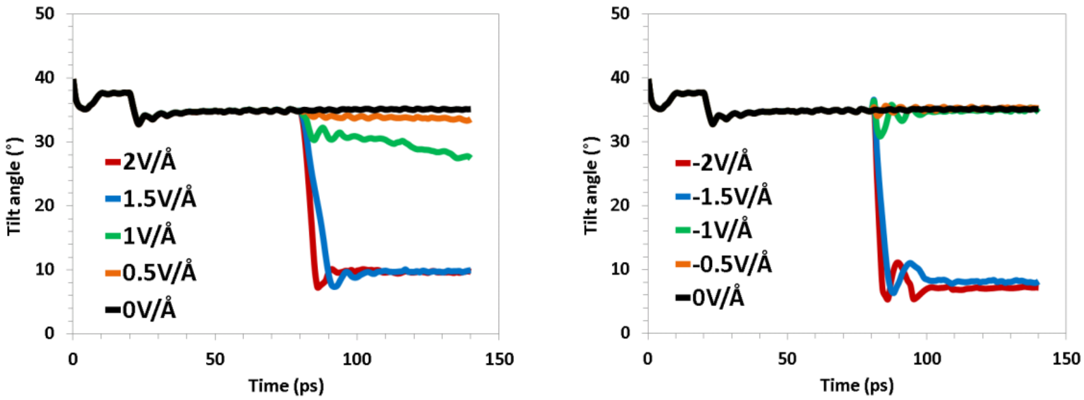

(a) Positive electrical fields

(b) Negative electrical fields

Fig. 7-6 Tilt angle calculation of PEG backbone chains

Another analysis of two dimensional structure factor on all of the carbon atoms in backbone chain and glycol end group could provide useful information on the order of the whole chains. The expression of structure factor is shown in the following equations.

$$S(k) = \frac{1}{N^2}\left\langle \left|\rho(\mathbf{k})\right|^2 \right\rangle \tag{7-3}$$

$$\rho(\mathbf{k}) = \sum_{i=1}^{N} \exp(-i\mathbf{k}\bullet r_i) = \sum_{i=1}^{N} \exp\left[-i(k_x r_{ix} + k_y r_{iy})\right] \tag{7-4}$$

where $\rho(\mathbf{k})$ is the Fourier transform of the local particle density, and $\mathbf{k} = (k_x, k_y)$ is the two-dimensional scattering vector. The plots of structural factor under different electrical fields are shown in Fig. 7-7. No. 1 to 20 on horizontal axis denote the numbering of carbon atoms in methylene groups and glycol end group, e.g. no.1 corresponds to carbon atoms that are connected with sulfur atoms, i.e. locate at the lowest height of 20 carbon atoms in a chain for the initial configuration, while no. 20 corresponds to the last carbon atoms in the glycol end group, i.e. locate at the highest height of 20 carbon atoms in a chain for initial configuration. It is observed that for both positive and negative electrical fields applied, structure factors of the SAMs are decreased, i.e. the applied potentials induce disorder into the system. Meanwhile, we should also notice that by comparison of the extreme positive potential strength 2V/Å and the extreme positive potential strength -2V/Å, the former one has a much lower structure factor than the latter, which implies that positive electrical fields induce much more extent of disorder upon the SAMs, or we may conclude that there is more prominent conformational transitional of the whole chain under positive electrical fields.

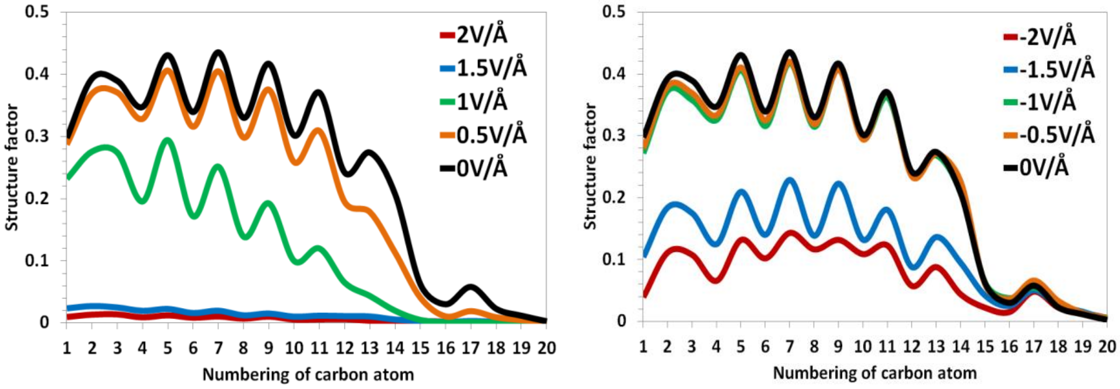

(a) Positive electrical fields

(b) Negative electrical fields

Fig. 7-7 2D structure factor of PEG backbone chains

The conformational transition of the glycol end groups can be shown quantitatively through the computation of partial radial distribution function (RDF) of OCCO dihedral group, which is defined as the number density of oxygen atoms with respect to the radial distance among different oxygen atoms, as shown in Fig. 7-8. There are two previously reported parameter sets of dihedral interaction potential, i.e. from Yoon's group (Jaffe, Smith et al. 1993; Smith, Jaffe et al. 1993) and from Tasaki"s group (Tasaki 1996; Tasaki 1996), and we utilized those two parameter sets respectively in the MD simulation in order to examine their computational efficiency. Based on Yoon's potential parameter sets, the above conformational transition can be explicitly illustrated in Fig. 7-8(i). The RDF of OCCO dihedral group has two significant peak values at 2.7Å corresponding to "gauche" conformation, and 3.5Å corresponding to "all-trans" conformation. When positive electrical fields were applied to the PEG system with increasing field strength, the peaks at 2.7Å increased whereas the peaks at 3.5Å decreased gradually, this implied that positive electrical fields triggered the "gauche" conformational transition upon glycol end groups. On the other aspect, when negative electrical fields were applied with increasing field strength, especially lower than -1V/Å, there were even no any peaks at 2.7Å, whereas the peaks at 3.5Å increased further, which indicated that negative electrical fields triggered the "all-trans" conformational transition by stretching the glycol end groups straight up.

Based on Tasaki's potential parameter sets, the RDF of OCCO dihedral group is shown in Fig. 7-8(ii), under positive electrical fields with increasing field strength, there was certain amount decrease of "all-trans" peaks at 3.5Å, but no significant variation of "gauche" peaks at 2.7Å was found. Under negative electrical fields with increasing field strength, there was certain amount decrease of "gauche" peaks at 2.7Å and increase of "all-trans" peaks at 3.5Å, but some other peaks at 3Å also emerged with ambiguity. In addition, the relative values of the RDF peaks based on Yoon's parameter sets were always prominent than that based on Tasaki's parameter set. Therefore, the comparison of two parameter sets showed that Yoon's potential parameter set is a better selection with higher computational efficiency for simulating the torsion and twist behavior upon glycol end group than Tasaki's.

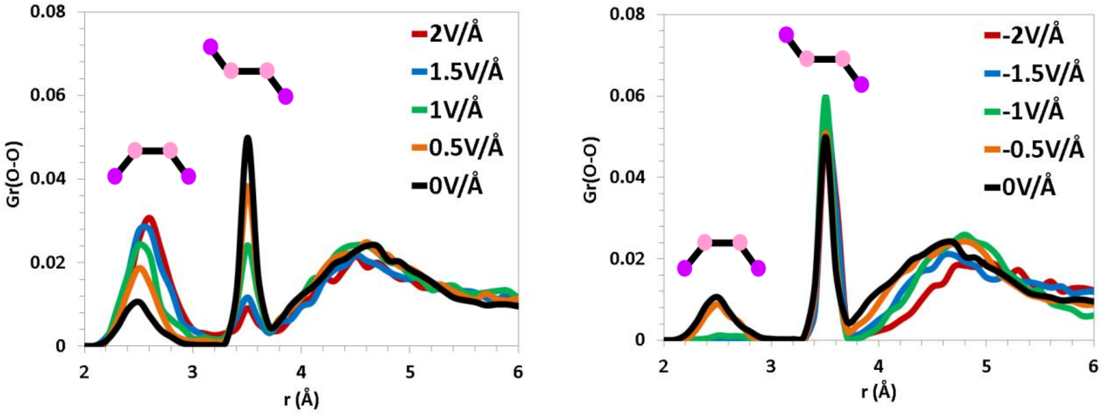

(a) Positive electrical fields (b) Negative electrical fields

i) Yoon's potential parameter sets

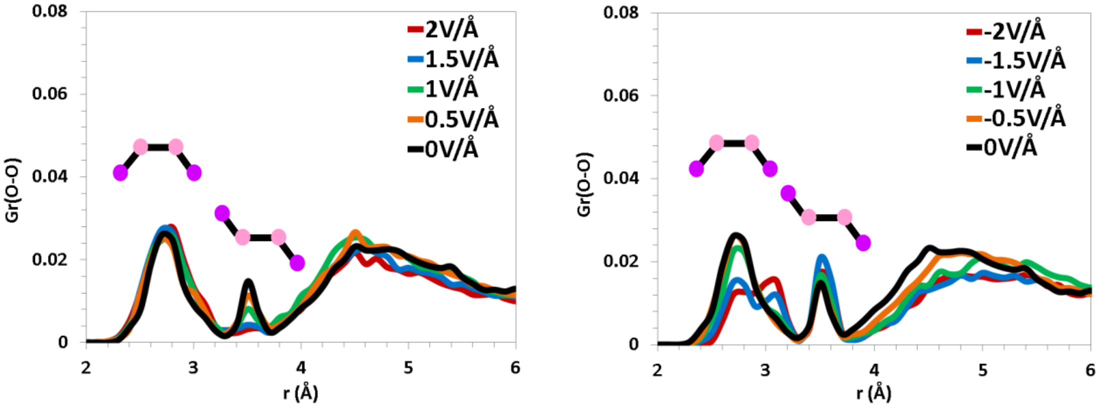

(a) Positive electrical fields (b) Negative electrical fields

ii) Tasaki's potential parameter sets

Fig. 7-8 RDF calculation of OCCO dihedral groups

[color representation for inlet: carbon (pink), oxygen (purple), covalent bond (black)]

The dihedral potential energy output also supports such conformational transition under electrical fields, as shown in Table 7-1. Under positive electrical fields, there was enormous increase of dihedral potential energy, which implies the "gauche" conformational transition was generated to a large extent. While under zero and negative electrical fields, there was subtle change of dihedral potential energy (even slight decrease in negative potential case), which indicated instead of "gauche" conformation, "all-trans" conformation was dominant.

Table 7-1 The ratio of dihedral potential change before and after application of electrical fields

Dihedral potential change	2V/Å	0V/Å	-2V/Å
$(E_{dihe\_efield} - E_{dihe\_thermo}) / E_{dihe\_thermo}$	157%	3.61%	-1.69%

To understand this "all-trans" to "gauche" conformational transition on the whole chain, the analysis of the normal density profile is conducted and shown in Fig. 7-9, which compute the number distribution of atoms along the surface normal direction. Under zero potential, we observed a doublet pattern upon the normal density profile, while indicated that the SAMs were in the "all-trans" conformation, since C-C bond held an alternate sequence of two orientations, i.e. along the surface normal and oriented approximately 60 ° with respect to surface normal. When positive potentials were applied on the SAMs and reached 1.5V/Å, the doublet pattern totally disappeared, which indicated that the "all-trans" conformation on the backbone chain has also been greatly altered. While for negative electrical fields, the doublet pattern could be kept well until -1V/Å, and gradually destroyed at -1.5V/Å and -2V/Å, however we could still observe some vague or residual doublet pattern under those two potential intensities. Through the comparison of normal density profiles under positive and negative electrical fields, we could draw the conclusion that positive potentials can totally alter the “all-trans” conformation on the whole SAM chain, while negative potentials have limited impact on this alteration.

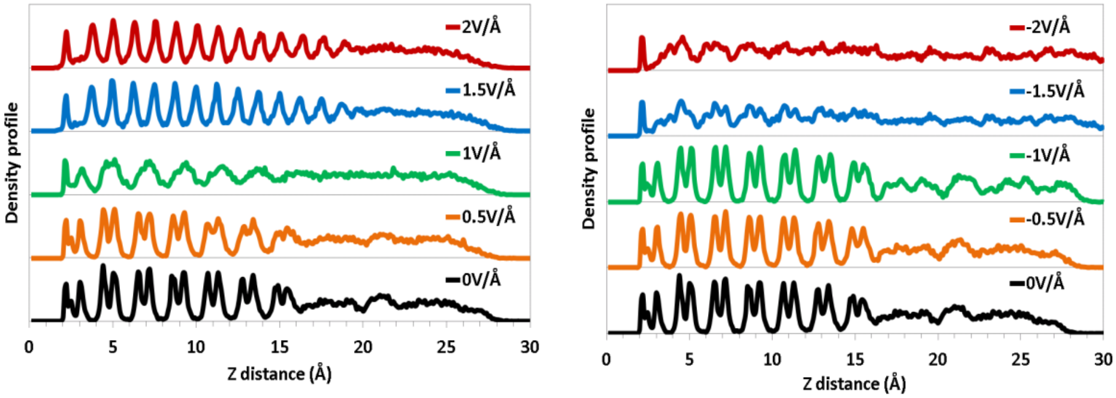

Fig. 7-9 Normal density profile of the whole SAM chain

7.4.2 Friction simulation

The indentation load exerted by the cylindrical rigid indenter is plotted as a function of normalized indentation depth in Fig 10. Normalized indentation depth, d, is defined as follows

$$d = \frac{h_0 - h}{h_0} \qquad 0 < h < h_0 \tag{7-5}$$

where h is the height with respect to the gold substrate (the same as z distance in Fig.9), and h_0 is the initial height of the indenter with respect to to the gold substrate. The initial height for all simulations was maintained to be about 10 Å above the highest atoms in the SAM.

Different indentation depths correspond to different normal load levels, so typical indentation loads were chosen on the indentation load-displacement curve to initiate sliding simulation, as the red forks shown in Fig. 7-10. We observed that the indentation load show two phase along the increase of indentation depth. After the contact of the indenter and the top surface of the SAMs, indentation load just increased gradually, which implies that indenter had a normal interaction with the SAM chains. When the indentation depth reached a threshold (around 0.82), there is a short plateau, which indicates that the indenter was quite deep in the SAMs and repulsed the around chains too much so that the contact load didn't increase accordingly. After this plateau, we observed a abrupt increase of the indentation load that means the indenter even interacted with fixed gold substrate, so the indentation load was extremely large. For comparison, we choose the same indentation depth from spherical indenter as that from cylindrical indenter.

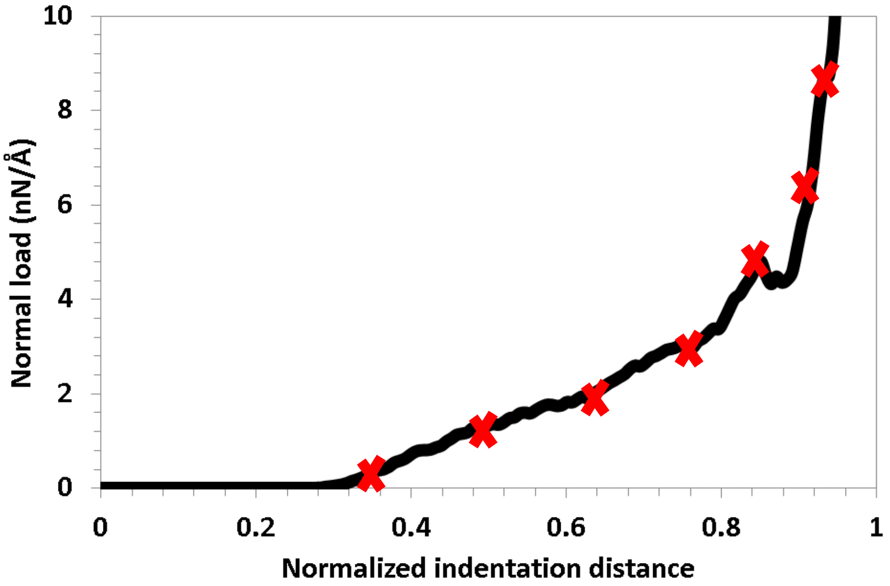

Fig. 7-10 Selection of indentation load on load-displacement curve

During the sliding, normal and tangential loads were computed to determine the frictional coefficients. The frictional coefficients of both cylindrical and spherical indenter on PEG SAMs were shown in Fig. 7-11. The scale of frictional coefficients is comparable to the nano scale friction simulation on alkyl monolayers and other organic monolayers (Harrison, White et al. 1992; Harrison, White et al. 1995; Zhang and Jiang 2002; Kapila, Deymier et al. 2006; Harrison, Schall et al. 2008).

There were two stages of friction response upon PEG SAMs during the sliding with different normal loads. On the lower normal load level (corresponding to the first 5 indentation depths shown in Fig. 7-10) , the frictional coefficients kept increasing with along the increment of normal load, which was also observed from reports for the frictional response of other close packed SAMs (Harrison, White et al. 1992; Harrison, White et al. 1995). It should be prominently noticed that under zero and negative electrical fields larger frictional coefficients were achieved than positive electrical fields. This may be caused by the fact that positive electrical fields induced “gauche” conformational transition onto PEG SAMs, i.e. chains were twisted into a coil-like configuration, so there was little interchain space for the SAMs to generate large deformation. While under zero and negative electrical fields, chains were held in “all-trans” conformation, i.e. a stick-like configuration of the SAMs, thus had more room to generate large stick-slip motion and deformation, and induce more resistance and energy absorption during the indenter sliding process. (corresponding to the last 2 indentation depths shown in Fig. 7-10) However, since in our simulation the gold atoms in substrate were fixed, i.e., the deformation of the gold substrate was not simulated, so under those higher normal load levels, the simulation might lead to non-physical response. Therefore, only the frictional coefficient results under lower normal load levels should be considered as reasonable responses. It can also be pointed out that no matter the shape of indenter as cylinder or sphere, similar trends on friction response were observed.

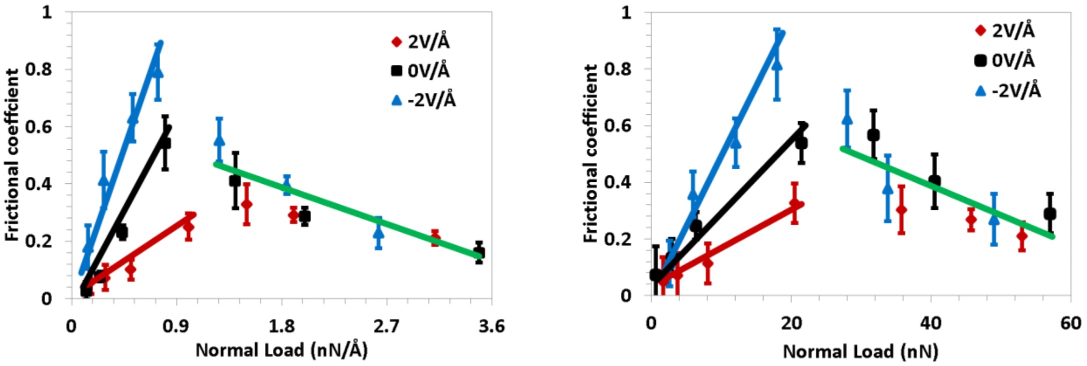

a) Cylindrical indenter (b) Spherical indenter

Fig. 7-11 Frictional coefficients of closed packed PEG SAMs

The total bonded energy output could provide the evidence of the above postulated mechanism of frictional performance change under electrical fields, as shown in Table 7-2. From positive potential of 2V/Å, to zero potential, and to negative potential -2V/Å, we observe a significant increase of changes in energy associated with bond, angle and dihedral potentials, i.e. total bonded energy, which could explain the reason why there is prominent increase of frictional coefficient under negative electrical fields than positive electrical fields.

Table 7-2 The ratio of bonded energy change before and after indentation and sliding

Total bonded energy change	2V/Å	0V/Å	-2V/Å
$(E_{bonded\_after} - E_{bonded\_before}) / E_{bonded\_before}$	22.3%	69.9%	84.9%

7.5 Conclusions

MD simulation on electrical field induced conformational transition and associated frictional response change upon PEG SAMs could lead to the following conclusions:

1) Positive electrical fields can trigger the “gauche” conformational transition for PEG SAMs by twisting the glycol groups, whereas negative electrical fields are prone to keep the “all-trans” conformational transition by stretching the glycol groups straight.

2) Two stages of friction response were discovered corresponding to lower and higher normal load levels. Under lower indentation loads, the frictional coefficient of SAMs keeps increasing, while under higher indentation loads exceeding a threshold value, the frictional coefficients of SAMs decrease.

3) Under lower normal load level, positive electrical fields can induce smaller frictional coefficient than zero and negative fields, which could be attributed to the “gauche” conformation, i.e. limited interchain space constricts the deformation and energy absorption of the SAMs, thus lead to a lower friction response.

7.6 Appendix

Interatomic potential functions and associated numerical parameters

Bonded	Bonds	Harmonic: $\sum_{i,j} k_{ij}\left(r_{ij}-r_0\right)^2$
	Angles	Harmonic: $\sum_{i,j,k} k_{ijk}\left(\theta_{ijk}-\theta_0\right)^2$
	Dihedrals	Class2: $\sum_{i,j,k,l} k_{ijkl}\left[1-\cos(n\varphi_{ijkl}-\varphi_0)\right]$
Nonbonded	Lennard Jones	Universal Force Field: $V=\sum_{i,j} 4\varepsilon_{ij}\left[\left(\frac{\sigma_{ij}}{r_{ij}}\right)^{12}-\left(\frac{\sigma_{ij}}{r_{ij}}\right)^{6}\right]$

	Electrostatic	Coulombic: $\sum_{i,j} C \frac{q_i q_j}{r_{ij}}$
	Morse	For Au/S interaction: $\sum_{i,j} D_{ij}\left[e^{-2\alpha(r_{ij}-r_0)} - 2e^{-\alpha(r_{ij}-r_0)}\right]$
Electrical field		$q_i E z_i$

Bond (Harmonic) potential parameters:

	k_{ij} (Kcal/mol)	r_0 (Å)
S-C	410	1.82
C-C	309	1.51
C-H	328	1.09
C-O	370	1.39

Angle (Harmonic) potential parameters:

	k_{ijk} (Kcal/mol)	θ_0 (Degree)
S-C-H	40	109.5
S-C-C	50	114.0
H-C-H	40	108.4
C-C-H	40	109.5
C-C-C	45	111.1
C-C-O	70	109.1
H-C-O	70	110.1
C-O-C	85	118.0

Dihedral (Class2) potential parameters (from Yoon's group):

	k_{ijk} (Kcal/mol)	φ_0 (Degree)	n
S-C-C-H	0.13896	0	3
S-C-C-C	0.13896	0	3
H-C-C-H	0.13896	0	3
H-C-C-C	0.13896	0	3
C-C-C-C	0.13896	0	3
C-C-C-O	0.13896	0	3
H-C-C- O	0.13896	0	3
C-O-C-C	0.5	0	1
C-O-C-C	0.35	180	2
C-O-C-C	0.16	0	3
C-O-C-H	0.4	0	3
O-C-C-O	0.025	0	1

O-C-C-O	1.275	0	2
O-C-C-O	0	180	3

Dihedral (Class2) potential parameters (from Tasaki’s group):

	k_{ijk} (Kcal/mol)	φ_0 (Degree)	n
S-C-C-H	0.13896	0	3
S-C-C-C	0.13896	0	3
H-C-C-H	0.13896	0	3
H-C-C-C	0.13896	0	3
C-C-C-C	0.13896	0	3
C-C-C-O	0.13896	0	3
H-C-C- O	0.13896	0	3
C-O-C-C	-1.75	0	1
C-O-C-C	0.7	180	2
C-O-C-C	0.25	0	3
C-O-C-H	0.4	0	3
O-C-C-O	0	0	1
O-C-C-O	-0.675	0	2
O-C-C-O	0.3	180	3

Morse potential parameters:

	D_{ij} (Kcal/mol)	α (Å^{-1})	r_0 (Å)
Au-S	9.546	1.378	2.903

Nonbonded intermolecular potential function (LJ potential) parameters:

	ε_{ij} (Kcal/mol)	σ_{ij} (Å)
Au-C	0.06399	3.1726
Au-H	0.04142	2.7465
Au-O	0.04837	3.0245
S-S	0.27400	3.5948
S-C	0.16962	3.5119
S-H	0.10980	3.0402
S-O	0.12822	3.3480
C-C	0.10500	3.4309
C-H	0.06797	2.9700
C-O	0.07937	3.2708
H-H	0.04400	2.5711
H-O	0.05138	2.8315
O-O	0.06000	3.1181

Point charges in carboxyl headgroup:

C (in CH_2)	C (in CH_3)	H (in CH_2)	H (in CH_3)	O
-0.066	-0.366	0.097	0.122	-0.256

CHAPTER 8. CONCLUSIONS

We utilized nanofabrication technology to establish the patterned nanostructure of thobmin and aptamer, and applied controlled electrical fields onto the structure and performed height identification experiment through AFM surface imaging.

Specific binding between thrombin and aptamer was first verified. Moderate electrical fields was then utilized to induce binding change between thrombin and aptamer pair, and thus can realize the actuation and modulation of the binding behavior of the pair: a) Positive electrical fields of 100 mV can successfully break the bonds between the pair; b) Zero potential condition does not influence the binding between the pair; c) Negative electrical fields of -100mV can withhold the pair structure; while At -300mV, the whole binding pair is stretched away from the gold substrate and the nanostructure was destroyed due to too large electrostatic pushing force.

AFM experiments were conducted to determine the characteristic force associated with specific binding between thrombin and its DNA aptamer. The measured rupture force distributions extend over a larger magnitude of forces and demonstrate characteristics of force quanta for specific binding (thrombin-aptamer) in comparison to non-specific binding (thrombin-polyA). We find the characteristic force for disruption of thrombin-aptamer complexes increases from 20 to 40 pN as the loading rate level increase from 100 to 40000 pN/s. The magnitude of characteristic forces is smaller than previously reported force magnitudes associated with disruption of the G-quadruplex structure. This difference suggests that, with the application of external force on the thrombin-aptamer complex, the G-quadruplex structure of the aptamer is not disrupted and the measured characteristic forces may be associated with dissociation of thrombin and aptamer binding pair. The characteristic rupture forces were fitted to a single energy barrier model to extract the bond energy parameters associated with thrombin-aptamer binding.

Through ECAFM technique, in-situ measurement of force interaction between thrombin-aptamer binding pair can be successfully acquired. Moderate electrical fields can be utilized to influence the force interaction between thrombin and aptamer pair: a) Positive electrical fields of 100 mV can weaken the bonds between the pair; b) Neutral and negative (-100mV) electrical fields condition maintain the similar force interaction compared to the in-air DFS experiment

Molecular dynamic simulations of chain conformation and frictional response for sparse and close packed MHA SAM under applied electrical field lead us to the following conclusions: a) Sparse monomolecular films show significant conformational transition when different polarities of electrical fields were applied. Under positive electrical fields chains undergo transition from standing up to lying-down conformation, while under neutral and negative electrical fields chains show regular standing-up conformation. b) Close packed SAMs don’t show obvious conformational transition due to their high coverage density. c) For repulsive rigid indenting surface, the SAM chains provide tangential resistance through two main mechanisms: localized chain deformation and SAM structure distortion due to dragging of chains with indenter. d) For loose packed

SAMs, in lower normal load region, positive electrical fields can induce smaller frictional coefficient than neutral and negative fields. While for close packed SAMs, all kinds of electrical fields lead to similar frictional coefficients.

AFM force curve experiment was utilized to evaluate the adhesion and friction of MHA SAM under electrical field application. Contrary trends on adhesion and friction of the SAM were observed in the experiment, i.e. under positive electrical fields, adhesion force decrease, while friction force increase compared to zero potential condition, vice versa for negative electrical field application. MD simulation could provide good explanation and understanding of those phenomena, and confirm the conformational transition induced surface chemistry change as the primary factor that governs the adhesion shift, and conformational transition induced structural order change as the dominant reason for friction performance alteration.

Molecular dynamic simulations of electrical field induced conformational transition and frictional response change for close packed PEG SAM lead us to the following conclusions: a) Positive electrical fields can trigger the “gauche” conformational transition for PEG SAMs by twisting the glycol groups, whereas negative electrical fields are prone to keep the “all-trans” conformational transition by stretching the glycol groups straight. b) Two stages of friction response were discovered corresponding to lower and higher normal load levels. Under lower indentation loads, the frictional coefficient of SAMs keeps increasing, while under higher indentation loads exceeding a threshold value, the frictional coefficients of SAMs decrease. c) Under lower normal load level, positive electrical fields can induce smaller frictional coefficient than zero and negative fields, which could be attributed to the “gauche” conformation, i.e. limited interchain space constricts the deformation and energy absorption of the SAMs, thus lead to a lower friction response.

REFERENCES

Arinaga, K., U. Rant, J. Knezevic, E. Pringsheim, M. Tornow, S. Fujita, G. Abstreiter and N. Yokoyama (2007). "Controlling the surface density of DNA on gold by electrically induced desorption." Biosensors & Bioelectronics **23**(3): 326-331.

Azzaroni, O., P. L. Schilardi and R. C. Salvarezza (2003). "Metal electrodeposition on self-assembled monolayers: a versatile tool for pattern transfer on metal thin films." Electrochimica Acta **48**(20-22): 3107-3114.

Basnar, B., R. Elnathan and I. Willner (2006). "Following aptamer-thrombin binding by force measurements." Analytical Chemistry **78**(11): 3638-3642.

Bat-Uul, B., S. Fujii, T. Shiokawa, T. Ohzono and M. Fujihira (2004). "Molecular dynamics simulation of non-contact atomic force microscopy of self-assembled monolayers on Au(111)." Nanotechnology **15**(5): 710-715.

Bearinger, J. P., C. A. Orme and J. L. Gilbert (2001). "Direct observation of hydration of TiO2 on Ti using electrochemical AFM: freely corroding versus potentiostatically held conditions." Surface Science **491**(3): 370-387.

Berens, C., A. Thain and R. Schroeder (2001). "A tetracycline-binding RNA aptamer." Bioorganic & Medicinal Chemistry **9**(10): 2549-2556.

Bhushan, B., J. N. Israelachvili and U. Landman (1995). "Nanotribology - Friction, Wear and Lubrication at the Atomic-Scale." Nature **374**(6523): 607-616.

Bloess, H., G. Staikov and J. W. Schultze (2001). "AFM induced formation of SiO2 structures in the electrochemical nanocell." Electrochimica Acta **47**(1-2): 335-344.

Bock, L. C., L. C. Griffin, J. A. Latham, E. H. Vermaas and J. J. Toole (1992). "Selection of Single-Stranded-DNA Molecules That Bind and Inhibit Human Thrombin." Nature **355**(6360): 564-566.

Bode, W., I. Mayr, U. Baumann, R. Huber, S. R. Stone and J. Hofsteenge (1989). "The Refined 1.9 a Crystal-Structure of Human Alpha-Thrombin - Interaction with D-Phe-Pro-Arg Chloromethylketone and Significance of the Tyr-Pro-Pro-Trp Insertion Segment." Embo Journal **8**(11): 3467-3475.

Bonner, T. and A. Baratoff (1997). "Molecular dynamics study of scanning force microscopy on self-assembled monolayers." Surface Science **377**(1-3): 1082-1086.

Boussaad, S. and N. J. Tao (1999). "Electron transfer and adsorption of myoglobin on self-assembled surfactant films: An electrochemical tapping-mode AFM study." Journal of the American Chemical Society **121**(18): 4510-4515.

Breisch, S., J. Gonska, H. Deissler and M. Stelzle (2005). "Measuring single-bond rupture forces using high electric fields in microfluidic channels and DNA oligomers as force tags." Biophysical Journal **89**(3): L19-L21.

Brenner, D. W., J. A. Harrison, C. T. White and R. J. Colton (1991). "Molecular-Dynamics Simulations of the Nanometer-Scale Mechanical-Properties of Compressed Buckminsterfullerene." Thin Solid Films **206**(1-2): 220-223.

Briscoe, B. J. and D. C. B. Evans (1982). "The Shear Properties of Langmuir-Blodgett Layers." Proceedings of the Royal Society of London Series a-Mathematical Physical and Engineering Sciences **380**(1779): 389-&.

Brooks, B. and M. Karplus (1983). "Harmonic Dynamics of Proteins - Normal-Modes and Fluctuations in Bovine Pancreatic Trypsin-Inhibitor." Proceedings of the National Academy of Sciences of the United States of America-Biological Sciences **80**(21): 6571-6575.

Brooks, B. R., R. E. Bruccoleri, B. D. Olafson, D. J. States, S. Swaminathan and M. Karplus (1983). "Charmm - a Program for Macromolecular Energy, Minimization, and Dynamics Calculations." Journal of Computational Chemistry **4**(2): 187-217.

Burke, D. H., D. C. Hoffman, A. Brown, M. Hansen, A. Pardi and L. Gold (1997). "RNA aptamers to the peptidyl transferase inhibitor chloramphenicol." Chemistry & Biology **4**(11): 833-843.

Burt, D. P., P. S. Dobson, J. M. R. Weaver, N. R. Wilson, P. R. Unwin and J. V. Macpherson (2007). "Developments in nanowire scanning electrochemical-atomic force microscopy (SECM-AFM) probes." 2007 Ieee Sensors, Vols 1-3: 712-715.

Chandross, M., C. A. Lorenz, G. S. Grest, M. J. Stevens and E. B. Webb (2005). "Nanotribology of anti-friction coatings in MEMS." Jom **57**(9): 55-61.

Chandross, M., E. B. Webb, M. J. Stevens, G. S. Grest and S. H. Garofalini (2004). "Systematic study of the effect of disorder on nanotribology of self-assembled monolayers." Physical Review Letters **93**(16).

Chang, W. Y., T. H. Fang and C. N. Fang (2009). "Molecular Dynamics on Interface and Nanoscratch Mechanisms of Alkanethiol Self-Assembled Monolayers." Journal of Physical Chemistry B **113**(45): 14994-15001.

Chen, J. R. and W. T. Tsai (2011). "In situ corrosion monitoring of Ti-6Al-4V alloy in H2SO4/HCl mixed solution using electrochemical AFM." Electrochimica Acta **56**(4): 1746-1751.

Chiorcea, A. M. and A. M. O. Brett (2005). "AFM of guanine adsorbed on HOPG under electrochemical control." Scanning Probe Microscopy: Characterization, Nanofabrication and Device Application of Functional Materials **186**: 467-+.

Coughlin, M. P. and T. H. Huang (2005). "Electrochemical AFM and STM investigation of mixed polymers of polyaniline and polystyrene sulfonate on gold." Abstracts of Papers of the American Chemical Society **229**: U133-U133.

Cullen, B. R. and W. C. Greene (1989). "Regulatory Pathways Governing Hiv-1 Replication." Cell **58**(3): 423-426.

de Abril, O., A. Gundel, F. Maroun, P. Allongue and R. Schuster (2008). "Single-step electrochemical nanolithography of metal thin films by localized etching with an AFM tip." Nanotechnology **19**(32).

Doi, T., M. Inaba, H. Tsuchiya, S. K. Jeong, Y. Iriyama, T. Abe and Z. Ogumi (2008). "Electrochemical AFM study of LiMn2O4 thin film electrodes exposed to elevated temperatures." Journal of Power Sources **180**(1): 539-545.

Domi, Y., T. Doi, T. Yamanaka, T. Abe and Z. Ogumi (2013). "Electrochemical AFM Study of Surface Films Formed on the HOPG Edge Plane in Propylene Carbonate-Based Electrolytes." Journal of the Electrochemical Society **160**(4): A678-A683.

Domi, Y., M. Ochida, S. Tsubouchi, H. Nakagawa, T. Yamanaka, T. Doi, T. Abe and Z. Ogumia (2012). "Electrochemical AFM Observation of the HOPG Edge Plane in Ethylene Carbonate-Based Electrolytes Containing Film-Forming Additives." Journal of the Electrochemical Society **159**(8): A1292-A1297.

Dudko, O. K. M., A (2009). Probing Biomolecular Interactions Using Nanopore Force Spectroscopy, John Wiley & Sons Ltd.

Eckhard, K., H. Shin, B. Mizaikoff, W. Schuhmann and C. Kranz (2007). "Alternating current (AC) impedance imaging with combined atomic force scanning electrochemical microscopy (AFM-SECM)." Electrochemistry Communications **9**(6): 1311-1315.

Efron, B. (1979). "1977 Rietz Lecture - Bootstrap Methods - Another Look at the Jackknife." Annals of Statistics **7**(1): 1-26.

Efron, B. T., R. (1993). An Introduction to the Bootstrap, Boca Raton, FL: Chapman & Hall/CRC.

Eick, K., O. Kahlen, D. Regener and J. Gollner (2000). "In situ observation of local corrosion events with electrochemical AFM investigations." Materials and Corrosion-Werkstoffe Und Korrosion **51**(8): 557-563.

ElKaoutit, M., A. H. Naggar, I. Naranjo-Rodriguez, M. Dominguez and J. L. H. H. de Cisneros (2009). "Electrochemical AFM investigation of horseradish peroxidase enzyme electro-immobilization with polypyrrole conducting polymer." Synthetic Metals **159**(5-6): 541-545.

Ellington, A. D. and J. W. Szostak (1990). "Invitro Selection of Rna Molecules That Bind Specific Ligands." Nature **346**(6287): 818-822.

Engler, E. M., J. D. Andose and P. V. Schleyer (1973). "Critical Evaluation of Molecular Mechanics." Journal of the American Chemical Society **95**(24): 8005-8025.

Erdmann, T., S. Pierrat, P. Nassoy and U. S. Schwarz (2008). "Dynamic force spectroscopy on multiple bonds: Experiments and model." Epl **81**(4).

Evans, E. (1998). "Energy landscapes of biomolecular adhesion and receptor anchoring at interfaces explored with dynamic force spectroscopy." Faraday Discussions **111**: 1-16.

Evans, E. (2001). "Probing the relation between force - Lifetime - and chemistry in single molecular bonds." Annual Review of Biophysics and Biomolecular Structure **30**: 105-128.

Evans, E., A. Leung, D. Hammer and S. Simon (2001). "Chemically distinct transition states govern rapid dissociation of single L-selectin bonds under force." Proceedings of the National Academy of Sciences of the United States of America **98**(7): 3784-3789.

Evans, E. B. (1999). "Looking inside molecular bonds at biological interfaces with dynamic force spectroscopy." Biophysical Chemistry **82**(2-3): 83-97.

Fan, F. R. F., J. P. Yang, L. T. Cai, D. W. Price, S. M. Dirk, D. V. Kosynkin, Y. X. Yao, A. M. Rawlett, J. M. Tour and A. J. Bard (2002). "Charge transport through self-assembled monolayers of compounds of interest in molecular electronics." Journal of the American Chemical Society **124**(19): 5550-5560.

Fan, F. R. F., Y. X. Yao, L. T. Cai, L. Cheng, J. M. Tour and A. J. Bard (2004). "Structure-dependent charge transport and storage in self-assembled monolayers of compounds of interest in molecular electronics: Effects of tip material, headgroup, and surface concentration." Journal of the American Chemical Society **126**(12): 4035-4042.

Fang, T. H., W. J. Chang, Y. C. Fan and C. I. Weng (2009). "Molecular dynamics of contact behavior of self-assembled monolayers on gold using nanoindentation." Applied Surface Science **255**(21): 8931-8934.

Fasching, R. J., Y. Tao and F. B. Prinz (2004). "Fabrication of an electrochemical tip-probe system embedded in SiNx-cantilevers for simultaneous SECM and AFM analysis." Micromachining and Microfabrication Process Technology Ix **5342**: 53-64.

Florin, E. L., V. T. Moy and H. E. Gaub (1994). "Adhesion Forces between Individual Ligand-Receptor Pairs." Science **264**(5157): 415-417.

Flyvbjerg, H. (2002). Physics of Bio-Molecules and Cells. Les Houches - Ecole d'Ete de Physique Theorique. F. J. Henrik Flyvbjerg, Pal Ormos, Francois David, Springer.

Ge, L., G. Jin and X. H. Fang (2012). "Investigation of the Interaction between a Bivalent Aptamer and Thrombin by AFM." Langmuir **28**(1): 707-713.

Geng, X., Z. Jiao, H. B. Wang, Q. Fu, H. J. Zhong and Z. Li (2006). "The Al2O3 nanowire grown on silicon chips by electrochemical reaction under AFM probe." 2006 1st Ieee International Conference on Nano/Micro Engineered and Molecular Systems, Vols 1-3: 679-681.

Ghorai, P. K. and S. C. Glotzer (2007). "Molecular dynamics simulation study of self-assembled monolayers of alkanethiol surfactants on spherical gold nanoparticles." Journal of Physical Chemistry C **111**(43): 15857-15862.

Ghorbal, A., F. Grisotto, J. Charlier, S. Palacin, C. Goyer and C. Demaille (2009). "Localized Electrografting of Vinylic Monomers on a Conducting Substrate by Means of an Integrated Electrochemical AFM Probe." Chemphyschem **10**(7): 1053-1057.

Gray, H. B. and J. R. Winkler (1996). "Electron transfer in proteins." Annual Review of Biochemistry **65**: 537-561.

Gronewold, T. M. A., S. Glass, E. Quandt and M. Famulok (2005). "Monitoring complex formation in the blood-coagulation cascade using aptamer-coated SAW sensors." Biosensors & Bioelectronics **20**(10): 2044-2052.

Gus'kova, O. A., E. Mena-Osteritz, E. Schillinger, P. G. Khalatur, P. Bauerle and A. R. Khokhlov (2007). "Self-assembled monolayers of beta-alkylated oligothiophenes on graphite substrate: Molecular dynamics simulation." Journal of Physical Chemistry C **111**(19): 7165-7174.

Hao, X., J. D. Zhang, H. E. M. Christensen, H. D. Wang and J. Ulstrup (2012). "Electrochemical Single-Molecule AFM of the Redox Metalloenzyme Copper Nitrite Reductase in Action." Chemphyschem **13**(12): 2919-2924.

Harrison, J. A., P. T. Mikulski and S. J. Stuart (2001). "Tribology of alkane monolayers: The effects of tip flexibility and defects." Abstracts of Papers of the American Chemical Society **221**: U383-U383.

Harrison, J. A., J. D. Schall, M. T. Knippenberg, G. T. Gao and P. T. Mikulski (2008). "Elucidating atomic-scale friction using molecular dynamics and specialized analysis techniques." Journal of Physics-Condensed Matter **20**(35).

Harrison, J. A., A. B. Tutein and S. J. Stuart (1999). "Molecular dynamics investigation of the atomic-scale friction of hydrocarbon self-assembled monolayers." Abstracts of Papers of the American Chemical Society **218**: U445-U445.

Harrison, J. A., C. T. White, R. J. Colton and D. W. Brenner (1992). "Molecular-Dynamics Simulations of Atomic-Scale Friction of Diamond Surfaces." Physical Review B **46**(15): 9700-9708.

Harrison, J. A., C. T. White, R. J. Colton and D. W. Brenner (1995). "Investigation of the Atomic-Scale Friction and Energy-Dissipation in Diamond Using Molecular-Dynamics." Thin Solid Films **260**(2): 205-211.

Harrison, J. A. S., S. J. ; Tutein, A. B. (2001). A new, reactive potential energy function to study the indentation and friction of C13 n-alkane monolayers. ACS Symp. Series: Interfacial Properties on the Submicron Scale., Washington, DC, American Chemical Society.

Harrison, J. A. S., S. J. ; Tutein, A. B. (2001). A new, reactive potential energy function to study the indentation and friction of C13 n-alkane monolayers. ACS Symp. Series: Interfacial Properties on the Submicron Scale, Washington, DC, American Chemical Society.

Harrison, J. A. S., S.J.; Tutein,A.B. (2001). a new, reactive potential energy function to study the indentation and friction of C13 n-alkane monolayers. ACS Symp. Series: Interfacial Properties on the Submicrometer Scale, Washington, DC.

Hermann, T. and D. J. Patel (2000). "Biochemistry - Adaptive recognition by nucleic acid aptamers." Science **287**(5454): 820-825.

Hianik, T., V. Ostatna, M. Sonlajtnerova and I. Grman (2007). "Influence of ionic strength, pH and aptamer configuration for binding affinity to thrombin." Bioelectrochemistry **70**(1): 127-133.

Hianik, T., V. Ostatna, Z. Zajacova, E. Stoikova and G. Evtugyn (2005). "Detection of aptamer-protein interactions using QCM and electrochemical indicator methods." Bioorganic & Medicinal Chemistry Letters **15**(2): 291-295.

Hink, S., E. Aleksandrova and E. Roduner (2010). "Electrochemical AFM Investigations of Proton Conducting Membranes." Polymer Electrolyte Fuel Cells 10, Pts 1 and 2 **33**(1): 57-70.

Holder, M. N., C. E. Gardner, J. V. Macpherson and P. R. Unwin (2005). "Combined scanning electrochemical-atomic force microscopy (SECM-AFM): Simulation and experiment for flux-generation at un-insulated metal-coated probes." Journal of Electroanalytical Chemistry **585**(1): 8-18.

Hu, Y. Z., T. Zhang, T. B. Ma and H. Wang (2006). "Molecular dynamics simulations on atomic friction between self-assembled monolayers: Commensurate and incommensurate sliding." Computational Materials Science **38**(1): 98-104.

Huitink, D., F. Gao and H. Liang (2010). "Tribo-Electrochemical Surface Modification of Tantalum Using In Situ AFM Techniques." Scanning **32**(5): 336-344.

Jackman, R. J., J. L. Wilbur and G. M. Whitesides (1995). "Fabrication of Submicrometer Features on Curved Substrates by Microcontact Printing." Science **269**(5224): 664-666.

Jaffe, R. L., G. D. Smith and D. Y. Yoon (1993). "Conformations of 1,2-Dimethoxyethane from Ab-Initio Electronic-Structure Calculations." Journal of Physical Chemistry **97**(49): 12745-12751.

Jang, S. S., Y. H. Jang, Y. H. Kim, W. A. Goddard, A. H. Flood, B. W. Laursen, H. R. Tseng, J. F. Stoddart, J. O. Jeppesen, J. W. Choi, D. W. Steuerman, E. DeIonno and J. R. Heath (2005). "Structures and properties of self-assembled monolayers of bistable [2]rotaxanes on Au(111) surfaces from molecular dynamics simulations validated with experiment." Journal of the American Chemical Society **127**(5): 1563-1575.

Jenison, R. D., S. C. Gill, A. Pardi and B. Polisky (1994). "High-Resolution Molecular Discrimination by Rna." Science **263**(5152): 1425-1429.

Jones, C. E., P. R. Unwin and J. V. Macpherson (2003). "In situ observation of the surface processes involved in dissolution from the cleavage surface of calcite in aqueous solution using combined scanning electrochemical-atomic force microscopy (SECM-AFM)." Chemphyschem **4**(2): 139-146.

Kado, S. and K. Kimura (2003). "Single complexation force of 18-crown-6 with ammonium ion evaluated by atomic force microscopy." Journal of the American Chemical Society **125**(15): 4560-4564.

Kane, R. S., S. Takayama, E. Ostuni, D. E. Ingber and G. M. Whitesides (1999). "Patterning proteins and cells using soft lithography." Biomaterials **20**(23-24): 2363-2376.
Kapila, V., P. A. Deymier and S. Raghavan (2006). "Molecular dynamics simulations of friction between alkylsilane monolayers." Modelling and Simulation in Materials Science and Engineering **14**(2): 283-297.

Karuppiah, K. S. K., Y. B. Zhou, L. K. Woo and S. Sundararajan (2009). "Nanoscale Friction Switches: Friction Modulation of Monomolecular Assemblies Using External Electric Fields." Langmuir **25**(20): 12114-12119.

Kelchner, C. L., S. J. Plimpton and J. C. Hamilton (1998). "Dislocation nucleation and defect structure during surface indentation." Physical Review B **58**(17): 11085-11088.

Kelly, J. A., J. Feigon and T. O. Yeates (1996). "Reconciliation of the X-ray and NMR structures of the thrombin-binding aptamer d(GGTTGGTGTGGTTGG)." Journal of Molecular Biology **256**(3): 417-422.

Kepler, K. D. and A. A. Gewirth (1994). "In-Situ Afm and Stm Investigation of Electrochemical Hydride Growth on Ge(110) and Ge(111) Surfaces." Surface Science **303**(1-2): 101-113.

Koch, S. J. and M. D. Wang (2003). "Dynamic force spectroscopy of protein-DNA interactions by unzipping DNA." Physical Review Letters **91**(2).

Koinuma, M. and K. Uosaki (1995). "An Electrochemical Afm Study on Electrodeposition of Copper on P-Gaas(100) Surface in Hcl Solution." Electrochimica Acta **40**(10): 1345-1351.

Koinuma, M. and K. Uosaki (1996). "AFM tip induced selective electrochemical etching of and metal deposition on p-GaAs(100) surface." Surface Science **357**(1-3): 565-570.

Kranz, C., A. Kueng, A. Lugstein, E. Bertagnolli and B. Mizaikoff (2003). "Simultaneous electrochemical and AFM imaging in tapping mode of soft samples with bifunctional scanning probe tips." Abstracts of Papers of the American Chemical Society **226**: U131-U131.

Kubo, K., N. Hirai, T. Tanaka and S. Hara (2003). "In situ observation on Au(100) surface in molten EMImBF(4) by electrochemical atomic force microscopy (EC-AFM)." Surface Science **546**(1): L785-L788.

Kueng, A., C. Kranz, A. Lugstein, E. Bertagnolli and B. Mizaikoff (2003). "Integrated AFM-SECM in tapping mode: Simultaneous topographical and electrochemical imaging of enzyme activity." Angewandte Chemie-International Edition **42**(28): 3238-3240.

Kumar, A. and G. M. Whitesides (1993). "Features of Gold Having Micrometer to Centimeter Dimensions Can Be Formed through a Combination of Stamping with an Elastomeric Stamp and an Alkanethiol Ink Followed by Chemical Etching." Applied Physics Letters **63**(14): 2002-2004.

Lahann, J., S. Mitragotri, T. N. Tran, H. Kaido, J. Sundaram, I. S. Choi, S. Hoffer, G. A. Somorjai and R. Langer (2003). "A reversibly switching surface." Science **299**(5605): 371-374.

Lapkowski, M., J. Zak, M. Kolodziej-Sadlok, S. Guillerez and G. Bidan (2001). "In situ AFM and conductivity measurements of regioregular oligoalkylthiophenes during electrochemical doping." Synthetic Metals **119**(1-3): 417-418.

Lato, S. M., A. R. Boles and A. D. Ellington (1995). "In-Vitro Selection of Rna Lectins - Using Combinatorial Chemistry to Interpret Ribozyme Evolution." Chemistry & Biology **2**(5): 291-303.

Lavrik, N. V., M. J. Sepaniak and P. G. Datskos (2004). "Cantilever transducers as a platform for chemical and biological sensors." Review of Scientific Instruments **75**(7): 2229-2253.

Leith, D. and D. A. Morton-Blake (2005). "A molecular dynamics simulation of the structure and properties of a self assembled monolayer formed from an amphiphilic polymer on a water surface." Molecular Simulation **31**(14-15): 987-997.

Li, L. C., S.; Jiang,S. (2001). Interfacial Properties on the Submicron Scale. ACS symposium Series, Washington, DC.

Li, X. X., L. H. Shen, D. D. Zhang, H. L. Qi, Q. Gao, F. Ma and C. X. Zhang (2008). "Electrochemical impedance spectroscopy for study of aptamer-thrombin interfacial interactions." Biosensors & Bioelectronics **23**(11): 1624-1630.

Li, Y., M. Ben and J. Liu (2002). "Electrochemical AFM "dip-pen" nanolithography and more." Chinese Journal of Inorganic Chemistry **18**(1): 75-78.

Li, Y., B. W. Maynor and J. Liu (2001). "Electrochemical AFM "dip-pen" nanolithography." Journal of the American Chemical Society **123**(9): 2105-2106.

Lifson, S. and A. Warshel (1968). "Consistent Force Field for Calculations of Conformations Vibrational Spectra and Enthalpies of Cycloalkane and N-Alkane Molecules." Journal of Chemical Physics **49**(11): 5116-&.

Liu, H. W., S. Fujisawa, A. Tanaka and Y. Enomoto (2000). "Controlling and improving the microtribological properties of Langmuir-Blodgett monolayer films using an external electric field." Thin Solid Films **368**(1): 151-155.

Liu, Y. X. and T. H. Cui (2005). "Metal-oxide-semiconductor capacitors fabricated by layer-by-layer nanoassembly and microfabrication." Journal of Nanoscience and Nanotechnology **5**(2): 192-197.

Luedtkea, W. D. L., U. (1992). "Solid and liquid junctions." Comput. Mater. Sci. **1**: 1-24.
Lugstein, A., E. Bertagnolli, C. Kranz and B. Mizaikoff (2002). "Fabrication of a ring nanoelectrode in an AFM tip: novel approach towards simultaneous electrochemical and topographical imaging." Surface and Interface Analysis **33**(2): 146-150.

Lynch, S., H. Baker, S. G. Byker, D. J. Zhou and K. Sinniah (2009). "Single Molecule Force Spectroscopy on G-Quadruplex DNA." Chemistry-a European Journal **15**(33): 8113-8116.

Maboudian, R., W. R. Ashurst and C. Carraro (2000). "Self-assembled monolayers as anti-stiction coatings for MEMS: characteristics and recent developments." Sensors and Actuators a-Physical **82**(1-3): 219-223.

Macpherson, J. V., P. R. Unwin, A. C. Hillier and A. J. Bard (1996). "In-situ imaging of ionic crystal dissolution using an integrated electrochemical/AFM probe." Journal of the American Chemical Society **118**(27): 6445-6452.

Manniron, C., A. DiNardo, P. Fruscoloni and G. P. TocchiniValentini (1997). "In vitro selection of dopamine RNA ligands." Biochemistry **36**(32): 9726-9734.

Merkel, R., P. Nassoy, A. Leung, K. Ritchie and E. Evans (1999). "Energy landscapes of receptor-ligand bonds explored with dynamic force spectroscopy." Nature **397**(6714): 50-53.

Mikulski, P. T. and J. A. Harrison (2001). "Periodicities in the properties associated with the friction of model self-assembled monolayers." Tribology Letters **10**(1-2): 29-35.

Miyachi, Y., N. Shimizu, C. Ogino and A. Kondo (2010). "Selection of DNA aptamers using atomic force microscopy." Nucleic Acids Research **38**(4).

Moon, J. S., J. Wiedemair, J. F. Masson, B. Mizalkoff and C. Kranz (2007). "Atomic force scanning electrochemical microscopy (AFM-SECM) for electrochemical imaging at the nanoscale." Microscopy and Microanalysis **13**: 58-59.

Moy, V. T., E. L. Florin and H. E. Gaub (1994). "Intermolecular Forces and Energies between Ligands and Receptors." Science **266**(5183): 257-259.

Mulliken, R. S. (1955). "Electronic Population Analysis on Lcao-Mo Molecular Wave Functions .1." Journal of Chemical Physics **23**(10): 1833-1840.

Mulliken, R. S. (1955). "Electronic Population Analysis on Lcao-Mo Molecular Wave Functions .2. Overlap Populations, Bond Orders, and Covalent Bond Energies." Journal of Chemical Physics **23**(10): 1841-1846.

Mulliken, R. S. (1955). "Electronic Population Analysis on Lcao-Mo Molecular Wave Functions .3. Effects of Hybridization on Overlap and Gross Ao Populations." Journal of Chemical Physics **23**(12): 2338-2342.

Mulliken, R. S. (1955). "Electronic Population Analysis on Lcao-Mo Molecular Wave Functions .4. Bonding and Antibonding in Lcao and Valence-Bond Theories." Journal of Chemical Physics **23**(12): 2343-2346.

Mulliken, R. S. (1995). "Electronic population analysis on LCAO-MO molecular wave functions: I." J Chem Phys **23**: 1833-1831.

Naoi, K., H. Ooike and Y. Oura (1994). "Monitoring of Polymerization-Depolymerization Processes of Disulfide Compounds by Use of in-Situ Electrochemical Afm and Qcm Spectroscopy." Denki Kagaku **62**(6): 534-537.

Nguyen, T., R. J. Pei, D. W. Landry, M. N. Stojanovic and Q. Lin (2011). "Label-free microfluidic characterization of temperature-dependent biomolecular interactions." Biomicrofluidics **5**(3).

Ohzono, T. and M. Fujihira (2000). "Molecular dynamics simulations of friction between an ordered organic monolayer and a rigid slider with an atomic-scale protuberance." Physical Review B **62**(24): 17055-17071.

Oncins, G., C. Vericat and F. Sanz (2008). "Mechanical properties of alkanethiol monolayers studied by force spectroscopy." Journal of Chemical Physics **128**(4).

Osnis, A., C. N. Sukenik and D. T. Major (2012). "Structure of Carboxyl-Acid-Terminated Self-Assembled Monolayers from Molecular Dynamics Simulations and Hybrid Quantum Mechanics-Molecular Mechanics Vibrational Normal-Mode Analysis." Journal of Physical Chemistry C **116**(1): 770-782.

Pan, J., M. Femenia and C. Leygraf (2000). "Corrosion behaviour of a duplex stainless steel studied by STM/AFM based scanning electrochemical microscopy." Localized in-Situ Methods for Investigating Electrochemical Interfaces **99**(28): 131-146.

Pei, Y. and J. Ma (2005). "Electric field induced switching behaviors of monolayer-modified silicon surfaces: Surface designs and molecular dynamics simulations." Journal of the American Chemical Society **127**(18): 6802-6813.

Pertsin, A. J. and M. Grunze (1994). "Low-Energy Structures of a Monolayer of Octadecanethiol Self-Assembled on Au(111)." Langmuir **10**(10): 3668-3674.

Peter, M., M. A. Hempenius, R. G. H. Lammertink, M. T. van Os and G. J. Vancso (2000). "Electrochemical AFM on surface grafted poly(ferrocenylsilanes)." Abstracts of Papers of the American Chemical Society **220**: U287-U287.

Peter, M., M. A. Hempenius, R. G. H. Lammertink and J. G. Vancso (2001). "Electrochemical AFM on surface grafted poly(ferrocenylsilanes)." Macromolecular Symposia **167**: 285-296.

Plimpton, S. (1995). "Fast Parallel Algorithms for Short-Range Molecular-Dynamics." Journal of Computational Physics **117**(1): 1-19.

Pope, L. H., M. C. Davies, C. A. Laughton, C. J. Roberts, S. J. B. Tendler and P. M. Williams (2001). "Force-induced melting of a short DNA double helix." European Biophysics Journal with Biophysics Letters **30**(1): 53-62.

Prime, K. L. and G. M. Whitesides (1991). "Self-Assembled Organic Monolayers - Model Systems for Studying Adsorption of Proteins at Surfaces." Science **252**(5009): 1164-1167.

Ramin, L. and A. Jabbarzadeh (2011). "Effect of Loading and Shear Rate on Tribological Behaviour of Dodecanethiol Self Assembled Monolayer on Au(111): A Molecular Dynamic Simulation Study." Proceedings of the Stle/Asme International Joint Tribology Conference, 2010: 5-7.

Rant, U., K. Arinaga, S. Fujita, N. Yokoyama, G. Abstreiter and M. Tornow (2004). "Dynamic electrical switching of DNA layers on a metal surface." Nano Letters **4**(12): 2441-2445.

Rant, U., K. Arinaga, S. Scherer, E. Pringsheim, S. Fujita, N. Yokoyama, M. Tornow and G. Abstreiter (2007). "Switchable DNA interfaces for the highly sensitive detection of label-free DNA targets." Proceedings of the National Academy of Sciences of the United States of America **104**(44): 17364-17369.

Rappe, A. K., C. J. Casewit, K. S. Colwell, W. A. Goddard and W. M. Skiff (1992). "Uff, a Full Periodic-Table Force-Field for Molecular Mechanics and Molecular-Dynamics Simulations." Journal of the American Chemical Society **114**(25): 10024-10035.

Reynaud-Laporte, I., M. Vayer, J. P. Kauffmann and R. Erre (1997). "An electrochemical-AFM study of the initiation of the pitting of a martensitic stainless steel." Microscopy Microanalysis Microstructures **8**(3): 175-185.

Romer, J., M. Plaschke, G. Beuchle and J. I. Kim (2003). "In situ investigation of U(IV)-oxide surface dissolution and remineralization by electrochemical AFM." Journal of Nuclear Materials **322**(1): 80-86.

Sader, J. E., J. W. M. Chon and P. Mulvaney (1999). "Calibration of rectangular atomic force microscope cantilevers." Review of Scientific Instruments **70**(10): 3967-3969.

Schneegans, O., A. Moradpour, L. Boyer and D. Ballutaud (2004). "Nanosized electrochemical cells operated by AFM conducting probes." Journal of Physical Chemistry B **108**(28): 9882-9887.

Schon, J. H., H. Meng and Z. Bao (2001). "Self-assembled monolayer organic field-effect transistors (Retracted article. See vol 422 pg 92 2003)." Nature **413**(6857): 713-716.

Schon, J. H., H. Meng and Z. N. Bao (2001). "Self-assembled monolayer organic field-effect transistors (Retraction of vol 413, vol 713, 2001)." Nature **414**(6862): 470-470.

Sekine, S., H. Kaji and M. Nishizawa (2008). "Integration of an electrochemical-based biolithography technique into an AFM system." Analytical and Bioanalytical Chemistry **391**(8): 2711-2716.

Sekine, S., H. Kaji and M. Nishizawa (2009). "Spatiotemporal sub-cellular biopatterning using an AFM-assisted electrochemical system." Electrochemistry Communications **11**(9): 1781-1784.

Semenikhin, O. A., L. Jiang, T. Iyoda, K. Hashimoto and A. Fujishima (2000). "In situ AFM study of the electrochemical deposition of polybithiophene from propylene carbonate solution." Synthetic Metals **110**(3): 195-201.

Shapiro, S. S. and M. B. Wilk (1965). "An Analysis of Variance Test for Normality (Complete Samples)." Biometrika **52**: 591-&.

Shimizu, J., H. Eda, M. Yoritsune and E. Ohmura (1998). "Molecular dynamics simulation of friction on the atomic scale." Nanotechnology **9**(2): 118-123.

Shin, H., P. J. Hesketh, B. Mizaikofff and C. Kranz (2008). "Development of wafer-level batch fabrication for combined atomic force-scanning electrochemical microscopy (AFM-SECM) probes." Sensors and Actuators B-Chemical **134**(2): 488-495.

Smith, G. D., R. L. Jaffe and D. Y. Yoon (1993). "A Force-Field for Simulations of 1,2-Dimethoxyethane and Poly(Oxyethylene) Based Upon Ab-Initio Electronic-Structure Calculations on Model Molecules." Journal of Physical Chemistry **97**(49): 12752-12759.

Sorensen, R. A., W. B. Liau, L. Kesner and R. H. Boyd (1988). "Prediction of Polymer Crystal-Structures and Properties - Polyethylene and Poly(Oxymethylene)." Macromolecules **21**(1): 200-208.

Srinivasan, U., M. R. Houston, R. T. Howe and R. Maboudian (1998). "Alkyltrichlorosilane-based self-assembled monolayer films for stiction reduction in silicon micromachines." Journal of Microelectromechanical Systems **7**(2): 252-260.

Stapleton, J. J., P. Harder, T. A. Daniel, M. D. Reinard, Y. X. Yao, D. W. Price, J. M. Tour and D. L. Allara (2003). "Self-assembled oligo(phenylene-ethynylene) molecular electronic switch monolayers on gold: Structures and chemical stability." Langmuir **19**(20): 8245-8255.

Stojanovic, M. N., P. de Prada and D. W. Landry (2001). "Aptamer-based folding fluorescent sensor for cocaine." Journal of the American Chemical Society **123**(21): 4928-4931.

Strunz, T., K. Oroszlan, R. Schafer and H. J. Guntherodt (1999). "Dynamic force spectroscopy of single DNA molecules." Proceedings of the National Academy of Sciences of the United States of America **96**(20): 11277-11282.

Sundararajan, S. and B. Bhushan (2001). "Static friction and surface roughness studies of surface micromachined electrostatic micromotors using an atomic force/friction force microscope." Journal of Vacuum Science & Technology a-Vacuum Surfaces and Films **19**(4): 1777-1785.

Sung, I. H. and D. E. Kim (2005). "Molecular dynamics simulation study of the nano-wear characteristics of alkanethiol self-assembled monolayers." Applied Physics a-Materials Science & Processing **81**(1): 109-114.

Tamura, K., T. Kondo and K. Uosaki (2000). "In situ optical and electrochemical AFM monitoring of Cu electrodeposition process on bare and (NH4)(2)S-treated p-GaAs(001) surfaces." Journal of the Electrochemical Society **147**(9): 3356-3360.

Tasaki, K. (1996). "Conformation and dynamics of poly(oxyethylene) in benzene solution: Solvent effect from molecular dynamics simulation." Macromolecules **29**(27): 8922-8933.

Tasaki, K. (1996). "Poly(oxyethylene)-water interactions: A molecular dynamics study." Journal of the American Chemical Society **118**(35): 8459-8469.

Tasset, D. M., M. F. Kubik and W. Steiner (1997). "Oligonucleotide inhibitors of human thrombin that bind distinct epitopes." Journal of Molecular Biology **272**(5): 688-698.

Tsiang, M., C. S. Gibbs, L. C. Griffin, K. E. Dunn and L. L. K. Leung (1995). "Selection of a Suppressor Mutation That Restores Affinity of an Oligonucleotide Inhibitor for Thrombin Using in-Vitro Genetics." Journal of Biological Chemistry **270**(33): 19370-19376.

Tuerk, C. and L. Gold (1990). "Systematic Evolution of Ligands by Exponential Enrichment - Rna Ligands to Bacteriophage-T4 DNA-Polymerase." Science **249**(4968): 505-510.

Tupper, K. J. and D. W. Brenner (1994). "Molecular-Dynamics Simulations of Friction in Self-Assembled Monolayers." Thin Solid Films **253**(1-2): 185-189.

Ulman, A. (1990). "Self-Assembled Monolayers of Alkyltrichlorosilanes - Building-Blocks for Future Organic Materials." Advanced Materials **2**(12): 573-582.

Umeda, K. and K. Fukui (2010). "Observation of Redox-State-Dependent Reversible Local Structural Change of Ferrocenyl-Terminated Molecular Island by Electrochemical Frequency Modulation AFM." Langmuir **26**(11): 9104-9110.

Vemparala, S., R. K. Kalia, A. Nakano and P. Vashishta (2004). "Electric field induced switching of poly(ethylene glycol) terminated self-assembled monolayers: A parallel molecular dynamics simulation." Journal of Chemical Physics **121**(11): 5427-5433.

Vidu, R. and S. Hara (1999). "Surface alloying at the Cd vertical bar Au(100) interface in the upd region. Electrochemical studies and in situ EC-AFM observation." Journal of Electroanalytical Chemistry **475**(2): 171-180.

Vidu, R., F. T. Quinlan and P. Stroeve (2002). "Use of in situ electrochemical atomic force microscopy (EC-AFM) to monitor cathode surface reaction in organic electrolyte." Industrial & Engineering Chemistry Research **41**(25): 6546-6554.

Villarroya, M., F. Perez-Murano, C. Martin, Z. Davis, A. Boisen, J. Esteve, E. Figueras, J. Montserrat and N. Barniol (2004). "AFM lithography for the definition of nanometre scale gaps: application to the fabrication of a cantilever-based sensor with electrochemical current detection." Nanotechnology **15**(7): 771-776.

Wallace, S. T. and R. Schroeder (1998). "In vitro selection and characterization of streptomycin-binding RNAs: Recognition discrimination between antibiotics." Rna-a Publication of the Rna Society **4**(1): 112-123.

Wallis, M. G., U. Vonahsen, R. Schroeder and M. Famulok (1995). "A Novel Rna Motif for Neomycin Recognition." Chemistry & Biology **2**(8): 543-552.

Wang, Y. and R. R. Rando (1995). "Specific Binding of Aminoglycoside Antibiotics to Rna." Chemistry & Biology **2**(5): 281-290.

Wilbur, J. L., A. Kumar, H. A. Biebuyck, E. Kim and G. M. Whitesides (1996). "Microcontact printing of self-assembled monolayers: Applications in microfabrication." Nanotechnology **7**(4): 452-457.

Willner, I. K. E. (2005). Bioelectronics: From Theory to Applications, Wiley-VCH Verlag GmbH & Co.

Win, M. N., J. S. Klein and C. D. Smolke (2006). "Codeine-binding RNA aptamers and rapid determination of their binding constants using a direct coupling surface plasmon resonance assay." Nucleic Acids Research **34**(19): 5670-5682.

Wong, I. Y., B. D. Almquist and N. A. Melosh (2010). "Dynamic actuation using nano-bio interfaces." Materials Today **13**(6): 14-22.

Wong, I. Y., M. J. Footer and N. A. Melosh (2008). "Electronically activated actin protein polymerization and alignment." Journal of the American Chemical Society **130**(25): 7908-7915.

Wong, I. Y. and N. A. Melosh (2009). "Directed Hybridization and Melting of DNA Linkers using Counterion-Screened Electric Fields." Nano Letters **9**(10): 3521-3526.

Wong, I. Y. and N. A. Melosh (2010). "An Electrostatic Model for DNA Surface Hybridization." Biophysical Journal **98**(12): 2954-2963.

Wu, C. D., T. H. Fang and J. F. Lin (2013). "Nanotribology of self-assembled monolayer with a probe tip investigated using molecular dynamics simulations." Micron **44**: 410-418.

Wu, C. D., J. F. Lin and T. H. Fang (2007). "Molecular dynamic simulation and characterization of self-assembled monolayer under sliding friction." Computational Materials Science **39**(4): 808-816.

Wu, Q., M. Tsiang and J. E. Sadler (1992). "Localization of the single-stranded DNA binding site in the thrombin anion-binding exosite." Journal of Biological Chemistry **267**(34): 24408-24412.

Yang, Y. S., M. Kochoyan, P. Burgstaller, E. Westhof and M. Famulok (1996). "Structural basis of ligand discrimination by two related RNA aptamers resolved by NMR spectroscopy." Science **272**(5266): 1343-1347.

Yu, Z. B., J. D. Schonhoft, S. Dhakal, R. Bajracharya, R. Hegde, S. Basu and H. B. Mao (2009). "ILPR G-Quadruplexes Formed in Seconds Demonstrate High Mechanical Stabilities." Journal of the American Chemical Society **131**(5): 1876-1882.

Zhang, L. Z., W. A. Goddard and S. Y. Jiang (2002). "Molecular simulation study of the c(4x2) superlattice structure of alkanethiol self-assembled monolayers on Au(111)." Journal of Chemical Physics **117**(15): 7342-7349.

Zhang, L. Z. and S. Y. Jiang (2002). "Molecular simulation study of nanoscale friction for alkyl monolayers on Si(111)." Journal of Chemical Physics **117**(4): 1804-1811.

Zhao, J., Q. Wang, G. Liang and J. Zheng (2011). "Molecular Dynamics Simulations of Low-Ordered Alzheimer beta-Amyloid Oligomers from Dimer to Hexamer on Self-Assembled Monolayers." Langmuir **27**(24): 14876-14887.

Zhao, L., X. M. Duan, X. G. Xue, M. H. Li and Z. S. Li (2011). "Self-assembled monolayers of oligosilane on the silicon (001) surface: molecular dynamics simulations." Journal of Molecular Modeling **17**(4): 721-726.

APPENDIX STATISTICAL TECHNIQUES UTILIZED TO OBTAIN PHYSICAL INSIGHTS

In Chapter 2 (electrostatic actuation of the binding behavior between thrombin and aptamer), the idea of experimental design is to first set up a data model – specific binding between thrombin and aptamer, then compared the electrostatic actuation experiment results with the data model and obtained the electrical field influence on the binding behavior of the pair. To confirm the binding specificity, both of the objective group (thrombin – aptamer) and control group (thrombin - polyA, and γ-thrombin – aptamer) were tested independently and compared to acquire meaningful conclusion (detailed description on page 17-19). Regarding the result interpretation, both normality test and resampling method boot-strap were applied to compute the confidence intervals, and the difference of height measurement between objective and control group could be explained by the fact that whether there is overlap of the confidence intervals among any groups, i.e. whether there is statistically significant difference among groups (detailed description on page 23-24, results shown in Fig. 2-6 on page 25, and Appendix Table 2-1 on page 29-30). In the electrostatic actuation experiment, similar result interpretation procedure was adopted to explicate whether there is statistically significant difference among various potential treatments (detailed description on page 27, results shown in Fig. 2-8 on page 28, and Appendix Table 2-2 on page 30). The outside variables such as the composition and concentration of binding buffer, stiffness of AFM cantilever, surface roughness of gold substrate, were controlled very strictly to ensure the significant change on sample was purely caused by the objective condition - molecular binding and electrostatic potential.

In Chapter 3 and 4 (open circuit AFM based DFS studies on the force interaction of thrombin and aptamer, and ECAFM based DFS investigations of the electrical field influence on the force interaction of thrombin and aptamer), the idea of experimental design is to first set up a data model – force interaction of specific binding between thrombin and aptamer, then compared the ECAFM experiment results with the data model and obtained the electrical field influence on the force interaction of the pair. To further confirm the binding specificity, both of the objective group (thrombin – aptamer) and control group (thrombin - polyA, and thrombin - PEG) were tested and compared to acquire meaningful conclusion (detailed description on page 35-38). Regarding the result interpretation, histogram was used to present the rupture force distribution according to different loading rate levels (detailed description on page 43-44, results shown in Fig. 3-4 and Fig. 3-5 on page 44), then autocorrelation function (ACF) was applied to acquire the force quantum (detailed description on page 45, results shown in Fig. 3-6 on page 45 and Appendix Fig. 3-1 on page 50). Finally, linear regression was utilized on dynamic spectrum to fit a theoretical model to our experimental results so as to estimate very important kinetic parameters (detailed description on page 48, results shown in Fig. 3-7 on page 49). In ECAFM experiment, similar result interpretation procedure was adopted to explicate whether there is statistically significant difference among the force interactions under different potential treatments (Histogram: detailed description on page 60-61, results shown in Fig. 4-3 and Fig. 4-4 on page 61-62, and Appendix Fig. 4-1 – Fig.

4-4 on page 67-70; ACF: detailed description on page 62-63, results shown in Fig. 4-5 on page 63, and Appendix Fig. 4-5 – Fig. 4-8 on page 70-72; Linear regression: detailed description on page 66, results shown in Fig. 4-6 on page 64 and Table 4-3 on page 66). The outside variables such as the composition and concentration of binding buffer, stiffness of AFM cantilever, surface roughness of gold substrate, were controlled very strictly to ensure the significant change on sample was purely caused by the objective condition - molecular force interaction and electrostatic potential.

In Chapter 5 and 6 (MD simulation on electrical field induced conformational transition and friction response change of MHA SAMs, and comparison with associated AFM force curve experiment), energy output was analyzed to describe the overall physical process (detailed description on page 83 and page 111, results shown in Fig. 5-2 on page 83, and Fig. 6-3 on page 111). Average height and height distribution of oxygen atoms were analyzed to illustrate the conformational transition under the application of electrical fields (detailed description on page 89 and page 112, results shown in Table 5-1 and Fig. 5-7 on page 89, and Table 6-1 and Fig. 6-6 on page 114-115). Then in friction simulation, statistical analysis on frictional coefficients as a function of normal loads and applied electrical fields was carried out to explicate the electrostatic influence on friction response of SAMs (detailed description on page 96, results shown in Fig. 5-9 and Fig. 5-10 on page 96). Bonded energy output was computed to further explain the deformation mechanism of the SAMs during sliding (detailed description on page 98-99, results shown in Table 5-2 on page 98). Regarding the comparison of MD simulation and AFM experiment on MHA SAMs, height distribution and counts of the oxygen atom in carboxylic end group and carbon atom in the last methylene group were computed to illustrate the conformational transition and explain the experimental results on adhesion (detailed description on page 115-116, 118, results shown in Fig. 6-7 and Table 6-2 on page 116-117, 118-119). Radial distribution function (RDF) of oxygen atoms (detailed description on page 120-121, results shown in Fig. 6-10 on page 121) and structure factor of backbone chains (detailed description on page 121-122, results shown in Fig. 6-11 on page 122) were calculated to explain the structural order effect for experimental results on friction.

In Chapter 7 (MD simulation on electrical field induced conformational transition and friction response change of PEG SAMs), energy output was analyzed to describe the overall physical process (detailed description on page 136-137, results shown in Fig. 7-3 on page 137). Average tilt angle of the backbone chains was analyzed to illustrate the electrical field influence on hydrocarbon sections (detailed description on page 139-140, results shown in Fig. 7-6 on page 140). Then structure factor of the backbone chain was calculated to explicate the structural order of the whole chains (detailed description on page 140-141, results shown in Fig. 7-7 on page 141). After that RDF of oxygen atoms in OCCO dihedral groups were computed to illustrate the conformational transition between two states: “gauche” and “all-trans” (detailed description on page 141-143, results shown in Fig. 7-8 on page 143). Then dihedral potential change and normal density profile were analyzed to depict the conformational transition upon the whole SAMs (detailed description on page 143-145, results shown in Table 7-1 on page 144 and Fig. 7-9 on page 145). In friction simulation, statistical analysis on frictional coefficients as a function of normal loads and applied electrical fields was carried out to explicate the electrostatic influence on friction response of SAMs (detailed description on page 146-148, results shown in Fig. 7-11 on page 148). Bonded energy output was computed to further explain the deformation mechanism of the SAMs during sliding (detailed description on page 148, results shown in Table 7-2 on page 148).